ABSTRACT

Title of thesis: AERODYNAMIC ANALYSIS AND SIMULATION OF A TWIN-TAIL TILT-DUCT UNMANNED AERIAL VEHICLE

Cyrus Abdollahi, Masters of Science, 2010

Thesis directed by: Assistant Professor J. Sean Humbert
Aerospace Engineering

The tilt-duct vertical takeoff and landing (VTOL) concept has been around since the early 1960s; however, to date the design has never passed the research phase and development phase. Nearly 50 years later, American Dynamics Flight Systems (ADFS) is developing the AD-150, a 2,250lb weight class unmanned aerial vehicle (UAV) configured with rotating ducts on each wingtip. Unlike its predecessor, the Doak VZ-4, the AD-150 features a V tail and wing sweep − both of which affect the aerodynamic behavior of the aircraft. Because no aircraft of this type has been built and tested, vital aerodynamic research was conducted on the bare airframe behavior (without wingtip ducts). Two weeks of static and dynamic testing were performed on a 3/10th scale model at the University of Maryland's 7' x 10' low speed wind tunnel to facilitate the construction of a nonlinear flight simulator. A total of 70 dynamic tests were performed to obtain damping parameter estimates using the ordinary least squares methodology. Validation, based on agreement between static and dynamic estimates of the pitch and yaw stiffness terms, showed an

average percent error of 14.0% and 39.6%, respectively. These inconsistencies were attributed to: large dynamic displacements not encountered during static testing, regressor collinearity, and, while not conclusively proven, differences in static and dynamic boundary layer development. Overall, the damping estimates were consistent and repeatable, with low scatter over a 95% confidence interval. Finally, a basic open loop simulation was executed to demonstrate the instability of the aircraft. As a result, it is recommended that future work be performed to determine trim points and linear models for controls development.

AERODYNAMIC ANALYSIS AND SIMULATION OF A TWIN-TAIL TILT-DUCT UNMANNED AERIAL VEHICLE

by

Cyrus Abdollahi

Thesis submitted to the Faculty of the Graduate School of the
University of Maryland, College Park in partial fulfillment
of the requirements for the degree of
Masters of Science
2010

Advisory Committee:
Assistant Professor J. Sean Humbert/Advisor
Professor Inderjit Chopra
Associate Professor James Baeder

Dedication

To my parents, and to Maynard and Gay Hill, who always encouraged me to do my best, work hard, and take time to enjoy life.

Acknowledgments

I would like to thank everyone that made this thesis possible. First, I would like to thank Dr. Humbert, who took me under his wing and allowed me to work on this project. Second, I would like to thank Paul Vasilescu of American Dynamics Flight Systems and their partnership on this Maryland Industrial Partnerships (MIPS) grant. Third, I would like to thank Dr. Jewel Barlow, director of the Glen L. Martin Wind Tunnel for his help and support throughout the project. Fourth, I would like to thank Dr. Eugene Morelli of NASA Langley for his guidance on the system identification portion of this thesis. Finally, I would like to thank Dr. Steve Fritz for being patient with me and allowing to me to finish my thesis.

In addition, I would like to thank all the graduate students I have had the pleasure working together with at the AVL laboratory. In particular, Scott Owen, who originally had this thesis but had to switch due to time constraints with the Navy. Good luck in Navy test pilot school! Also, I would like to thank Mac MacFarlane for his help in processing the CFD data, and Bryan Patrick for bouncing ideas off of. Finally, I would like to thank Brandon Bush for helping me out on my AHS and AIAA presentations, student paper, and this thesis.

Table of Contents

List of Tables vii

List of Figures viii

Nomenclature x

1 Introduction 1
1.1 Motivation . . . 1
1.2 Objectives and approach of current research . . . 4

2 Literature Review 7
2.1 Doak VZ-4 . . . 7
2.2 Wind Tunnel Tests . . . 9
2.3 Flight Tests . . . 10
2.4 Stability Derivatives . . . 16

3 Model Scaling 17
3.1 Similitude . . . 17
3.2 Scaling Ratio . . . 18
3.3 Propulsion . . . 19

4 Experimental Setup: Static Testing 21
4.1 Model Construction . . . 21
4.2 Design of Experiment . . . 24
4.3 Measurement Instrumentation and Accuracy . . . 25
4.4 Tare and Interference . . . 26
4.4.1 Test Procedure . . . 28
4.4.2 Test Matrix . . . 30
4.5 Aerodynamic Conventions . . . 32

5 Experimental Results: Static Testing 34
5.1 Introduction . . . 34
5.2 Flow Visualization . . . 35
5.3 Longitudinal Trim Coefficients . . . 36
5.3.0.1 Lift . . . 36
5.3.0.2 Drag . . . 37
5.3.0.3 Pitching Moment . . . 37
5.4 Lateral Trim Coefficients . . . 42
5.4.0.4 Side Force . . . 42
5.4.0.5 Roll Moment . . . 42
5.4.0.6 Yaw Moment . . . 43
5.5 Controls Deflections . . . 47
5.5.1 Flaperons: High Lift Device . . . 47

5.5.2 Ruddervators: Pitch . . . 48
5.5.3 Reflection Method . . . 53
5.5.4 Flaperons: Roll . . . 54
5.5.5 Ruddervators: Yaw . . . 56

6 Experimental Setup: Dynamic Testing 61
6.1 Design of Experiment . . . 61
6.2 Origins of Aerodynamic Damping . . . 62
6.3 System Identification . . . 65
6.3.1 Background Theory . . . 65
6.3.2 SIDPAC . . . 67
6.3.2.1 deriv.m . . . 67
6.3.2.2 smoo.m . . . 68
6.3.2.3 mof.m . . . 69
6.3.2.4 *r_colores.m* . . . 71
6.3.3 Data Filtering . . . 72

7 Experimental Results: Dynamic Testing 74
7.1 Yaw Perturbation Tests . . . 74
7.1.1 Test Procedure . . . 74
7.1.2 Model Structure Determination . . . 76
7.1.3 Parameter Estimation . . . 79
7.1.4 Comparison of Static and Dynamic Data . . . 80
7.2 Pitch Perturbation Tests . . . 83
7.2.1 Test Procedure . . . 83
7.2.2 Model Structure Determination . . . 85
7.2.3 Stability Analysis . . . 87
7.2.4 Spring-Mass Damper System . . . 90
7.2.5 Dynamic Model Structure Determination . . . 91
7.2.6 Parameter Estimation . . . 93
7.2.7 Comparison of Static and Dynamic Data . . . 94
7.3 Origin Offsets . . . 95
7.4 Assumptions . . . 96

8 Simulink Math Models 97
8.1 Nonlinear Simulation . . . 97
8.2 Equations of Motion . . . 100
8.3 Environmental Properties . . . 102
8.4 Control variables . . . 103
8.5 Mass & Inertia Properties . . . 105
8.6 Static Lookup Tables . . . 110
8.7 Force & Moment Summation . . . 112
8.8 Aerodynamic Damping . . . 113
8.9 Engine Dynamics . . . 115
8.9.1 HTAL Fans . . . 115

8.10 Open Loop Simulation 125

9 Conclusions and Recommendations for Future Works 127
9.1 Summary 127
9.2 Limitations 127
9.3 Conclusions 128
9.4 Future work 131

A VZ-4 Stability Derivatives 133

B Test Matrix 138

C Sensor Specifications 145

D CFD Test Matrix 146

Bibliography 154

List of Tables

1.1 Technical Specifications 3

2.1 VZ-4 Longitudinal Hover Derivatives based on momentum theory. . . 16
2.2 VZ-4 Lateral Hover Derivatives based on momentum theory. 16

4.1 Tare & Interference Test Matrix 30
4.2 Abbreviated Test Matrix 31

6.1 Aerodynamic Damping Parameters 65

7.1 Percent error of static and dynamic parameter estimates. 82
7.2 Mechanical parameter estimates (2-σ standard deviation). 90
7.3 Percent error between static and dynamic parameter estimates. . . . 94

8.1 Control surface saturation limits. 104
8.2 CFD propulsion test matrix 118

A.1 VZ-4 Longitudinal Derivatives 134
A.2 VZ-4 Longitudinal exact and approximate factors 135
A.3 VZ-4 Lateral Derivatives 136
A.4 VZ-4 Lateral exact and approximate factors 137

A-1 Wind Tunnel Test Matrix 139
A-1 Wind Tunnel Test Matrix - Cont'd 140
A-1 Wind Tunnel Test Matrix - Cont'd 141
A-1 Wind Tunnel Test Matrix - Cont'd 142
A-1 Wind Tunnel Test Matrix - Cont'd 143
A-1 Wind Tunnel Test Matrix - Cont'd 144
A-2 Variable Definitions 144

C-1 Jewell Instruments LSO inclonometer 145
C-2 Microstrain 3DM-GX1 Specifications 145

D-1 CFD Test Matrix, Ducts 148
D-1 CFD Test Matrix, Cont'd. 149
D-1 CFD Test Matrix, Cont'd. 150
D-1 CFD Test Matrix, Cont'd. 151
D-1 CFD Test Matrix, Cont'd. 152
D-1 CFD Test Matrix, Cont'd. 153

List of Figures

1.1 AD-150 tilt-duct VTOL UAV. 2
1.2 Comparison of AD-150 hovering efficiency to various production aircraft, data from [4]. 3

2.1 Doak VZ-4 tilt-duct aircraft (dimensions in feet) [17]. 7
2.2 Residual exhaust deflection schemes [6]. 8
2.3 Ground effect hover testing and flow pattern distributions [16]. 11
2.4 Flow over wing during steady-state descent at constant duct angle and airspeed and varying fuselage angle of attack and power (δ_d - duct tilt angle, V forward airspeed, α_w wing angle of attack)[16]. . . . 15

4.1 3/10 Scale Wind Tunnel Model (Dimensions in inches) 21
4.2 Model assembly 22
4.3 Control surface attachment inaccuracies. 23
4.4 Static instrumentation. 25
4.5 Inverted model with single-strut mounting and image system. 27
4.6 Aerodynamic reference frames. 32

5.1 Flow visualization at nose stagnation point. 35
5.2 Lift Coefficient 39
5.3 Drag Coefficient 40
5.4 Pitch Momement Coefficient 41
5.5 Side Force Coefficient 44
5.6 Roll Coefficient 45
5.7 Yaw Coefficient 46
5.8 Flap Deflection: V = 110 mph, $\beta = 0^o$ 50
5.9 Elevator Control Power (Longitudinal): V = 110 mph 51
5.9 Elevator Control Power (Lateral): V = 110 mph 52
5.10 Reflection Method 53
5.11 Aileron Control Power (Longitudinal): V = 110 mph 57
5.11 Aileron Control Power (Lateral): V = 110 mph 58
5.12 Rudder Control Power (Longitudinal): V = 110 mph 59
5.12 Rudder Control Power (Lateral): V = 110 mph 60

6.1 Microstrain 3DM-GX1 Inertial Measurement Unit 62
6.2 Influence of the yawing rate on the wing and vertical tail. 63
6.3 Wing planform undergoing a rolling motion. 63
6.4 Mechanism for aerodynamic force due to pitch rate. 64

7.1 Controls neutral heading offset, $\psi = -5.6^o$ 74
7.2 Wind-tunnel model constrained to pure yawing motion. 76
7.3 Controls neutral yaw perturbation. 78
7.4 $\delta_r = 15^o$ yaw perturbation. 78
7.5 Damping parameter estimates vs. tunnel speed w/95% CI. 80

7.6 Static yaw moment curves at for $\theta = 0^o$, $V = 110$ mph. 81
7.7 Wing-tail vortex interaction. 83
7.8 Extension spring added for stability augmentation. 84
7.9 Wind-tunnel model constrained to pure pitching motion. 85
7.10 Wind-tunnel model constrained to pure pitching motion. 86
7.11 Static pitch moment about the pivot point. 88
7.12 Controls neutral pitch perturbation (High α spring geometry). 92
7.13 Damping parameter estimates vs. tunnel speed & trim condition with 95% CI. 93

8.1 Wind frame function block. 97
8.2 Simulink duct rotation matrices. 99
8.3 Equations of motion function block. 100
8.4 Atmospheric and gravitational parameters. 102
8.5 Simulation control inputs and saturation limits. 103
8.6 Calculation of mass and inertia properties. 105
8.7 Duct frame and pivot point. 106
8.8 Inertia Subfunction 108
8.9 Parallel axis theorem (D matrix). 109
8.10 Aerodynamic lookup tables. 110
8.11 Aerodynamic, Graviational, and propulsive forces and moments. . . . 112
8.12 Aerodynamic damping function block diagram. 113
8.13 Engine dynamics subsystem. 115
8.14 High level calculation of duct forces and moments. 116
8.15 Quasi-steady duct velocities. 117
8.16 Polar coordinate Transformation. 119
8.17 Duct parameter transformation and Force/Moment lookup. 120
8.18 Conversion of duct forces and moments to aircraft body frame. 122
8.19 Gyroscopic couplings. 124
8.20 Open loop simulation results. 126

Nomenclature

a	sonic velocity
$\bar{c}$	average wing chord
C_L	lift coefficient
C_D	drag coefficient
C_{Y_w}	side force coefficient (wind axis)
C_{l_w}	roll moment coefficient (wind axis)
C_{m_w}	pitch moment coefficient (wind axis)
C_{n_w}	yaw moment coefficient (wind axis)
D	diameter
G	orthogonalization transformation matrix
I	inertia matrix
k	frequency index
Ma	Mach number or local free-stream Mach number, V/a
MSFE	Mean Squared Fit Error
N	number of data points
p	body axis roll rate
$\hat{p}$	nondimensional body axis roll rate
$\boldsymbol{P}$	orthogonal regressor matrix
PSE	Predicted Square Error
q	body axis pitch rate
$\hat{q}$	nondimensional body axis pitch rate
r	body axis yaw rate
$\hat{r}$	nondimensional body axis yaw rate
$\hat{\mathcal{R}}$	autocorrelation matrix
R^2	fit error
Re	Reynolds bumber based on chord, $\rho V c/\mu$
S	planform area
V_∞	free stream velocity
u	body X-Axis belocity
v	body Y-Axis belocity
w	body Z-Axis belocity
X	body axis unit vector (forward though the nose)
$\boldsymbol{X}$	standard regressor matrix
$\boldsymbol{y}$	model output
Y	body axis unit vector (out the right wing)
$\boldsymbol{z}$	measured output
$\bar{z}$	mean of measured output
Z	body axis unit vector (through the belly)

Greek Symbols

α	angle of attack
β	sideslip angle
δ_e	elevator deflection [deg]
δ_f	flap deflection [deg]
δ_a	aileron deflection [deg]
δ_r	rudder deflection [deg]
$\boldsymbol{\theta}$	model parameters
θ	Euler angle pitch
κ	torsional spring constant
$\boldsymbol{\nu}$	measurement noise
ρ	air density
$\boldsymbol{\sigma}$	measurement variance
τ	spring torque
ϕ	Euler angle roll
ψ	Euler angle yaw

Subscripts

0	trim value
∞	free-stream conditions
STD	standard atmosphere

Superscripts

T	matrix transpose
-1	matrix inverse
$\dot{}$	time derivative
$\hat{}$	estimated value

Abbreviations

ABC	Advanced Blade Concept
AD	American Dynamics
ADFS	American Dynamics Flight Systems
AUV	Autonomous Unmanned Vehcile
CFD	Computational Fluid Dynamics
CNC	Computer Numeric Control
CV	Constant-Velocity Joint
DAQ	Data Acquisition System
DFMA	Design for Manufacture and Assembly
HTAL	High Torque Arial Lift
IMU	Inertial Measurement Unit
ISA	1979 International Standard Atmosphere
ISR	Intelligence,Surveillance, and Reconnaissance
JSF	Joint Strike Fighter
LTI	Linear Time Invariant
NACA	National Advisory Committee for Aeronautics
NASA	National Aeronautics and Space Administration (Formally NACA)
NED	North-East Down coordinate frame
OEI	One Engine Inoperative
PIO	Pilot Induced Oscillations
RANS	Reynolds-Averaged Navier-Stokes
RFC	Reference Flight Condition
RFI	Request for Information
RPV	Remotely Piloted Vehcile
SAR	Search and Rescue
SFC	Specific Fuel Consumption
SKF	Svenska Kullagerfabriken bearing company
SoS	Speed of Sound
STOVL	Short Take-Off and Vertical Landing
UAV	Unmanned Air Vehcile
V/STOL	Vertical/Short Take-Off and Landing
VTOL	Vertical Take-Off and Landing
WGS84	1984 World Geodetic System
WT	Wind Tunnel

Chapter 1

Introduction

1.1 Motivation

Currently, unmanned aircraft play a vital role in the United States military. This is highlighted by the fact that it has roughly double the number of unmanned vs. manned aircraft [1]. Typically, unmanned aerial vehicles (UAVs) are used for intelligence, surveillance, and reconnaissance (ISR) missions. They are also relied upon for target acquisition, communications relay, border patrol, and search and rescue (SAR), to name a few. From a military standpoint, the UAV allows the battlefield commander to get persistent real-time information, literally around the clock - without risking soldiers lives.

Recently, the Marines aging UAV fleet along with the Navy's sucessful landing of the MQ-8 [3] on the back of a naval ship spawned the production of the Marine Crops Tier III request for information (RFI) on a medium range high speed autonomous vertical takeoff and landing (VTOL) tactical UAV. The requirements are for a high speed VTOL aircraft that can fly ahead of the V-22 Osprey (currently no marine aircraft can perform this task, manned or unmanned). The UAV must be capable of runway independent operations from unprepared locations in-country, without a priori knowledge of terrain or obstacles. Also, the inherent naval operations performed by the marines means that the vehicle must have a large radius

of action, allowing ship-to-shore operation. The ship based operation means that autopilot system must be able to cope with a deck that is both pitching and translating. The problem is further exacerbated by the naturally turbulent flow due to the wake of the superstructure. As a result, good characterization of the aircraft dynamics is critical.

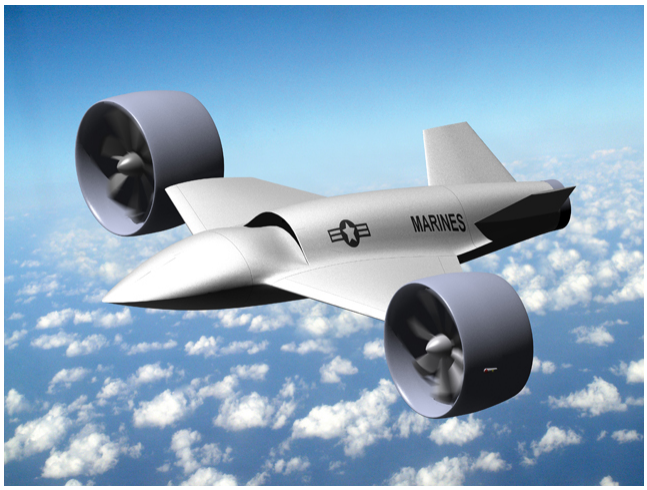

Figure 1.1: AD-150 tilt-duct VTOL UAV.

In response to the RFI, American Dynamics Flight Systems (ADFS) developed their concept of the AD-150 (Fig. 1.1). Designed by chief technology officer, Paul Vasilescu, the AD-150 is a twin-tail tilt-duct unmanned aerial vehicle. Fixed pitch, shaft driven ducts, are integrally mounted on the wingtips. Power is obtained from a central turboshaft engine. Directional control in forward flight is provided by the use of ruddervators and flaperons. In hover, where aerodynamic surfaces become ineffective, attitude and directional control are achieved by tilting the thrust vector of the ducts and residual exhaust gases of the engine. The ducts have the ability to pitch collectively, but can yaw independently; similarly, deflecting vanes at the

engine exit nozzle allow for yaw and pitch control. The performance metrics[1] of the vehicle are given in Table 1.1.

Table 1.1: Technical Specifications

Length	14.5 ft
Wing Span	17.5 ft
Height	4.75 ft
Max Speed	300 kts
Max Takeoff Weight	2,250 lbs
Payload Capacity	500 lbs
Powerplant	PW 200
Fuel Type	JET-A, JP-4, JP-5
Navigation	Dual GPS with INS/IMU
Command & Control	STANAG 4586
LOS Communications	TCDL

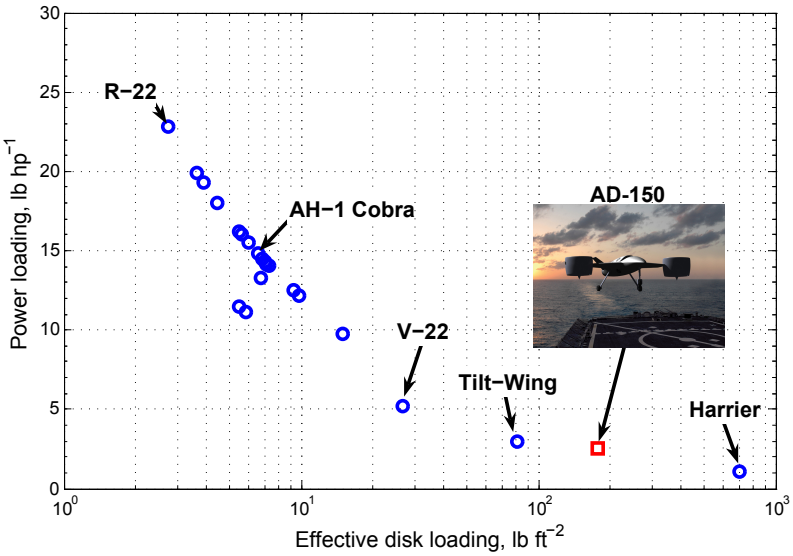

Figure 1.2: Comparison of AD-150 hovering efficiency to various production aircraft, data from [4].

As a basis of comparison, a log plot of the AD-150 and 22 other production rotorcraft are given in Fig. 1.2. The abscissa is the effective disk loading, which is the thrust per unit rotor area. The ordinate is the power loading, which is

[1]These are projected estimates, which have not been validated by flight test at the time of this writing.

the thrust per unit horsepower. Plotted against each other, the graph provides a loose metric for comparing hover efficiencies. Higher efficiencies (larger power loadings) are realized when the thrust is distributed over a larger disk area (lower disk loadings). As expected, AD-150 falls between tilt rotors and pure jet thrust augmentation. Clearly, this indicates a suboptimal design from a hovering efficient perspective. However, this is less of a problem when one considers that the mission requirements are primarily for high speed flight, and that the VTOL component is only for runway independent accessibility. In order to give an accurate context of the above graph, the fundamental physics of the various V/STOL concepts are given in the next Chapter.

1.2 Objectives and approach of current research

In support of the work being done by ADFS, the objectives of this thesis were to:

1. Design and fabricate a $3/10^{th}$ scale wind tunnel model of the AD-150.

2. Obtain a complete 6-DOF aerodynamic database of static coefficients accounting for variations in freestream conditions and control deflections for validation of CFD data produced by ADFS.

3. Calculate quasi-steady aerodynamic damping terms along the pitch and yaw axis.

4. Construct a nonlinear simulation environment in Simulink using the aerody-

namic data to allow for future linearizations and controls design.

Chapter 2 contains a literature review of past research on the Doak VZ-4, encompassing both wind tunnel and flight tests. Wind tunnel tests were conducted on a duct/semi-span wing combination; whereas, qualitative flight tests were conducted to determine the aircrafts handling qualities. Chapter 3 discusses the limitations of model scaling and precautionary notes on the interpretation of subscale wind tunnel results. Chapter 4 presents an overview of experimental setup for static wind tunnel tests, including: an overview of the wind tunnel model and its construction process, design of experiment, tare and interference tests, test matrix, and aerodynamic conventions used to report the data. Chapter 5 presents the results of the static test data for both stability and control effectiveness. These tests were conducted at various freestream velocities, angles of attack, and sideslip velocities. Control deflection tests included use of both ruddervators and flaperons. Measurements were made along all three axes for a complete 6-DOF dataset. Chapter 6 discusses the experimental setup for dynamic wind tunnel tests. In addition, background information is given on the system identification methodologies utilized on the data. Chapter 7 presents the results of dynamic test data for pitch and yaw rate damping terms: assumptions and validation are also detailed. Chapter 8 describes the Simulink simulation environment and math models used to represent the dynamic behavior of the aircraft. Output of a simple open loop run is presented to demonstrate the unstable nature of the aircraft. Chapter 9 summarizes the work presented, along with concluding remarks and future work. Appendix A details stability and control

derivatives for the Doak VZ-4. Appendix B presents the complete wind tunnel test matrix (static, dynamic, and tare). Appendix C contains instrumentation sensor specifications. Finally, Appendix D contains a complete test matrix of CFD duct data used in Simulink.

Chapter 2

Literature Review

Extensive research and development on tilt-wing VTOL aircraft was conducted in the period of 1960-1965 between the Doak Aircraft Corporation and NASA, including full scale flight tests and semi/full scale testing of a shrouded rotor on a semispaned wing. Since then, almost no research has continued on a wingtip mounted tilt-duct aircraft of the same configuration.

2.1 Doak VZ-4

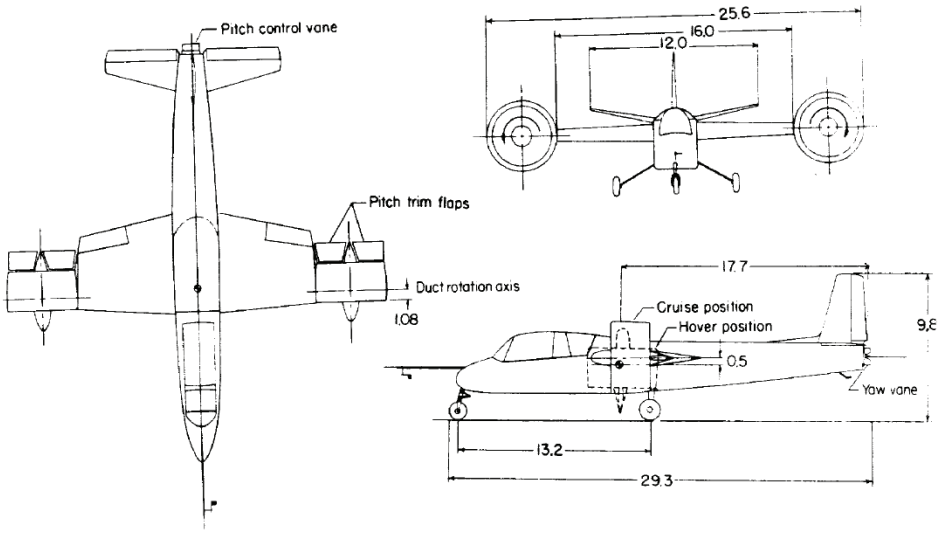

Figure 2.1: Doak VZ-4 tilt-duct aircraft (dimensions in feet) [17].

The Doak VZ-4 (Fig. 2.1) was the first, and only, wingtip mounted tilt-duct VTOL aircraft that was successfully built and flown from hover to forward flight,

and back. The aircraft uses conventional control surfaces (ailerons, elevator, and rudder)[1] for forward flight. In hover, lateral control was made by use of radial guide vanes in each duct inlet, which change the angle of attack of the blades and thrust generated. In addition, pitch and yaw control was provided by deflecting residual exhaust gasses using tangential flaps, spoilers, and a variable cruciform surface (Fig. 2.2). The cruciform surface was eventually adopted as having the most effective control authority. During transitional conversion, a switch on the control stick caused duct rotation. After the ducts rotated to the forward flight position, the vane deflections were phased out. Pitch and yaw control was performed by way of a three piece articulated cruciform tail vane in the engine-exhaust exit. Note that after the first series of flight tests pitch trim flaps were added to the diffuser exit plane of each duct to help reduce the excessive nose-up pitching moments.

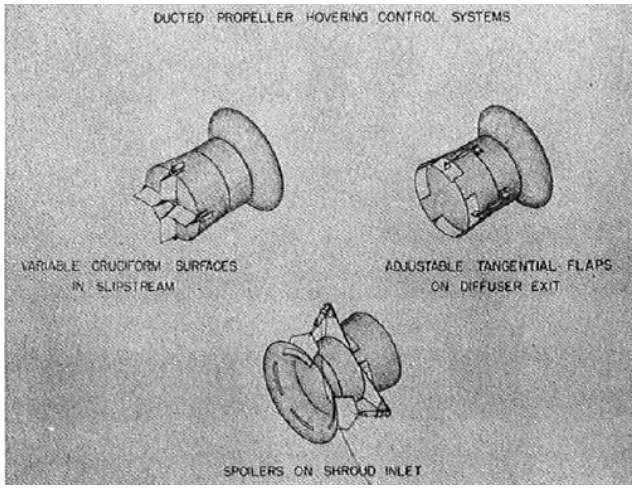

Figure 2.2: Residual exhaust deflection schemes [6].

[1] A complete table of the control surfaces characteristics are tabulated in Ref. [16].

2.2 Wind Tunnel Tests

In conjunction with flight tests, extensive wind tunnel tests were performed on full and subscale semispan duct configurations to determine baseline and performance changes due to: inlet vanes, duct angle, and trim flaps (to combat high destabilizing moments). An overview of the test results can be found in Ref. [7].

Subscale Tests

Several tests [6, 8, 9, 10] were conducted on subscale models of a duct and semispan wing to characterize the full scale performance of the Doak VZ-4. Problems with premature leading edge stall on the models prevented accurate extrapolation to full scale performance; however, important findings were:

- 30% power reduction can be realized when the ducts are unloaded by operating the wing at a higher angle of attack
- large destabilizing pitch up moments are generated during decelerating flight conditions where the angle of attack is largest
- power required in ground effect increases due to possible backpressure effects on the propeller and suction effects on the lower wing surface
- hysteresis was observed when transiting through high angles of attack

Full Scale Tests

Four full scale wind tunnel tests [11, 12, 13, 14] of 4ft ducts on a semispan wing (both exact duplicates of the VZ-4) were performed in support of flight testing. The important findings of these tests were:

- duct inlet vanes were able to modify thrust production by 11%, thereby increasing lateral directional control
- trim flaps in the diffuser of the duct reduced pitching moments by half for a 3% increase in power

2.3 Flight Tests

Between 1960-1963 three flight studies [15, 16, 17] of the Doak VZ-4 were performed to obtain qualitative estimates of the aircrafts handling qualities, including: hover, transition to forward flight, forward flight, and transition to hover (landing). Airspeed, pressure altitude, angle of attack, duct angle, engine-output shaft speed, horizontal tail angle, and engine gear-box oil pressure were crudely recorded using two cameras photographing the pilots instrument panel at a rate of two frames per second. Angular velocities and control stick positions were measured on an oscillograph. An air data sensor was used on the end of a nose boom to measure angle of attack and sideslip; however, these time histories were not provided in any of the reports. As a result, the method of data collection is not of sufficient fidelity to be used for modern system identification techniques. Apparent static and dynamic stability was assessed from data of stick position and time to damp, and are therefore

considered qualitative in nature: no quantitative values were calculated.

Hover

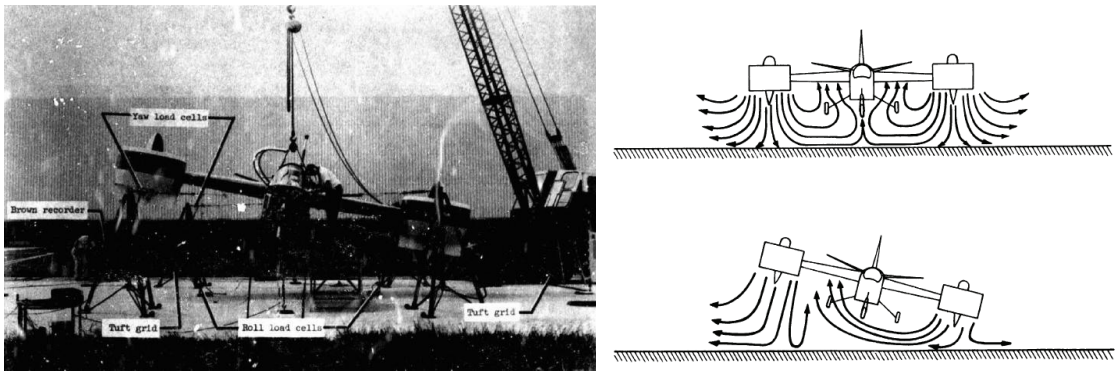

(a) Hovering Static test rig.

(b) Destabilizing downwash flow patterns on underside of the wing in ground effect.

Figure 2.3: Ground effect hover testing and flow pattern distributions [16].

Hover tests were performed using NASA test pilots to assess the aircraft's handling qualities as compared to other VTOL aircraft configurations. Overall, the aircraft was very difficult to control about the roll and yaw axes, even when out of ground effect. It was generally considered too hazardous to attempt roll-control inputs because of the large time delays and inability to arrest roll rates within safe limits. During testing, roll displacements could not be corrected even with full lateral control, resulting in contact with the ground. Rudder control authority was equally poor, with deflections insufficient to prevent heading changes as large as 90^o or more. Analysis on the lateral control authority showed the ratio of control power to aircraft inertia was too low, resulting in 1/6 th and 1/10 th the minimum acceptable values for VTOL aircraft [16].

Tethered ground tests (Fig. 2.3a) were performed to better understand the

behavior in hover. Tie down cables were equipped with load cells to measure rolling moments from control inputs, and allowed the height of the vehicle to range from 4, 6, and 8 feet in altitude. At each height above the ground, the aircraft was tested at bank angles of $\pm 10^o$ and 80% engine power. Tufts were arranged on the aircraft, cables, and ground to observe the flow around the aircraft and showed that the strong rolling moments were partly due to asymmetrical flow under the wing when at a bank angle and in ground effect (Fig. 2.3b).

Transition to Forward Flight

Transition flights from hover to forward flight were limited by the time at which the ducts could be tilted from vertical to horizontal: 11 seconds. Pilot reports indicated that power changes were smooth, accelerating conversion without loss in altitude was possible, and that excessive but tolerable controls deflections were required. In order to overcome the large pitch up moments from the ducts, significant down elevator trim was needed [15].

Forward Flight

Forward flight tests were performed to determine the static and dynamic handling qualities, along with stall boundaries. Stall boundary plots for a range of airspeeds and duct angles can be found in Ref. [17]. Near stall, significant and erratic roll moments were found that would cause stick "snatching," where the stick would violently whip from side to side.

Static stability was assessed for apparent dihedral, while directional stability was based on stick input positions. Apparent dihedral from stick position time histories was tested in level flight and found to be satisfactory at low duct angles, but less so as duct angle was increased. Pilots reported the aircraft as being marginally acceptable for zero duct angle (in the forward flight position), but unsatisfactory as duct angle increased due to inadequate roll control power, particularly in rough air. Apparent directional stability was assessed for speeds between 46-96 kts for various duct angles using time histories of the sick position and was deemed satisfactory at high speeds, but unsatisfactory at low speeds.

Dynamic oscillation tests were performed by assessing the aircraft response to stick pulse inputs. Longitudinal oscillations increased with duct angle, but were stable at all times. Similarly, lateral oscillations increased with duct angle (decreasing velocity) and were stable at all times. Note that no Dutch roll oscillations were noted by pilots during testing [16].

Transition to Hover

Traditionally, the transition from forward flight to hover is the most difficult task of any VTOL aircraft. In order to investigate the performance capabilities, flight tests were performed in steady-state descents and glide slope interceptions. Unlike takeoff transition, conversion to landing took upwards of one minute and required full nose down elevator to offset the large pitching moments from the ducts at flight speeds between 50-100 kts and duct angles of 30-60^o. Similarly large control

motions (upwards of 50-60%) were required to stabilize the aircraft when landing at a specified point, and were not attributed to pilot induced oscillations (PIO) [15].

In addition, cameras were used during transition to record tuft behavior on the right wing during various landing configurations and indicated significant susceptibility to outboard wing panel stall (Figs. 2.4a-2.4c). Major separation was noted at a descent rate of 600 feet per minute (Fig. 2.4c) and was partly attributed to the increased induced angle of attack at the outboard wing regions due to the presence of the duct. Consequently, various methods of landing were tested and it was found best to hold the aircraft at a fixed nose down attitude, while varying the duct angle as required to prevent airspeed changes. Analysis of transition corridors determined from flight test can be found in Ref. [17].

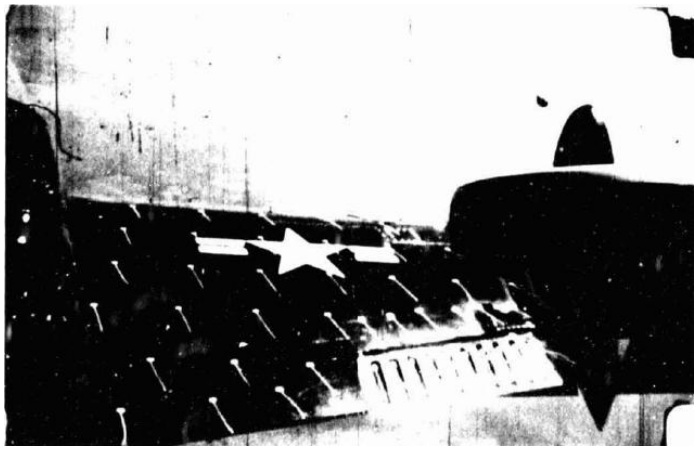

(a) Rate of descent = 0 feet per minute; $\delta_d = 60^o$ V = 37 kts.; $\alpha_w = 6.5^o$.

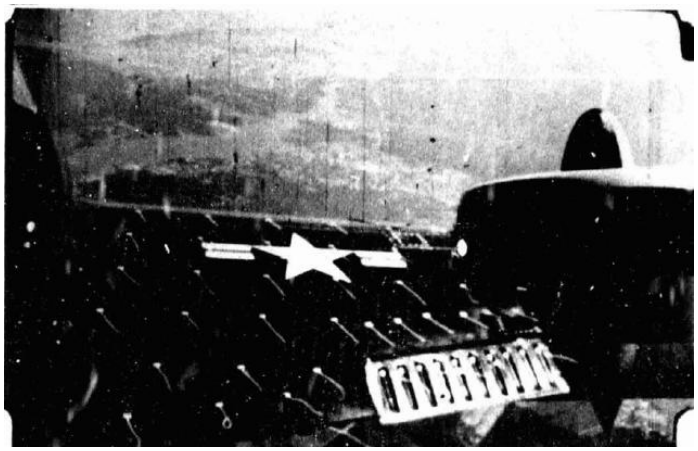

(b) Rate of descent = 300 feet per minute; $\delta_d = 60^o$ V = 37 kts.; $\alpha_w = 11.5^o$.

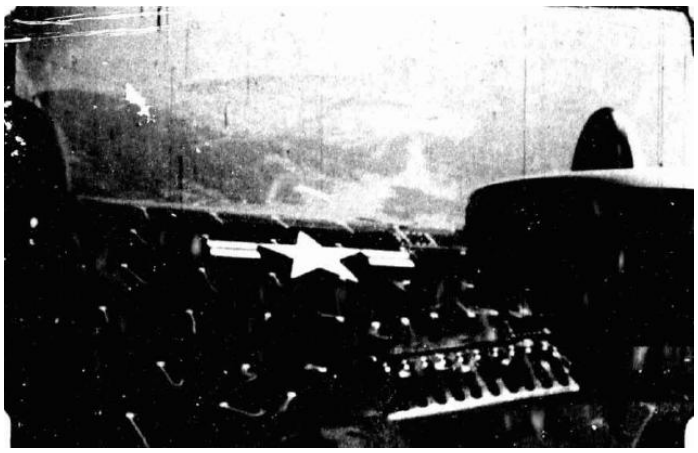

(c) Rate of descent = 600 feet per minute; $\delta_d = 60^o$ V = 37 kts.; $\alpha_w = 14.5^o$.

Figure 2.4: Flow over wing during steady-state descent at constant duct angle and airspeed and varying fuselage angle of attack and power (δ_d - duct tilt angle, V forward airspeed, α_w wing angle of attack)[16].

2.4 Stability Derivatives

Limited stability data on the VZ-4 at the hover condition was found in Ref. [18] and is presented in Tables 2.1-2.2. Note that this data is based on simplified analysis using momentum theory, and has no justification or validation.

Table 2.1: VZ-4 Longitudinal Hover Derivatives based on momentum theory.

M_u (ft-sec)$^{-1}$	M_q (sec)$^{-1}$	X_u(sec)$^{-1}$	$\frac{X_{\delta_e}}{M_{\delta_e}}$ (ft)$^{-1}$
0.014	-0.05	-0.14	0

Table 2.2: VZ-4 Lateral Hover Derivatives based on momentum theory.

L'_v (ft-sec)$^{-1}$	L'_p (sec)$^{-1}$	Y_v(sec)$^{-1}$	$\frac{Y_{\delta_a}}{L'_{\delta_a}}$ (ft)$^{-1}$
-0.014	-0.27	-0.14	0

Full lateral and longitudinal stability data obtained from Ref [19] is given in Appendix A and agrees well with the calculated values listed above using momentum theory.

Chapter 3

Model Scaling

3.1 Similitude

Early attempts at understanding the performance of aerodynamic bodies were investigated by Cayley, Lilinthal and Robins in the mid-to-late 1700s using a whirling arm balance. It was not until the late 1800s that Wenham, Maxim, and Phillips began to carry out tests using what would be considered the "modern" wind tunnel, whereby the test article remains stationary and the air is drawn through the test section. Like these early experiments, the data collected today still rely heavily on the use of subscale models to extrapolate full scale prototype behavior. As a result, extreme care must be taken in the design of the experiment and interpretation of the results. Correct application of subscale data requires that the flow be dynamically similar to the full scale prototype. The property of similitude is defined as having similar geometric streamline patterns, force coefficients, and distributions of V/V_∞, p/p_∞, & T/T_∞, when plotted against common nondimensional coordinates [20]. This occurs only when the nondimensional similarity parameters, or pi-terms, of the model and prototype are equal. For subsonic tests (Ma < 0.3) the similarity parameters of interest are the geometric scaling ratio and Reynolds number (Re). The first parameter is the easier of the two to maintain; however, proper scaling applies even to fine details like the surface finish, which can influence the location of

transition and separation in the boundary layer. Conversely, the Reynolds number is almost never matched in an unpressurized tunnel with air as the working fluid. This is because the freestream velocity varies inversely to geometric scale: consider investigating the aerodynamic performance of a full scale prototype at a freestream velocity of 160 mph using a $3/10^{th}$ scale model: the required tunnel speed to match Reynolds number would be a staggering 533 mph (Ma = 0.7)! Clearly such a flow would violate the incompressibility assumptions and result in significant changes of the underlying physics. As a result, the model was tested at a range of speeds representative of the full scale prototype. Such a model is said to be distorted in Reynolds number.

3.2 Scaling Ratio

Proper selection of a geometric scaling ratio must be made before a model can be built and tested in the wind tunnel. This decision is far from easy and requires careful attention to several competing requirements, which include: Reynolds distortion, wind tunnel wall effects, design for manufacture and assembly (DFMA), structural integrity, and available resources and funding.

The most important requirement in this list is Reynolds distortion because it affects the ratio of viscous to inertial forces between the model and prototype. This ratio is highly dependent on the transition point within the boundary layer, and is not guaranteed to be the same at the model scale. Consequently, trip strips are sometimes placed along the span and fuselage by an experienced tunnel engineer.

Due to the lack of full scale test data on the location of boundary layer transition, trip strips were not utilized during testing.

In addition, the interplay of wall effects and Reynolds number are particularly important when testing V/STOL models, as the low end transition speeds can result in unacceptably low Reynolds numbers and excessively large downwash angles. Reference [21] recommends model-span-to-tunnel-width ratios of 0.3-0.5, placing an upper limit the model span of 3.31-5.52 ft. As a result, a 3 ft span model ($3/10^{th}$ scale) was chosen.

Furthermore, the use of the wind tunnel imposes further testing limitations. The first restriction is that the walls of the tunnel affect the streamline curvature of the flow. In addition, introducing a model in the test section of the wind tunnel reduces the exposed cross sectional area, resulting in an increase in flow velocity around the model (due to the continuity equation) as compared to free air. Finally, wake blockage and horizontal buoyancy forces result in slight over predictions in drag. These affects were assumed to be negligible during testing.

3.3 Propulsion

The presence of propulsion systems on the aircraft has the potential of significantly affecting both stability and control. This is primarily a result of changes in the slipstream due to swirl components of wake from the ducts that modify the dynamic pressure, downwash, and cross-flow at the tail [15]. This effect is typically most pronounced at high power low speed settings, near takeoff. Furthermore, the

central mounted jet engine has the potential of entraining surround air near the tail due to the pressurized exhaust gasses, which in turn can modify the inflow at the tail. However, scaled propulsion systems were omitted in the wind tunnel model, due primarily to insufficient Reynolds number at the $3/10^{th}$ scale. As a result, the abovementioned effects are not captured in the data, but must be noted.

Chapter 4

Experimental Setup: Static Testing

4.1 Model Construction

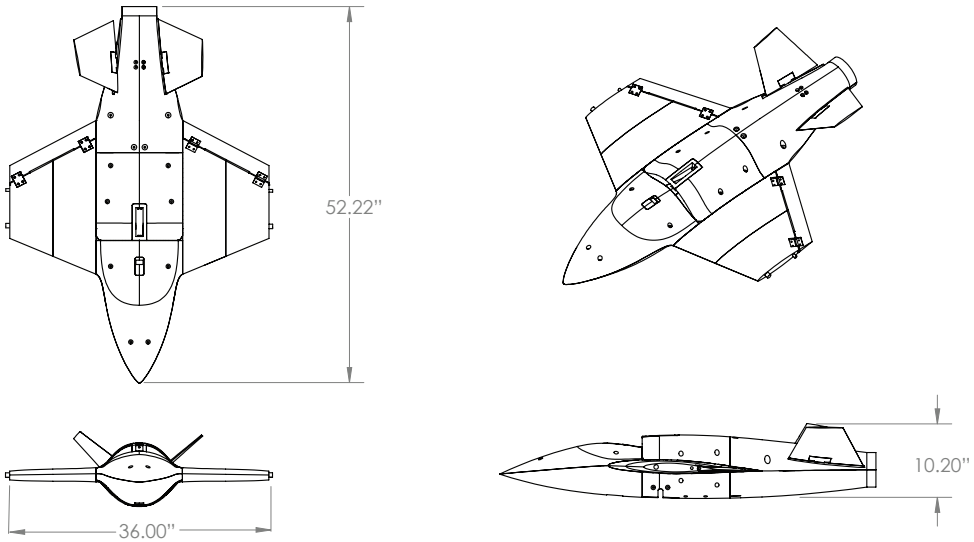

Figure 4.1: 3/10 Scale Wind Tunnel Model (Dimensions in inches)

A $3/10^{th}$ scale model was designed in the Solid Works environment by graduate student Scott Owen and undergrad Roberto Semidey, shown in Fig. 4.1. The materials used in construction were: Ren Shape 440 ($\rho = 34 lbf/ft^3$), Last-a-Foam FR-7120 ($\rho = 20 lbf/ft^3$), and 6061 aluminum stock. These are popular choices for fabrication and were selected because component parts could be made in-house at American Dynamics. Limitations on the maximum manufacturable part size resulted in the following subassemblies: wing, tail, nose, and mid/aft fuselage sections. Constituent parts and tooling, shown in Fig. 4.6a, were made using a Haas

4-axis VF2SS computer numeric controlled (CNC) vertical machining center with a tolerance of 0.001 in., which is within the 0.005 - 0.01 in. wing/fuselage contour accuracy recommended in Ref [21].

(a) Subassemblies w\tooling (b) R. Semidey working on bottom of fuselage mid-section (c) Duct centerline Pitot rake.

Figure 4.2: Model assembly

The lynchpin of the entire assembly is the bottom half of the fuselage mid-section, shown in Fig. 4.6b. Attachments to the wings, nose, empennage, and tunnel balance are located here. Two aluminum wing spars provide in-plane and torsional stiffness to combat aeroelastic effects. A bearing box located in the core of the mid-section serves as an attachment point to the wind tunnel balance and can be configured to allow model rotations in either pitch or yaw. Air data measurements were taken inside the central duct at a longitudinal station representative of the turboshaft compressor face. Static pressure was measured with four 1/16 in. diameter pressure taps equally spaced around the periphery of the inner duct walls. In addition, stagnation pressure at the centerline of the duct was measured using nine 1/16 in. diameter Pitot tubes connected to a rake, shown in Fig. 4.2c.

The process in finishing the surface was as follows: body filler, sanding, sanding sealer, paint, wet-sanding, gloss varnish, and wet sanding. The application of

sanding sealer was necessary because Last-a-Foam FR-7120 is highly porous and does not accept paint readily on its own. Thin layers of paint and sealer were used to prevent excessive build-up. Similarly, all sanding steps were carefully performed using 400 grit paper to avoid geometric distortions. Structural integrity was computationally validated by applying a uniform load distribution and locating the point of maximum stress. The factor of safety was calculated at 3.

It must be noted, several lessons were learned during the construction and testing of the model. First and foremost, the rigid connection of the control surface mounting brackets resulted in time consuming configuration changes with only discrete choices of deflection angles being permissible. For this reason, a hinged control surface with an adjustable linkage is recommended. Adding insult to injury, the bolts and washers used to attach the control surfaces protruded from the model. This can be seen at the root of the ruddervators and inside the duct on Figs. 4.3a-4.3b, respectively. Issues associated with the exposed bolts at the ruddervators were not deemed to be of substantial concern to the quality of the data. Examining the connection of flaperons to the wings in Fig. 4.3c, it is apparent that

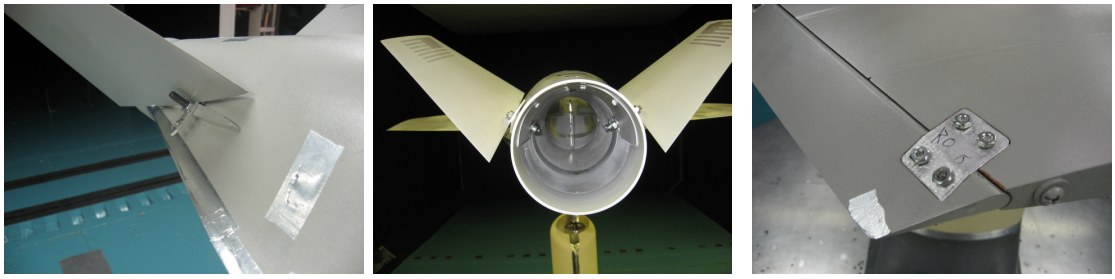

(a) Protrusion of ruddervator bolts near root.

(b) Protrusion of ruddervator bolts inside duct.

(c) Protrusion of flaperons mounting hex nuts on upper wing surface.

Figure 4.3: Control surface attachment inaccuracies.

the hex nuts protrude from the upper wing surface well into the boundary layer. The condition of the wing surface is one of the most important variables affecting drag [22]: smooth surfaces should be maintained even when extensive laminar flow cannot be expected. Furthermore, the gains of smooth surfaces are greatest for the NACA 6-series airfoils, which are found the model. Therefore, the control surface mounting brackets are a design error that should have been corrected by placing them on the *bottom* of the wing and having the hex nuts flush with the airfoil contour. Additionally, limited space inside the bearing box made model attachment and bearing reconfiguration a tedious process. It is recommended that ample space be provided to manipulate tools with full range of motion, and that all nuts and bolts be standardized to a single size. The guidelines for DFMA [23] should be consulted.

4.2 Design of Experiment

Stability and control of a $3/10th$ scale model of the AD-150 was determined from two weeks of testing at the University of Maryland's Glenn L. Martin wind tunnel (3/13/09–3/27/09). The closed circuit facility has: a 7.75' high x 11.04' wide test section, top speed of 230MPH (Ma = 0.3), 6 component yoke balance, and turbulence factor of 1.05[1]. Force coefficient data obtained from 72 static and 73 dynamic runs were compiled into lookup tables for use in nonlinear simulation. Dynamic testing did not include aeroelastic or spin characteristics: a description of the dynamic testing is given in Section 6.1.

[1] `http://windvane.umd.edu/research/facilities.html`

4.3 Measurement Instrumentation and Accuracy

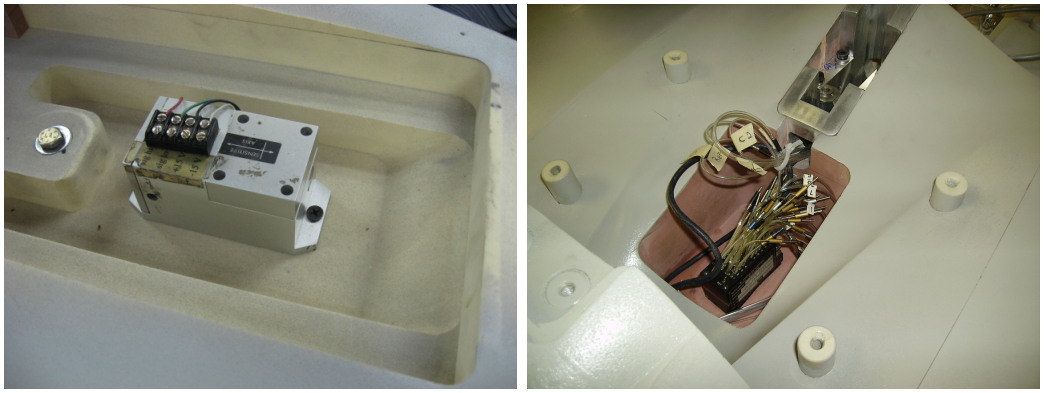

(a) Jewell Instruments LSO inclonometer (b) Pressure Systems 32HD pressure transducer

Figure 4.4: Static instrumentation.

Each force and moment coefficient collected during testing was subject to strict statistical convergence criteria in order to maintain a specified confidence level. A brief explanation this process follows below: for a complete discussion see Barlow, Rae and Pope [21]. During the measurement process, each data point is assumed to have a Student-t probability distribution. A running calculation is made of the sample mean $\bar{\mu}$ and standard deviation σ, which is then used to compute a 95% confidence interval. Maximum spread in the interval is specified by the tunnel operator at the start of each run and used as a 'target precision of the mean' for each balance component. While spread decreases about the mean as the number datapoints increase, this can result in excessively long tests before target precision is met. Consequently, a second constraint is imposed in the form of maximum number of datapoints collected. If the confidence bounds do not fall at or below the specified targets in the time alloted, the test is ended and the mean value is reported. Timming out of the system typically occurs during unsteady aerodynamic

conditions, such as stall or periodic vortex shedding. The sampling rate of the wind tunnel system was 8 Hz.

Model attitude measurements were made using a Jewell Instruments LSO inclonometer located inside the nose of the aircraft, shown in Fig. 4.4a. The inclonomter sensor specifications are given in Table C-1 of Appendix C. Heading angles were set by a stepper motor installed in the wind tunnel facility. A shaft encoder on the motor provided heading measurements and was assumed accurate to $\pm$ 0.1 deg due to blacklash in the gears and play in the connection of the model to the wind tunnel support.

Pressure measurements were made using a Pressure Systems 32HD pressure transducer. The transducer was placed within a small access compartment aft of the bearing box in the lower fuselage mid-section, shown in Fig. 4.4b. The accuracy of the pressure measurements are a function of both the transducer and data acquisition system (DAQ). Using a 1 psi transducer and PSI 8400 DAQ with 16 bit A/D converter, a pressure measurement accuracy of 0.1% FS was realized.

4.4 Tare and Interference

The first step in wind tunnel testing is correction for tare and interference effects resulting from the model supports. Tare corrections account for the aerodynamic drag produced from the exposed portions of the strut and pitch arm, shown in Fig. 4.5.

In order to minimize this drag, a floor mounted aerodynamic windshield covers

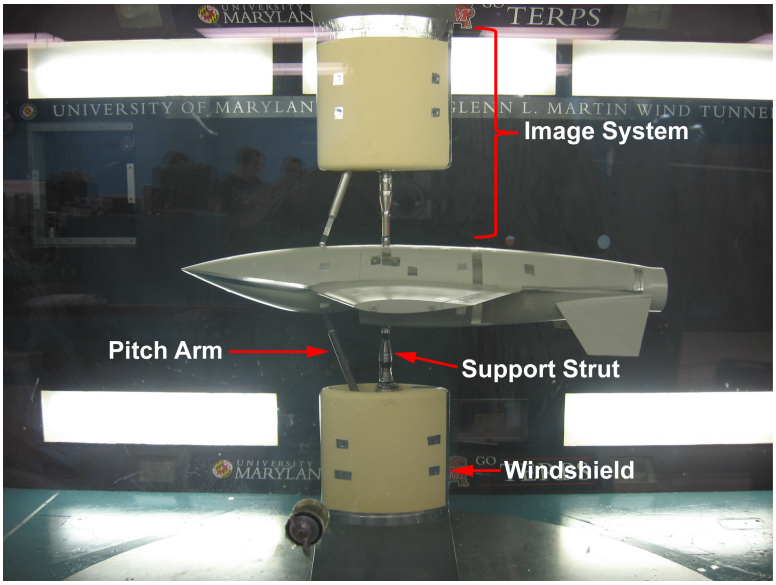

Figure 4.5: Inverted model with single-strut mounting and image system.

a majority of the strut. The windshield has a through-all hole along its centerline, preventing contact (and thus transmission of drag forces experienced by the windshield) with the strut. The hole also establishes a flow path between the wind tunnel test section and balance chamber; consequently, diaphragm seals are sometimes used to prevent inadvertent flow into the test section resulting from the reduced localized static pressures induced by the presence of the model. Note that the strut/pitch arm assembly rotates as a unit, driven by a motor in the balance chamber below the test section. In turn, the model rotates to a prescribed sideslip angle. Because the support strut rotates *relative* to the windshields, a sliding seal arrangement would have been needed. For the type of testing conducted this was not deemed necessary from both a practical or budgetary standpoint.

Another important complication of the model support is the interaction effects between the strut, pitch arm, and windshields on the airflow patterns around the model, and vice versa. This interaction affect is somewhat mitigated by the fact that

the support strut moves relative to the windshields, thereby keeping the windshields parallel to the freestream velocity at all times. Corrections for upflow and cross-flow of the tunnel and support structure were assumed negligible. Here again the type of testing and added time did not warrant such a procedure.

4.4.1 Test Procedure

A combined tare and interference test was used, requiring a total of three types of runs. First a series of normal model orientation runs were made, yielding:

$$D_{meas} = D_N + T_L + I_L \tag{4.1}$$

where D_{meas} is the measured drag force, D_N is the drag of the model in the normal position, T_L is the free air drag of the strut and pitch arm, and I_L is a combination of the interaction effects between the model/strut, strut/model, and lower windshield. Next the model was inverted and the test runs were repeated, giving:

$$D_{meas} = D_{inverted} + T_U + I_U \tag{4.2}$$

where the subscript 'U' denotes the inverted model state. Finally, with the model still inverted, a dummy support with a mock strut, pitch arm, and exposed electrical wiring identical to that of the lower support was installed. The exposed portion of the image strut was attached to the model, while clearance was left in the dummy supports. This was done to prevent the drag forces on the dummy strut and pitch

arm from being transfered to the upper windsheild. The resulting drag data measured was:

$$D_{meas} = D_{inverted} + T_L + I_L + T_U + I_U \tag{4.3}$$

The difference between Eqs. (4.3)-(4.2) is the sum of the tare and interference, $T_L + I_L$. Implicit to the image system methodology is that there are no mutual interaction effects between the top and bottom supports.

In addition to the test just described, a second no-wind tare test was performed to remove bias forces and moments attributed to the weight of the model. Ideally, the tare and interference procedures outlined should be repeated at each tunnel speed, angle of attack, sideslip angle, and model configuration. However, this would inevitably double the size of the test matrix and take an unacceptable amount of time. Instead, all tare test were performed with the model at a controls neutral configuration. The tunnel speeds used were 0 mph and 80 mph. The data collected from the 80 mph runs were applied to all tunnel speeds with the assumption that the tare coefficients obtained remained invariant to the range of Reynolds numbers tested. A complete test matrix of the tare & interference runs is given in Table 4.1.

Table 4.1: Tare & Interference Test Matrix

Run	V mph	θ (Pitch)	ψ (Heading)	Configuration
902	0	0	ψ_1	Upright
904	0	θ_3	0	Upright
1	80	0	ψ_1	Upright
908	0	θ_6	14	Inv. + Image
909	0	θ_6	0	Inv. + Image
910	0	θ_6	14	Inv. + Image
2	80	θ_5	14	Inv. + Image
3	80	θ_5	0	Inv. + Image
4	80	θ_5	14	Inv. + Image
6	80	θ_5	-14	Inv.
7	80	θ_5	0	Inv.
8	80	θ_5	14	Inv.
912	0	θ_7	0	Upright
913	0	θ_7	2	Upright
914	0	θ_7	4	Upright
915	0	θ_7	6	Upright
916	0	θ_7	7	Upright
917	0	θ_7	13	Upright

Notes:
θ_3 = (-2, -1.5, -1, -0.5, 0, 0.5, 1, 1.5, 2)
θ_5 = (-16, -15, -12, -11, -10, -8, -6, -4, -2, 0 , 2, 4, 5)
$\theta_6 = \theta_7$ = Random Variation
ψ_1= (-2, -1.5, -1, -0.5, 0, 0.5, 1, 1.5, 2)

4.4.2 Test Matrix

After completing the tare test, the model was configured to specific flaperon and ruddervator deflection angles. Next, the tunnel velocity was increased until dynamic pressure matched $\frac{1}{2}\rho_{STD}V^2$, where ρ_{STD} is sea level density on a standard day[2] and V is the freestream velocity in the test matrix. Consequently, variations in density due to temperature, pressure and humidity resulted in variations of tunnel

[2]Standard conditions are defined as: $T_0 = 59^o$F, $p_0 = 2116.4lb/ft^2$, $\rho_0 = 0.002378\ slug/ft^3$

velocities to sustain a constant dynamic pressure. The model then underwent a sweep in pitch θ and heading ψ angles. This process was repeated for various model configurations, sweep profiles, and tunnel speeds: ranging from transition (50 mph), to forward flight (160 mph). At the end of each sweep the first wind-on and wind-off runs were repeated to ensure balance drift limits were below 0.2% maximum reading. An abbreviated test matrix is given in Table 4.2, while a detailed version can be found in Appendix B.

Table 4.2: Abbreviated Test Matrix

Tunnel Speeds	50 mph – 160 mph
Reynolds Number	$0.665[10^6]$ – $2.13[10^6]$
Angle of Attack (α)	-4^o – 15^o
Sideslip Angle (β)	$\pm 13^o$
Ruddervator (Pitch)	$\pm 45^o$
Ruddervator (Yaw)	$\pm 45^o$
Flaperons (Roll)	$\pm 45^o$
Flaperons (Flap)	0^o – 45^o
Dynamic Testing	–

4.5 Aerodynamic Conventions

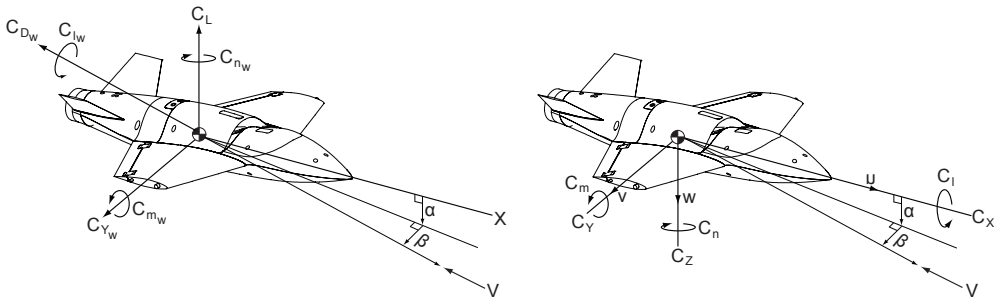

(a) Wind Axis (b) Body Axis

Figure 4.6: Aerodynamic reference frames.

Throughout this paper both wind and body axis conventions will be used; therefore, a definition of positive forces, moments, and angles for each case is shown in Fig. 4.6. Conversion between the wind and body axis are given below, for a derivation see Refs. [21],[26].

Force conversion:

$$\begin{bmatrix} C_L \\ C_{D_w} \\ C_{Y_w} \end{bmatrix} = \begin{bmatrix} C_X \sin\alpha - C_Z \cos\alpha \\ -C_X \cos\alpha \cos\beta - C_Y \sin\beta - C_Z \sin\alpha \cos\beta \\ -C_X \cos\alpha \sin\beta + C_Y \cos\beta - C_Z \sin\alpha \sin\beta \end{bmatrix} \tag{4.4}$$

Moment conversion:

$$\begin{bmatrix} C_{l_w} \\ C_{m_w} \\ C_{n_w} \end{bmatrix} = \begin{bmatrix} C_l \cos\alpha \cos\beta + C_m \sin\beta + C_n \sin\alpha \cos\beta \\ -C_l \sin\beta \cos\alpha + C_m \cos\beta - C_n \sin\alpha \sin\beta \\ -C_l \sin\alpha + C_n \cos\theta \end{bmatrix} \tag{4.5}$$

Static wind tunnel data in Section 5.1 is reported in the wind axis, as direct performance calculations can be made from the graphs. Conversely, the nonlinear simulation lookup table values are in the body axis, which lend to direct stability analyis. Controls deflections follow the right hand rule: positive elevator deflection is trailing edge down, positive rudder deflection is trailing edge left (as viewed from behind), positive flap deflection is trailing edge down, and positive ailerons are one half the right aileron deflection (trailing edge down) minus left aileron deflection (trailing edge up), or: $\frac{1}{2}(\delta_{aR} - \delta_{aL})$.

Chapter 5

Experimental Results: Static Testing

5.1 Introduction

A total of 70 static wind tunnel tests were conducted to gather insights on stability and control, while simultaneously validating CFD results generated by American Dynamics using CD-adapco's STAR-CCM+ software: a Reynolds-Averaged Navier-Stokes (RANS) solver with a K-Epsilon turbulence model. Mesh dependency studies were performed to find an optimal polyhedral grid spacing that was computational inexpensive, while simultaneously producing minimal change in the resultant force coefficients. Validation with the experimental results provided a greater level of confidence in making predictions at flight Reynolds number using the optimized mesh, allowing for future prototype performance estimates to be made without resorting to prohibitively expensive experimentation methods. The inherent assuption in using an 'optimal' mesh at various Reynolds numbers is that no local refinements are necessary as the Reynolds number changes. Furthermore, because the mesh is constant, any changes in the force and moment coefficients are attributable soley to Reynolds number. Tests and comparisons were performed at four tunnel speeds (50, 80, 110, 160 mph), while high speed analysis (200 mph) was performed predictively in CFD alone. The effect of wing tip ducts and the turboshaft engine are not included in the analysis.

An important note of caution is in order when interpreting the static data in this section. At first glance it may appear that the sideslip angles tested were exclusively negative. This is a byproduct of the wind tunnel using the convention of an earth fixed frame, where the rotation angles are in yaw ψ, pitch θ, and roll ϕ. The convention used in flight dynamics is angle of attack α and sideslip β. For all test runs $\phi = 0$; therefore, $\theta = \alpha$ and $\psi = -\beta$. This explains the abundance of negative sideslip angles in the plots given in the following sections.

5.2 Flow Visualization

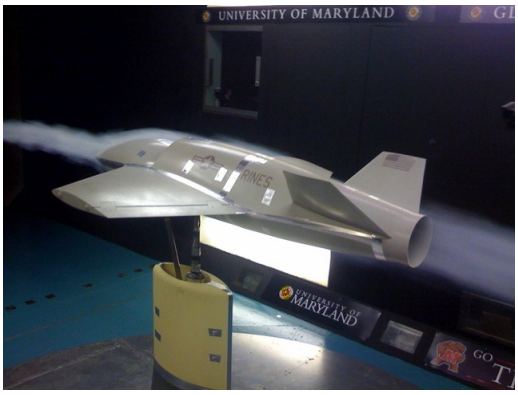

Figure 5.1: Flow visualization at nose stagnation point.

In order to investigate flow separation on the wings and fuselage of the model, propylene glycol vapor was introduced upstream of the test section using a handheld wand, shown in Fig. 5.1. As the model swept through various pitch and side slip angles, no adverse behaivor was observed. Separation occured for pitch angles above 10^o, as indicated by the wind tunnel and CFD data. Tufts were not used during testing.

5.3 Longitudinal Trim Coefficients

Variation of the wind frame longitudinal static coefficients (C_L, C_D, C_{m_w}) are presented in this subsection. In all plots the abscissa is the angle of attack-α, and contours are constant in sideslip-β. Throughout testing no structural flutter was visually observed, which accurately represents the prototype because drive shafts within the wing limit angular misalignments no greater than 5^o.

5.3.0.1 Lift

The lift coefficient plots, shown in Fig. 5.2, are invariant to both sideslip and airspeed. CFD (solid line) slightly over predicts the linear lift slope as compared to experimental wind tunnel (WT) data points. The WT and CFD curves cross at $\alpha = 6^0$, with stall occurring at $\alpha = 11^0$. The critical stall angle is based on the moment curve of Fig. 7.11. Post stall experimental behavior gradually continues to increase and peaks at $C_{L,max} = 1.5$. An empirical correction for maximum lift coefficient when extrapolating from tunnel $Re = 1.5 \times 10^6$ to prototype $Re = 6 \times 10^6$ is $\Delta C_{L,max} = 0.15$ [21]. This correction means the actual maximum lift coefficient can be as large as $C_{L,max} = 1.65$. Drop-off ($\alpha > 11^o$) was not predicted well; however, correlation for $\alpha \leq 11^o$ is excellent. Experimental zero lift occurred at $\alpha = -3^o$. Note that the slopes shown are for steady conditions: transients in the form of time rates of change in angle of attack prevent the boundary layer from fully developing and can cause a further increase in $C_{L,max}$ [22].

5.3.0.2 Drag

The variation of the drag coefficient is shown in Fig. 5.3. Below stall ($\alpha \leq 11^o$) a second order trend exists and CFD overestimates experiment; conversely, CFD significantly under estimates experiment in the post stall region. This indicates that the experimental data has extensive region of laminar flow in the boundary layer towards the front of the wing, whereas the CFD data treats this region as primarily turbulent. At higher angles of attack, the assumption of a larger turbulent region in CFD may result in the flow remaining attached longer as compared to experiment, thus explaining the under prediction of drag. The drag increases with increasing magnitude[1] of sideslip, as indicated by arrow. Post stall variation to sideslip shows an increase in drag with increasing tunnel speed. Minimum drag, $C_{D,min} = 0.0269$, occurs at ($\alpha = -3.8^o$, $\beta = 0^o$). Drag corresponding to $C_{L,max}$ is $C_D = 0.1787$. Finally, variation to tunnel speed is negligible below stall. Note that no efforts were made to determine the components of parasitic and induced drag because the goal of testing was to generate aerodynamic databases for simulation.

5.3.0.3 Pitching Moment

The variation of the pitch moment coefficient, shown in Fig. 7.11, increases in magnitude of sideslip angle, as indicated by arrow. A linear trend appears until stall, where a sudden and precipitous drop-off occurs. Moment stall occurrs before lift stall, and is typical on low aspect ratio wings and lifting bodies where classic 2-D

[1]Recall that the graph shows *negative* of sideslip angles, explaining why drag decreases with increasing sideslip.

airfoil characteristics are invalid. Post stall sensitivity to sideslip is greatest at 50 mph, as shown in Fig. 5.4a. Comparatively, the slope and sideslip variation is larger for CFD than experiment in the linear range. Prediction of stall at $\alpha = 11^0$ agrees well with experiment for high magnitude sideslip angles across all tunnel speeds, but the drop-off is wanting. Below $\beta = -9^o$, CFD fails to predict stall entirely.

The pitch stiffness, defined as the rate of change in pitch moment with respect to angle of attack-C_{m_α}, is clearly positive, and therefore statically unstable. As a result, stability augmentation had to be achieved prior to dynamic oscillation testing. This was done through the use of a linear extension spring (see Section 7.2). Finally, variation with tunnel speed below stall is negligible.

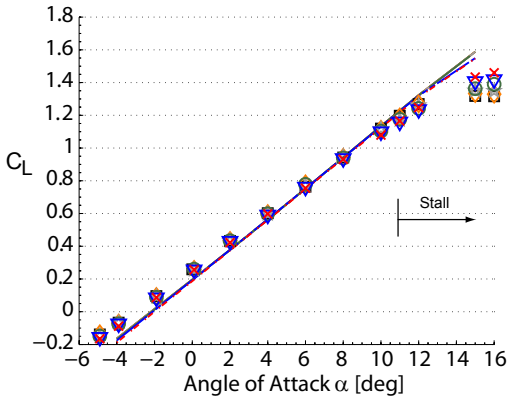

(a) V= 50 mph

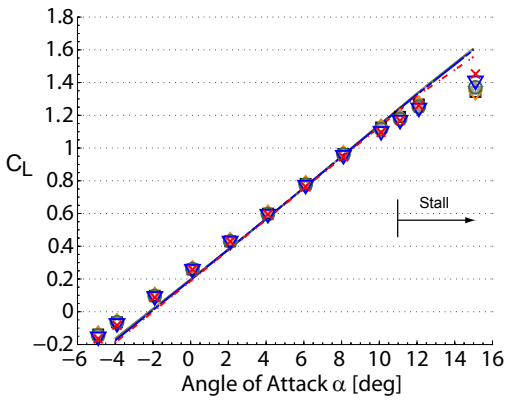

(b) V= 80 mph

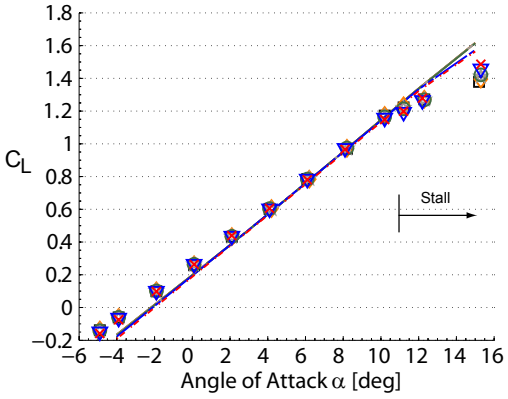

(c) V= 110 mph

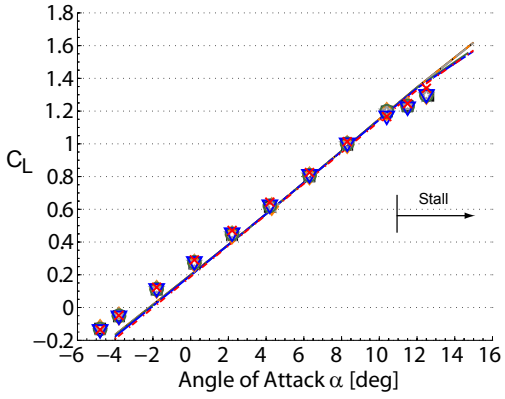

(d) V= 160 mph

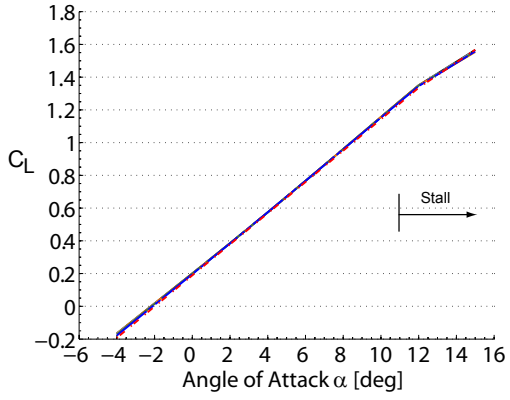

(e) V= 200 mph

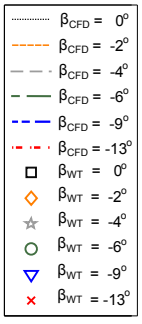

(f) Legend

Figure 5.2: Lift Coefficient

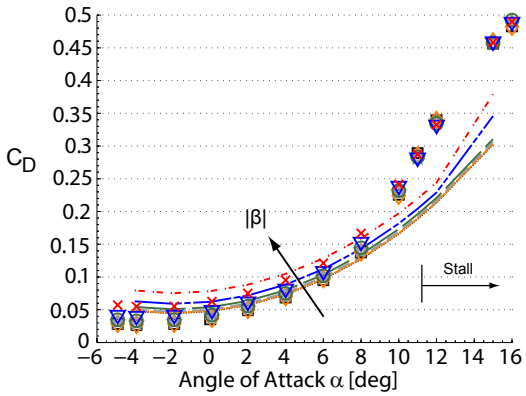

(a) V= 50 mph

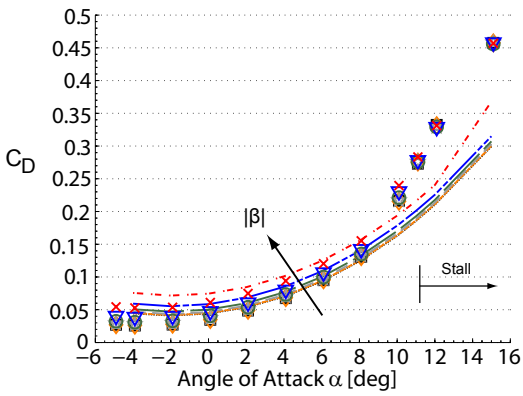

(b) V= 80 mph

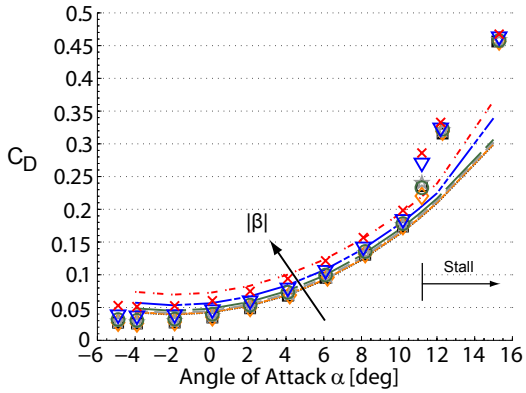

(c) V= 110 mph

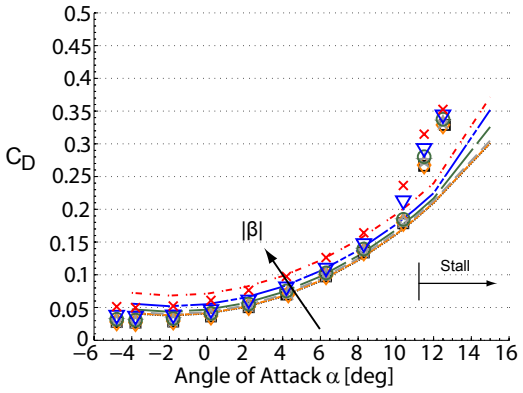

(d) V= 160 mph

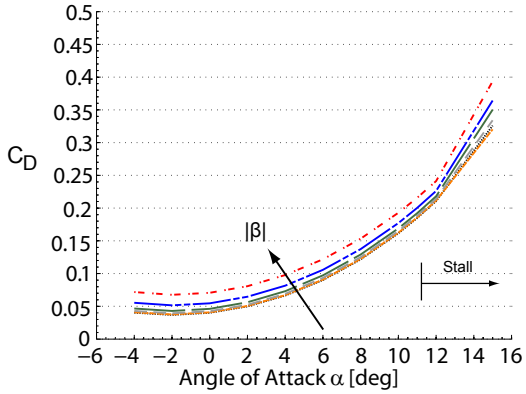

(e) V= 200 mph

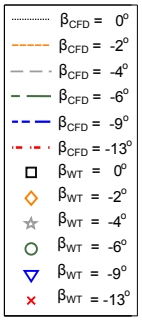

(f) Legend

Figure 5.3: Drag Coefficient

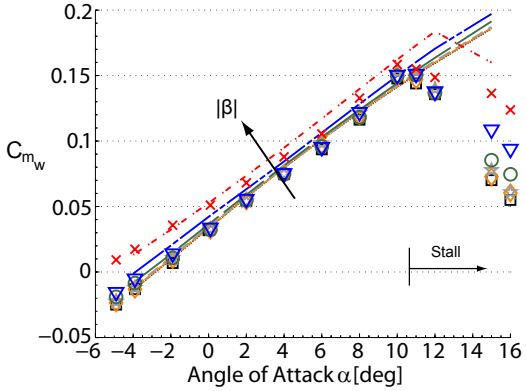

(a) V= 50 mph

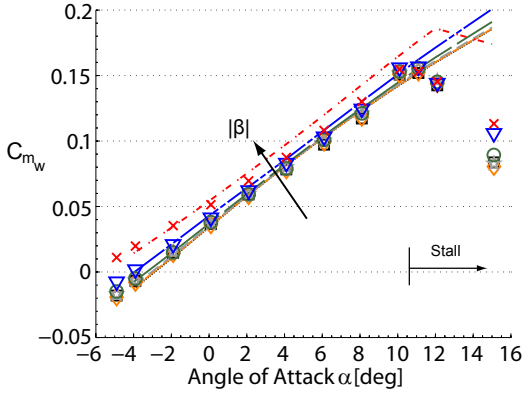

(b) V= 80 mph

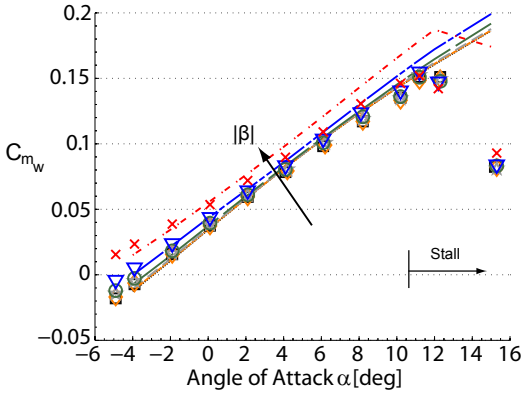

(c) V= 110 mph

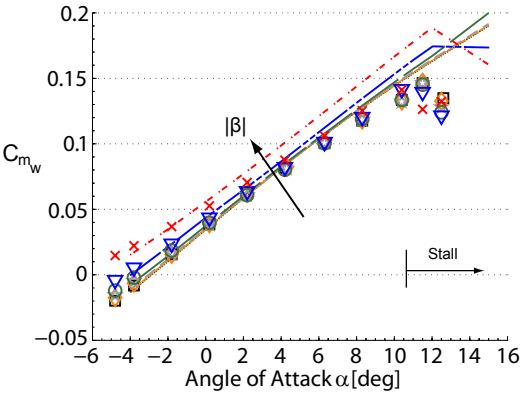

(d) V= 160 mph

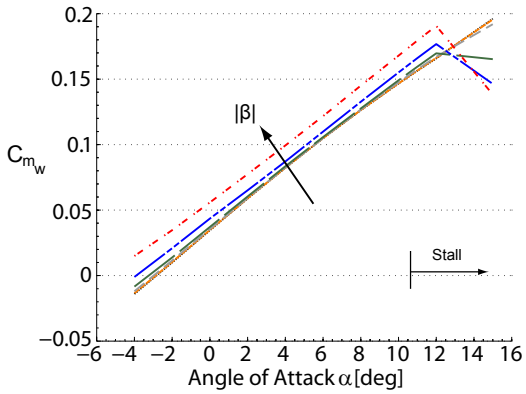

(e) V= 200 mph

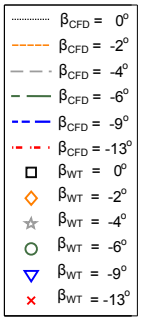

(f) Legend

Figure 5.4: Pitch Momement Coefficient

5.4 Lateral Trim Coefficients

Variation of the lateral static coefficients (C_{Y_w}, C_{l_w}, C_{n_w}) are presented in this subsection. In all plots the abscissa is the sideslip β, and contours are constant angle of attack α. Select values of angle of attack are plotted for clarity. Characteristic of all lateral plots are small nonzero force and moment coefficients when $\beta = 0^o$. These nonzero values are a possible result of: asymmetric flow in the tunnel, model asymmetry, or hysteresis due to small separation areas [21].

5.4.0.4 Side Force

Side force plots are given in Fig. 5.5, and was the only aerodynamic coefficient to show mild variability to tunnel speed. As per a conventional aircraft design, the side force is positive for negative sideslip angles. As tunnel speed increases, the spread in angle of attack decreases for the experimental data. CFD has a large discrepancy in variation with angle of attack, and rate of change with respect to sideslip-C_{Y_β}. Post stall ($\alpha = 11^o, 15^o$), the experimental data shows a dramatic drop in side force. Note that for $\beta = 0^o$ the side force takes on nonzero values, despite being a symmetric condition.

5.4.0.5 Roll Moment

Roll moment plots are given in Fig. 5.6. A modest correlation between CFD and experiment can be seen for $\alpha \leq 11^o$. Behavior at stall is significant below 80 mph and highly nonlinear. Roll stiffness, defined as the rate of chage in roll moment

with respect to sideslip, is seen to be negative and indicates static stability. The stability in roll to sideslip can be traced back to the wing sweep and ruddervators, both of which create stabilizing roll moments when perturbed from equilibrium. The wing sweep creates a dihedral effect by increasing the component of chord-wise flow for the wing aligned with the wind, while the vertical tail produces a restoring torque because its center of pressure is above the aircraft cg [28, 25].

5.4.0.6 Yaw Moment

Yaw moment plots are given in Fig. 5.7. Correlation between CFD and experiment is low for all tunnel speeds. Yaw stiffness, also known as directional or weathercock stability and defined as the rate of change in yaw moment with respect to sideslip-$\frac{\partial C_{n_w}}{\partial \beta}$, is seen to be positive and indicates static stability. Any perturbations from trim will return to equilibrium, resulting from the side force generated by the tail and fuselage: known as the keel effect [29]. In Figs. 5.7a-5.7b, the slope of the experimental data progressively increases up to $\alpha = 8^o$. For $\alpha \geq 11^o$ there is a significant diminish in slope resulting from stall, indicating a sudden decrease in directional stability.

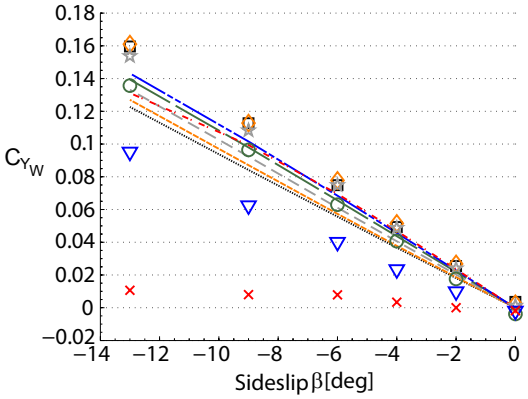

(a) V= 50 mph

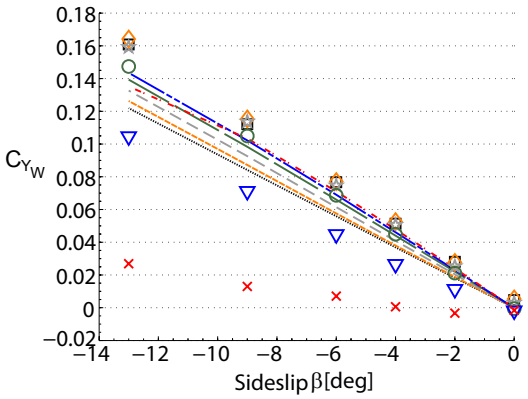

(b) V= 80 mph

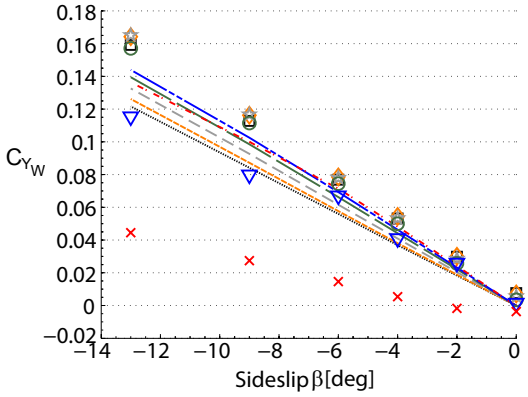

(c) V= 110 mph

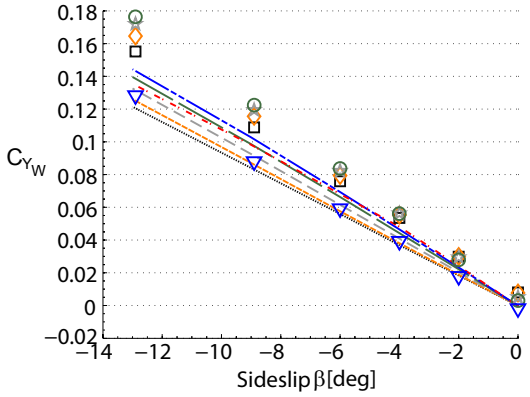

(d) V= 160 mph

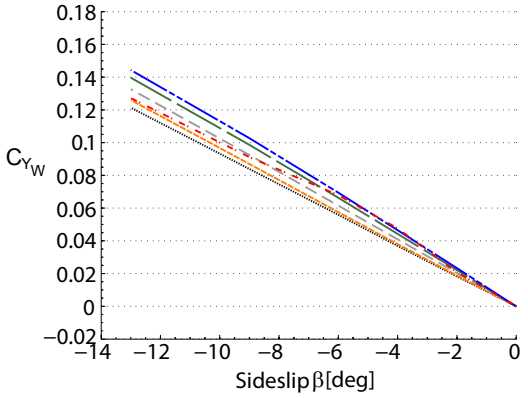

(e) V= 200 mph

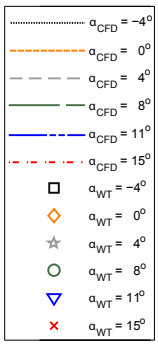

(f) Legend

Figure 5.5: Side Force Coefficient

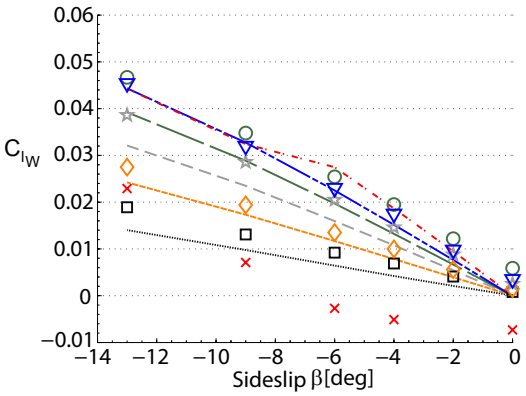

(a) V= 50 mph

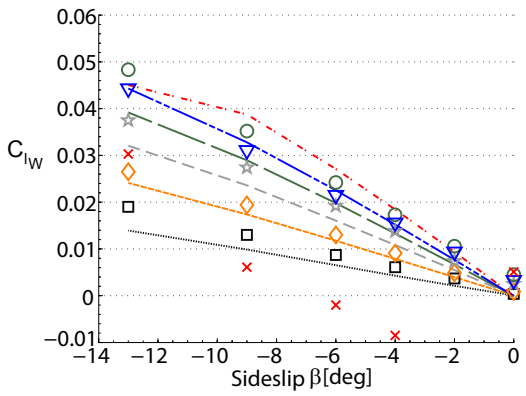

(b) V= 80 mph

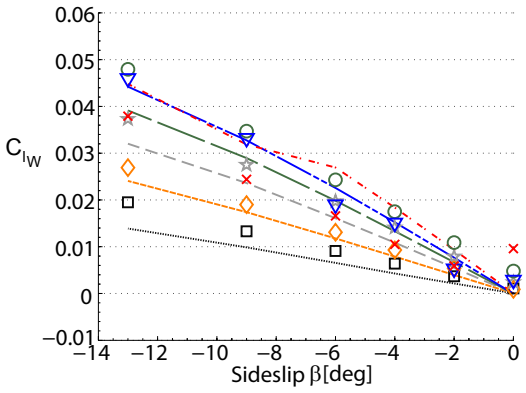

(c) V= 110 mph

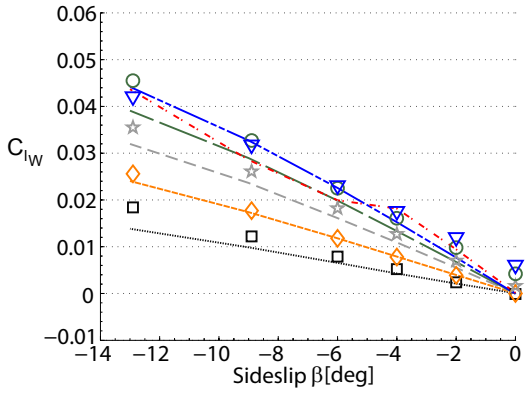

(d) V= 160 mph

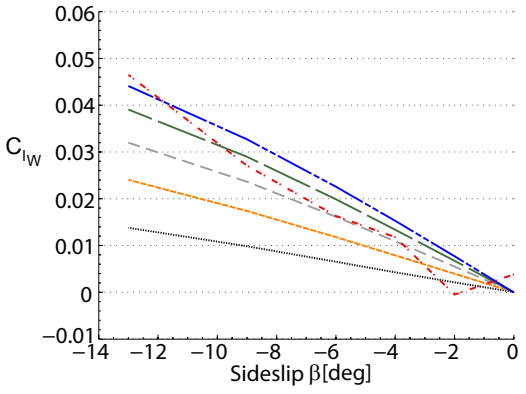

(e) V= 200 mph

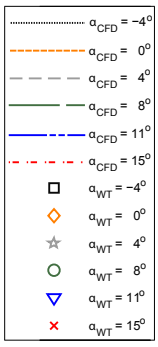

(f) Legend

Figure 5.6: Roll Coefficient

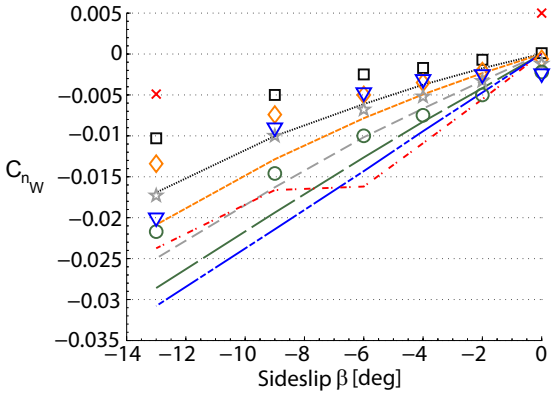

(a) V= 50 mph

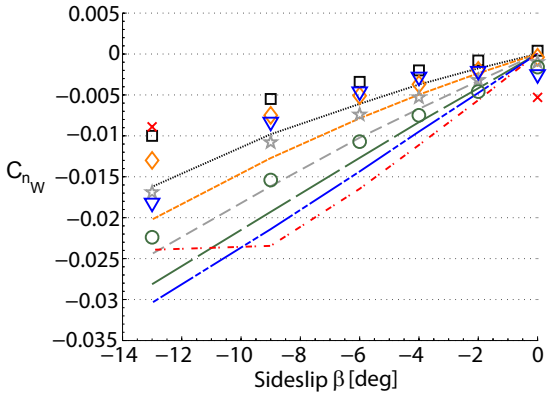

(b) V= 80 mph

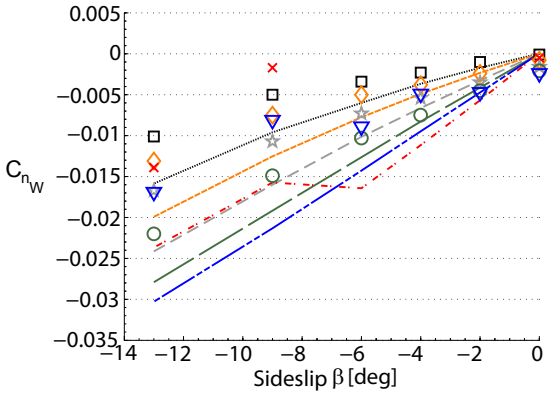

(c) V= 110 mph

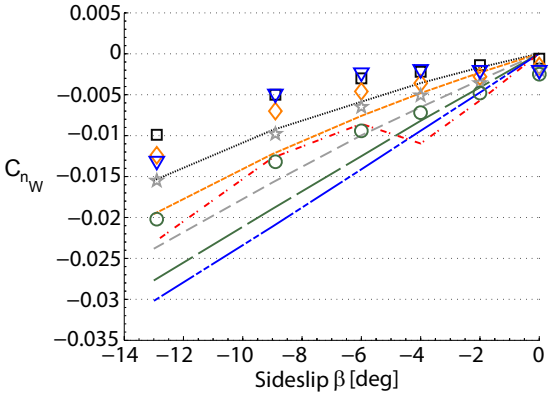

(d) V= 160 mph

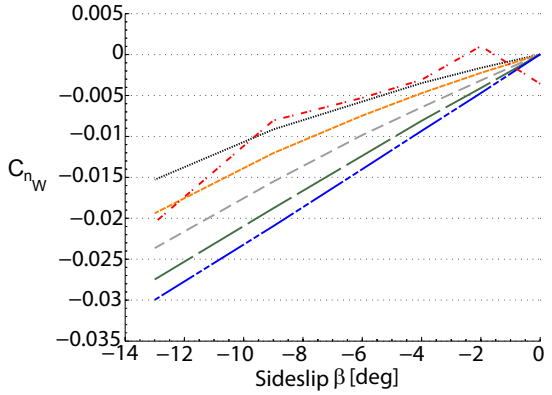

(e) V= 200 mph

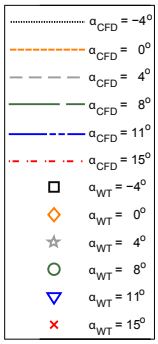

(f) Legend

Figure 5.7: Yaw Coefficient

5.5 Controls Deflections

Any successful vehicle design requires controllability in all three axis. Control typically occurs through the use of ailerons, elevator, rudder, and flaps. Note that the ailerons differ functionally from the other controls because they are *rate* controls, whereas elevators, rudders, and flaps are *displacement* controls [25]. All controls tests were performed at 110 mph and assumed invariant to tunnel speed based on the low sensitivity of the lateral and longitudinal plots in Sections 5.3-5.4. CFD analysis of the control deflection cases were not completed in time to make comparisons to experiment; however, trends are expected to follow suit with those in the previous section.

5.5.1 Flaperons: High Lift Device

The effects of flaperons when used as a high lift device[2] are given in Fig. 5.8. Because the flaps also double as ailerons, they can be regarded as a plain flap design. Flap extension in Fig. 5.8a indicates a uniform increase in lift coefficient with angle of attack, while preserving lift slope-C_{L_α}. Maximum lift coefficient ranges between $C_{L,max} = 1.22 - 1.84$ for $\delta_f = 0^o - 45^o$, respectively. Historically the value of $C_{L,max}$ at full scale Reynolds number is larger than experiment by as much as 0.2. However, low-aspect ratio wings with sweep have a leading-edge vortex that is relatively insensitive to Reynolds numbers near $Re = 2 \times 10^6$; therefore, the discrepancy in maximum lift is expected to be only slightly larger in flight than

[2]All tests were performed at $\beta = 0^o$.

experiment [21]. As expected, the drag curves increase with flap deflection, while simultaneously causing a substantial decrease in the pitch moment. The lateral coefficient plots of Figs. 5.8c,5.8d, 5.8f indicate low sensitivity to flap deflection. Finally, note that flaps increase the vorticity in the wake, which can affect control effectiveness at the tail. However, due to limited time combined flap-rudder/elevator tests were not performed.

5.5.2 Ruddervators: Pitch

Elevator control cross-plot are given in Fig. 5.9. Moving across each row shows the variation in the aerodynamic coefficients with sideslip angle. Select angle of attack contours are shown in each subplot for clarity. The longitudinal plots of Figs. 5.9a-5.9i show very little dependence to sideslip angle, whereas the angle of attack contours differ by a constant bias. The lift and drag curves increase, as expected, with positive elevator deflections, and are insensitive to sideslip. The pitch moment curves indicate that a linear approximation for $\delta_e = \pm 15^o$ is justifiable. Control surface stall occurs for $\delta_e = 15^o$,$\delta_e = \pm 30^o$ when $\beta = 0^o$ and $\beta = -6^o, -13^o$, respectively. From the pitch data, it is recommended that the elevator control saturation limits be $\delta_e = \pm 15^o$.

Variation of the lateral coefficients in Figs. 5.9a-5.9r show a strong correlation to sideslip. Side force has a weak dependence on angle of attack, with the exception of $\beta = -13^o$ in the post stall region ($\alpha \geq 11^o$). In addition, the side force is symmetric with elevator deflection. Coupling with the roll axis, shown in Fig. 5.9o,

has a bias offset for variation in angle of attack, but changes in functional form with sideslip. Coupling is most predominant for negative elevator deflections, with perturbations as large as $\Delta C_l = -0.064$ between $\delta_e = 0^o$ and $\delta_e = -45^o$. This is equivalent to approximately $\delta_a = 22^o$ of aileron deflection, as seen in Fig. 5.11i: a non-trivial amount! The yaw moment plots of Figs. 5.9p-5.9r show a similar dependency to sideslip. The $\beta = -13^o$ plot in Fig. 5.9r indicates a yaw perturbation of $\Delta C_n = 0.037$ between $\delta_e = 0^o$ and $\delta_e = -45^o$, which is equivalent to $\delta_r = -6^o$ in Fig. 5.12p.

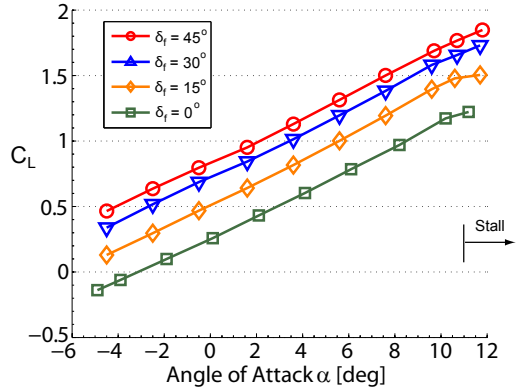

(a) Lift

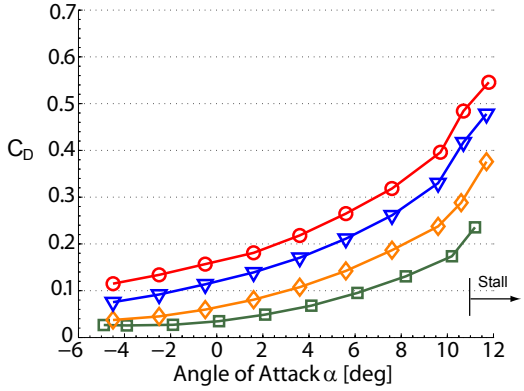

(b) Drag

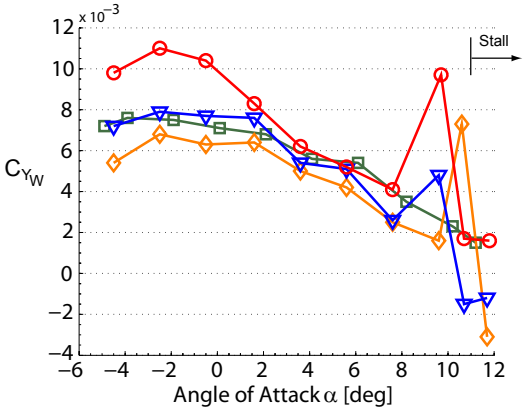

(c) Side Force

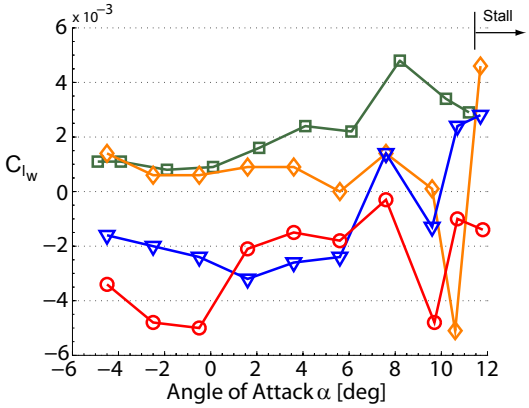

(d) Roll Moment

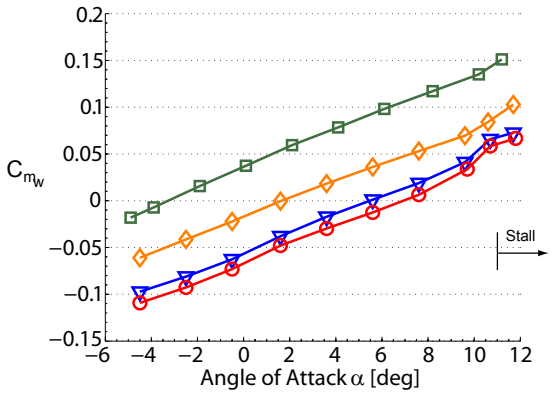

(e) Pitch Moment

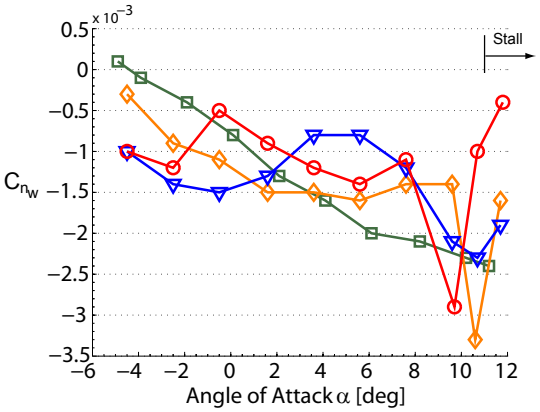

(f) Yaw Moment

Figure 5.8: Flap Deflection: V = 110 mph, $\beta = 0^o$

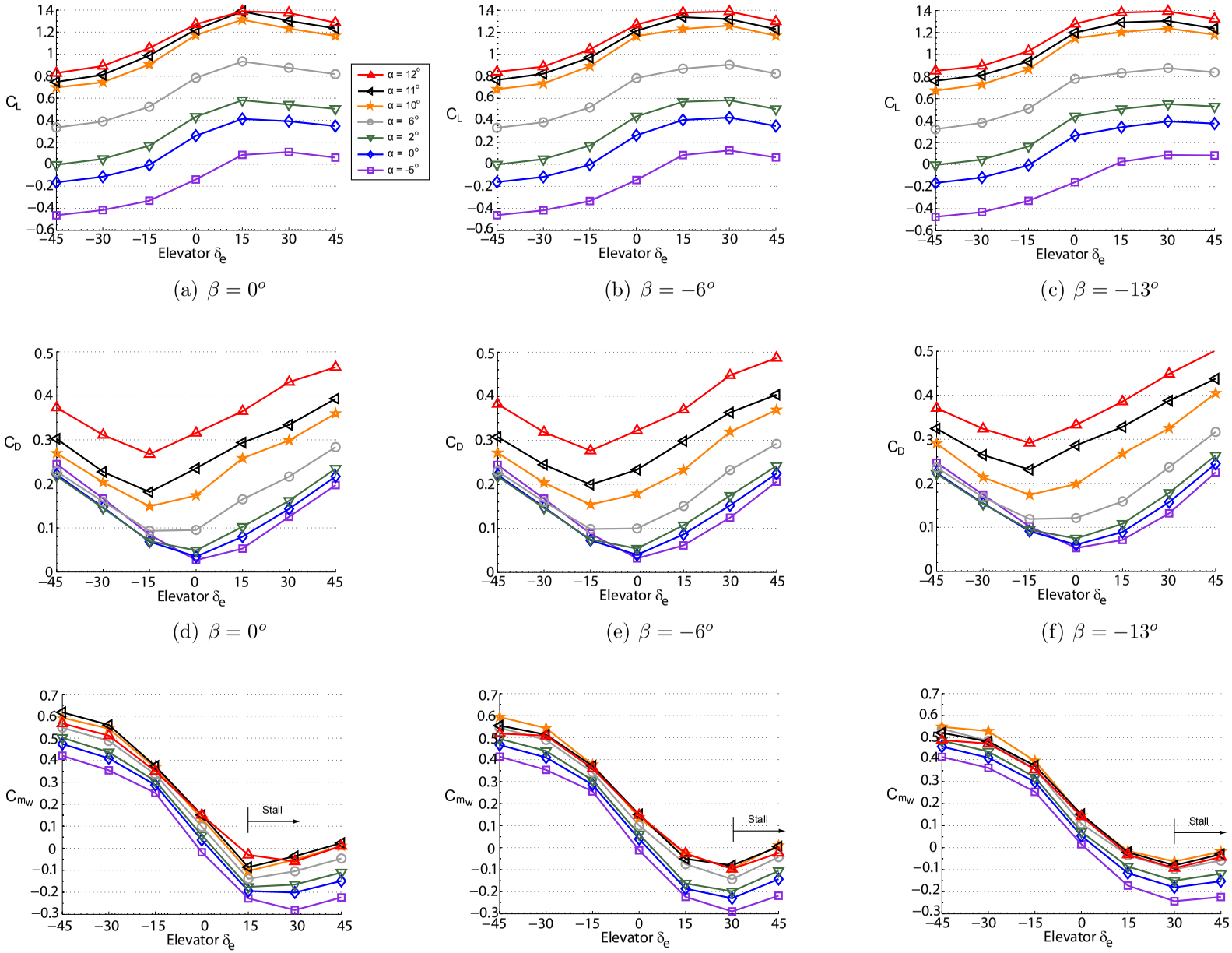

(a) $\beta = 0^o$ (b) $\beta = -6^o$ (c) $\beta = -13^o$

(d) $\beta = 0^o$ (e) $\beta = -6^o$ (f) $\beta = -13^o$

(g) $\beta = 0^o$ (h) $\beta = -6^o$ (i) $\beta = -13^o$

Figure 5.9: Elevator Control Power (Longitudinal): V = 110 mph

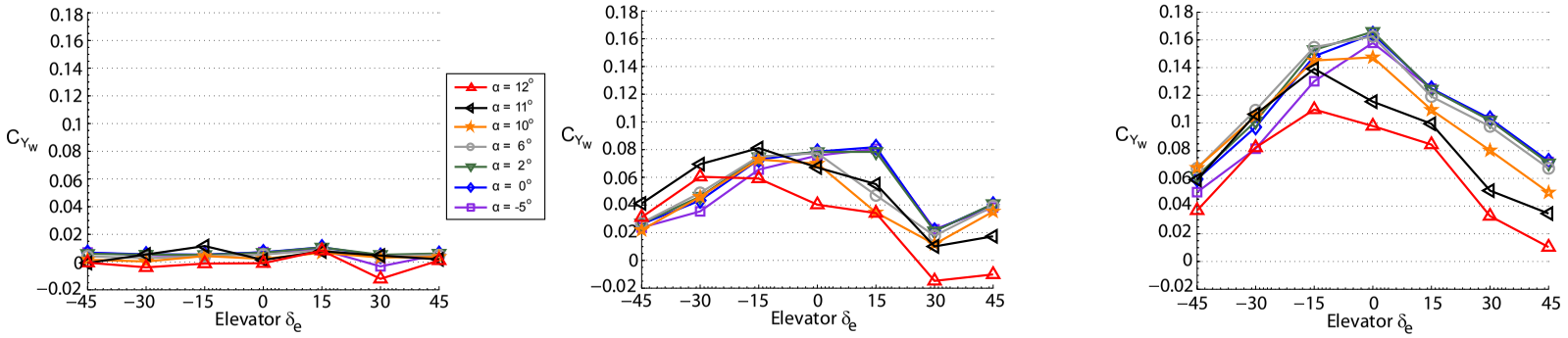

(j) $\beta = 0^o$ (k) $\beta = -6^o$ (l) $\beta = -13^o$

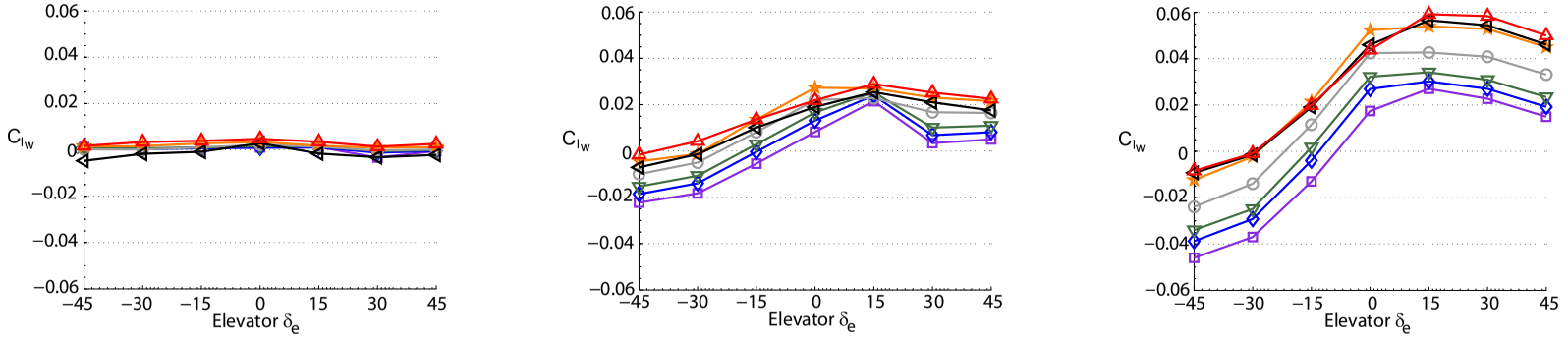

(m) $\beta = 0^o$ (n) $\beta = -6^o$ (o) $\beta = -13^o$

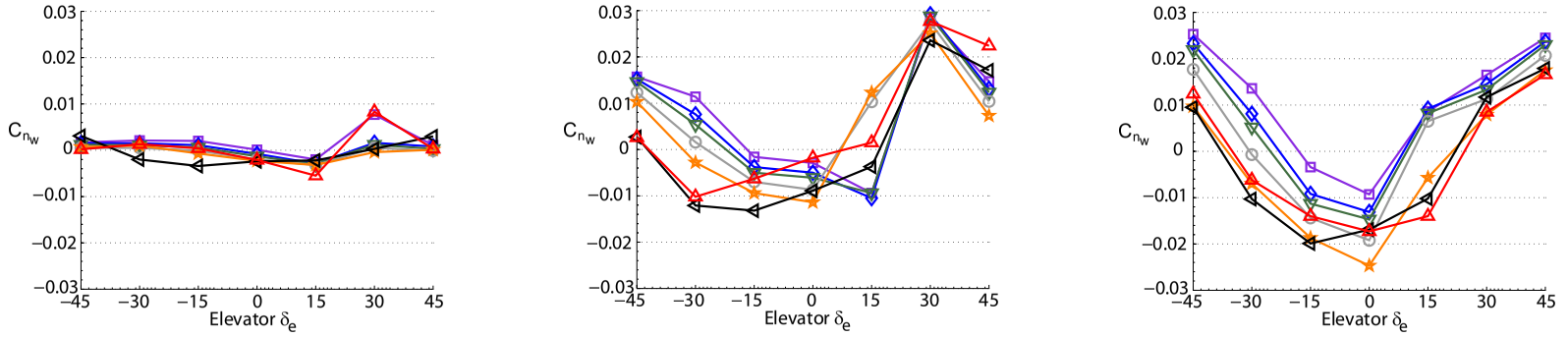

(p) $\beta = 0^o$ (q) $\beta = -6^o$ (r) $\beta = -13^o$

Figure 5.9: Elevator Control Power (Lateral): V = 110 mph

5.5.3 Reflection Method

A brief interlude is necessary on reflecting test data to construct the lateral control power plots. These plots have the aerodynamic coefficients as the ordinate and control deflection angle as the abscissa. This poses a problem because during aileron and rudder testing the model was subjected to a sideslip sweep of $\beta = \pm 13^o$; however, controls neutral runs were only performed between $\beta = -13^o - 0^o$. Lack of data between $\beta = 0^o - 13^o$ meant it had to be reconstructed indirectly.

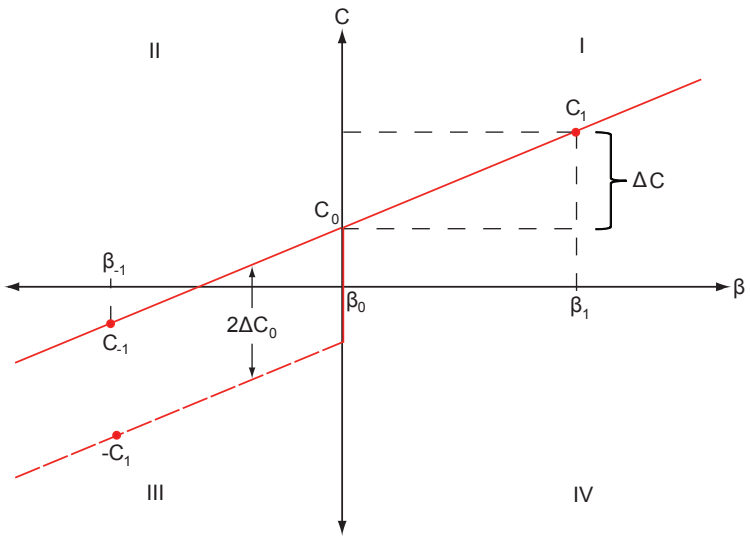

Figure 5.10: Reflection Method

The first observation to note about reflecting the data is that the longitudinal coefficients (*controls neutral*) are insensitive to the sign of the sideslip angle. Furthermore, the lateral coefficients do not undergo a simple sign change that follows suit with sideslip angle. Consider the exemplar aerodynamic curve shown in Fig. 5.10. The data is assumed to be collected at positive sideslip angles that lay quadrant I. The task is to reflect the data to negative sideslip angles in quadrant III. Simply changing

the sign of the coefficient associated with β_1 will produce a new point $-C_1$ that has an error *two times* the zero intercept: $\epsilon = 2\Delta C_0$. The correct method of reflection is to calculate the perturbation from the zero intercept, $\Delta C = C_1 - C_0$, and subtract it from the intercept itself, yielding:

$$C_{-1} = 2C_0 - C_1 \tag{5.1}$$

This equation is valid for any sign in slope or zero intercept, and is of extreme importance in constructing accurate aerodynamic lookup tables for simulation.

5.5.4 Flaperons: Roll

Roll control is realized through the use of ailerons, which modify the span wise lift distribution. First, testing occurred for a fixed sideslip angle ($\beta = 0^o$) with variations in angle of attack. Next, the angle of attack was fixed ($\alpha = 6^o$), and variations in sideslip were made, as shown by the cross-plots of Fig. 5.11. The reflection method in Section 5.5.3 was used for the construction of all controls neutral ($\delta_a = 0^o$) lateral data points that varied between $\beta = -13^o - 0^o$.

Longitudinal cross plots are given in Figs. 5.11a-5.11f. Fig. 5.11a shows that for symmetric flight ($\beta = 0^o$), the lift coefficient is constant across all angles of attack. Physically, this means the lift increment/decrement by opposing ailerons cancel each other. On the other hand, Fig. 5.11b show a weak dependency to sideslip. It is interesting to note that the lift increases with negative sideslip and positive aileron deflection: a non-intuitive result considering that one would expect increased lift to

occur when the sideslip angle favors the wing with the aileron trailing edge down. The Drag coefficient increases with: angle of attack, sideslip, and aileron deflection. The pitch moment is insensitive to angle of attack, but shows a symmetric variation in pitch-to-sideslip. The variation in pitch to aileron deflection is moderately linear, and decreases with decreasing sideslip angle. This is another non-intuitive result because Fig. 5.11b shows an increase in lift with a decrease in sideslip angle, which usually comes with an associated penalty of increased pitching moment.

The lateral cross plots are given in Figs. 5.11h-5.11l. The side force decreases with increasing angle of attack and aileron deflection. Furthermore, the side force is symmetric about $\beta = 0^o$, and insensitive to aileron deflection for variations in sideslip angle. Roll moment cross-plots shows a second order relationship to aileron deflection angle, invariance to angle of attack, and symmetric bias offset about $\beta = 0^o$ in sideslip (a byproduct of wing sweep). Note that for $\beta < -2^o$ a small region exists where positive aileron deflection is insufficient to provide a negative moment. The yaw moment increases uniformly with angle of attack, but varies in sideslip. The slope of the sideslip variation is proportional to the direction of the sideslip angle, being symmetric about $\beta = 0^o$ and insensitive to aileron deflection. The dependency to direction of sideslip means no definitive statements can be made concerning aileron adverse/proverse yaw coupling.

Overall, the ailerons provide adequate control authority over a broad range of freestream conditions while avoiding lateral and longitudinal coupling. Note that testing is typically made with the horizontal tail removed. This is because as the aircraft rolls in response to aileron deflection, the inboard aileron trailing vortex

is swept away from the tail via the helix angle [21]. For the tests conducted, the tail section was not removed because the short distance between the wing and tail stations suggest that the helix angle will not be sufficient to sweep the trailing vortex from the tail in unconstrained flight.

5.5.5 Ruddervators: Yaw

Control power cross-plots are given in Fig. 5.12. The Longitudinal coefficients in Figs. 5.12a-5.12i show an increasing offset with angle of attack, and symmetric variation with sideslip about the $\beta = 0^o$ contour. Drag and pitch moment both increase symmetrically with the sign of rudder deflection. The moment plots shows a mild sensitivity to sideslip, with greatest variation when $\delta_r = \pm 45^o$ and changing by as much as $\Delta C_{m_w} = 0.1$ from the $\beta = 0^o$ contour. This perturbation is approximately equivalent to an elevator deflection of $\delta_e = \pm 5^o$, as seen in Fig. 5.9g.

The lateral side force coefficient in Figs. 5.12a-5.12l show no dependency on angle of attack, but have a bias offset with increasing sideslip angle. The roll moment plots show a bias offset to sideslip angle and moderately sensitivity to angle of attack. Note that for negative rudder deflections (which produce positive yawing moments), the roll coefficient C_l takes on negative values. This behavior is typical of V-tail aircraft, known as "adverse roll-yaw coupling" [24].

The yaw plots show no dependency to sideslip or angle of attack. A linear approximation is justifiable for rudder deflections of $\delta_r = \pm 30^o$, with control effectiveness leveling off at higher deflection angles.

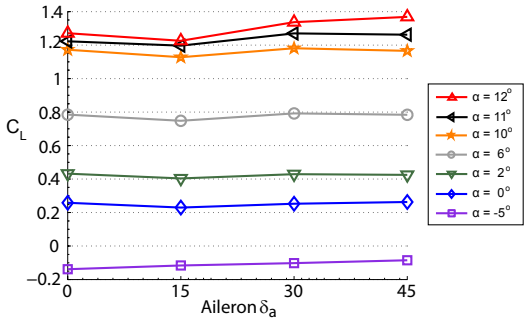

(a) $\beta = 0^o$

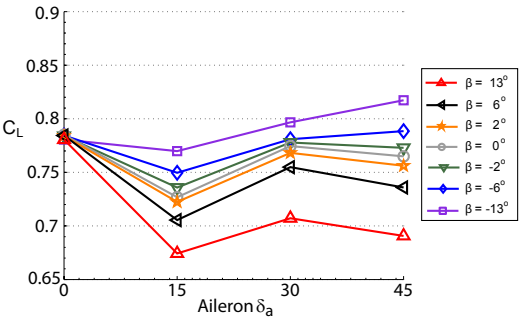

(b) $\alpha = 6^o$

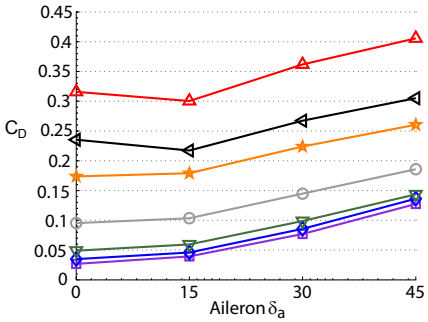

(c) $\beta = 0^o$

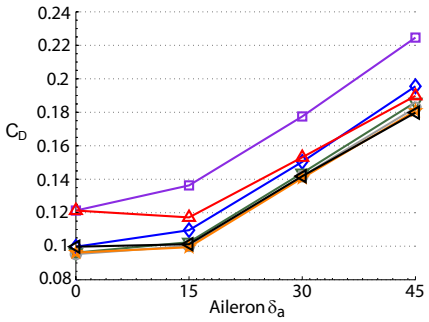

(d) $\alpha = 6^o$

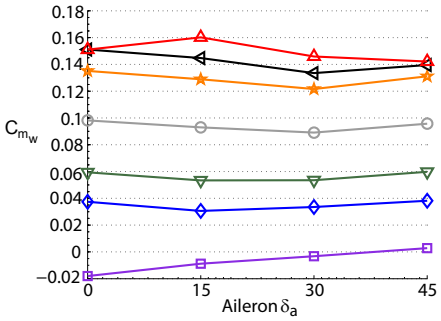

(e) $\beta = 0^o$

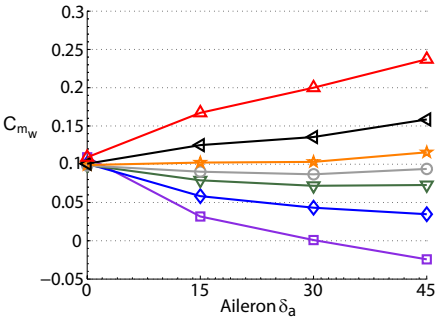

(f) $\alpha = 6^o$

Figure 5.11: Aileron Control Power (Longitudinal): V = 110 mph

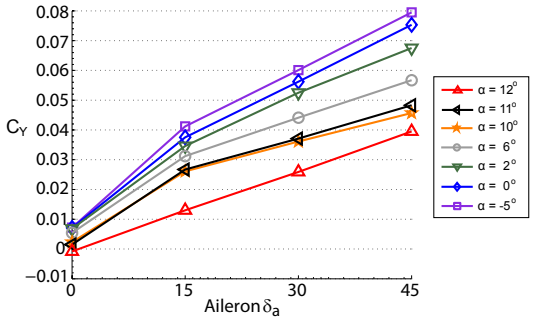

(g) $\beta = 0^o$

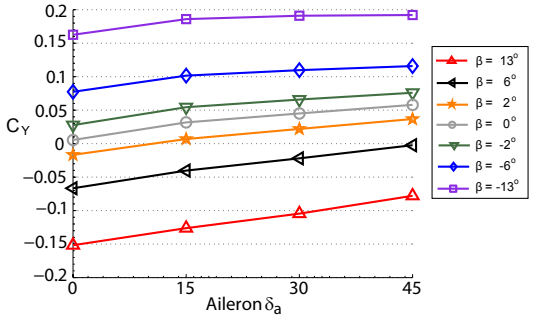

(h) $\alpha = 6^o$

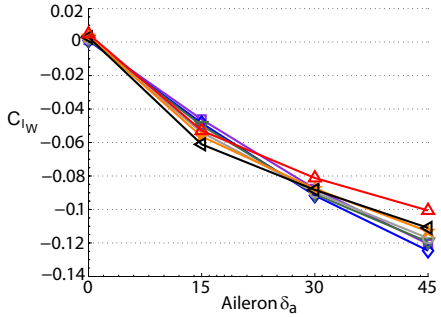

(i) $\beta = 0^o$

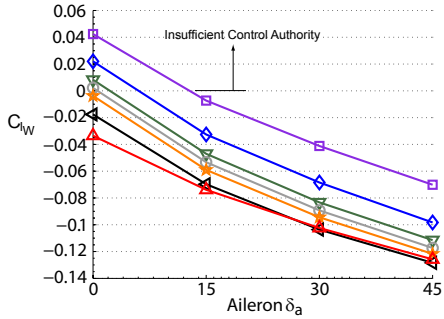

(j) $\alpha = 6^o$

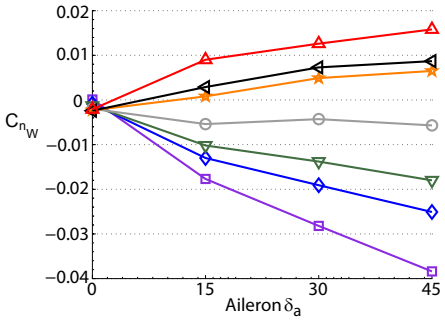

(k) $\beta = 0^o$

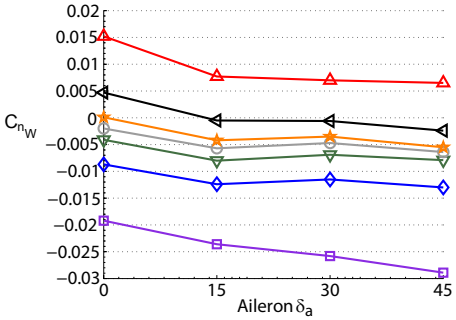

(l) $\alpha = 6^o$

Figure 5.11: Aileron Control Power (Lateral): V = 110 mph

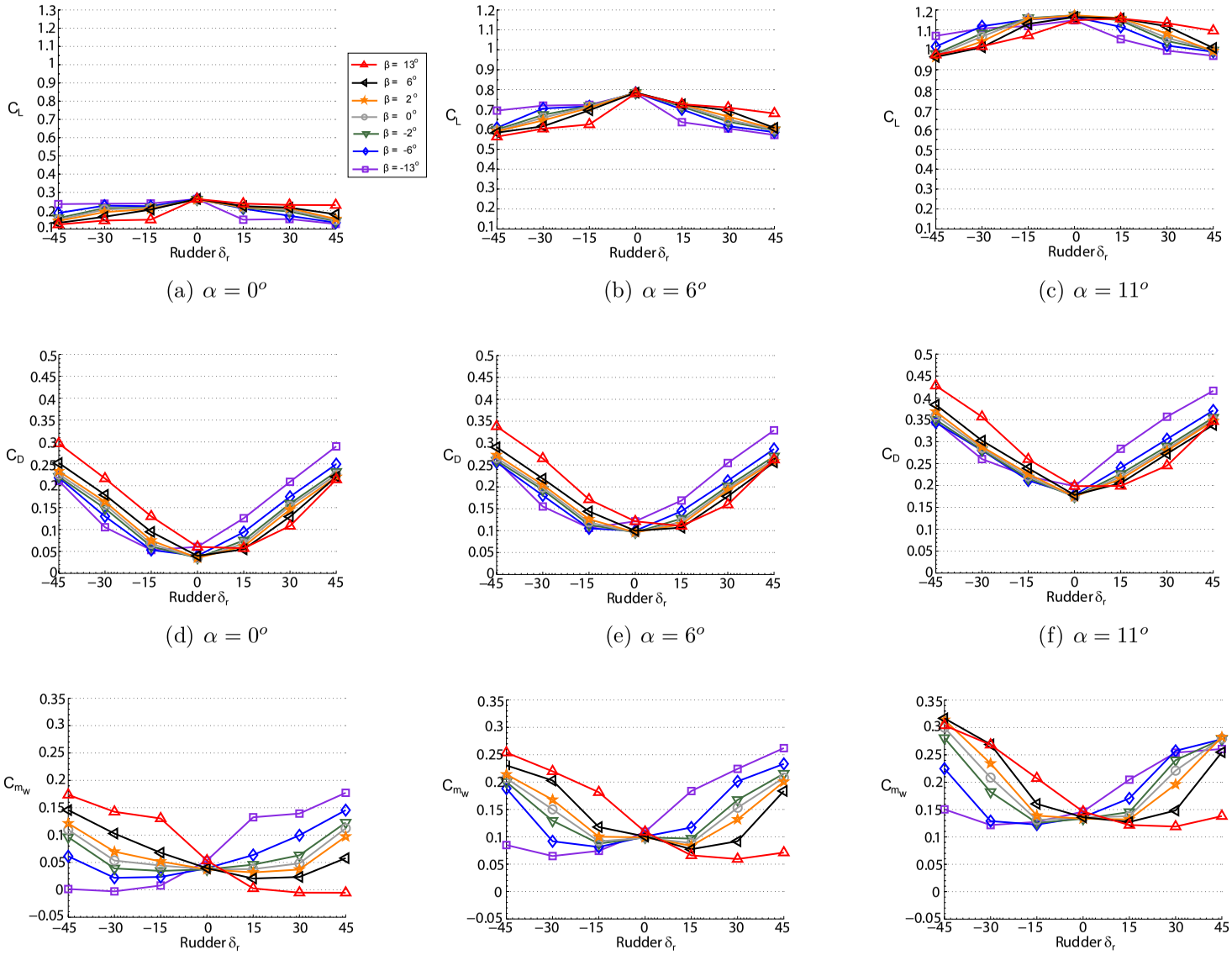

(a) $\alpha = 0^o$ (b) $\alpha = 6^o$ (c) $\alpha = 11^o$

(d) $\alpha = 0^o$ (e) $\alpha = 6^o$ (f) $\alpha = 11^o$

(g) $\alpha = 0^o$ (h) $\alpha = 6^o$ (i) $\alpha = 11^o$

Figure 5.12: Rudder Control Power (Longitudinal): V = 110 mph

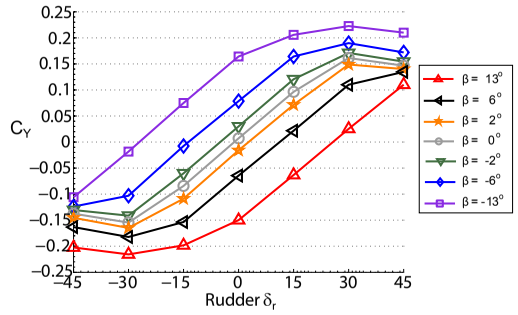

(j) $\alpha = 0^o$

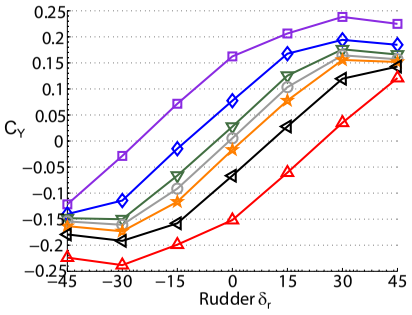

(k) $\alpha = 6^o$

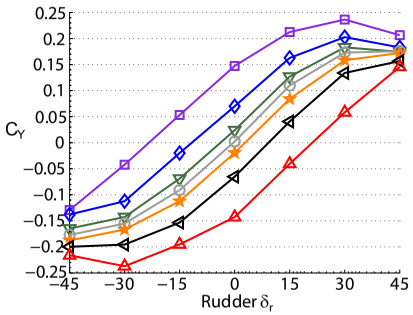

(l) $\alpha = 11^o$

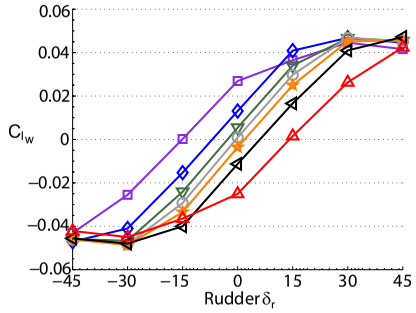

(m) $\alpha = 0^o$

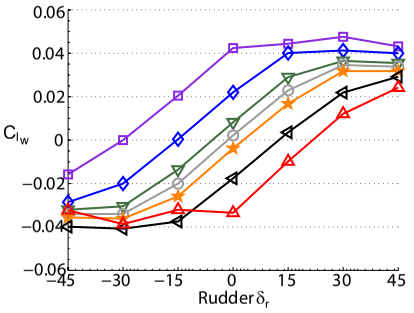

(n) $\alpha = 6^o$

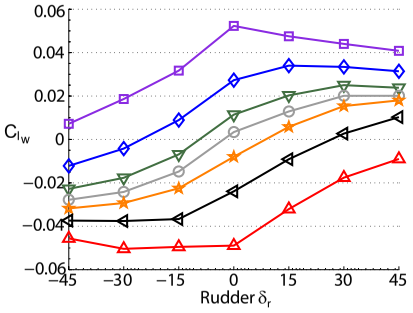

(o) $\alpha = 11^o$

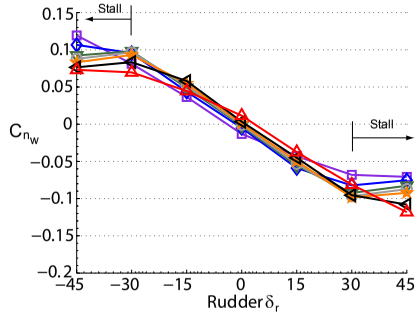

(p) $\alpha = 0^o$

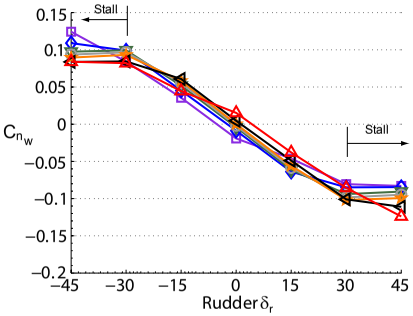

(q) $\alpha = 6^o$

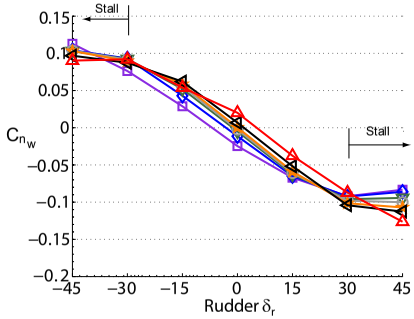

(r) $\alpha = 11^o$

Figure 5.12: Rudder Control Power (Lateral): V = 110 mph

Chapter 6

Experimental Setup: Dynamic Testing

6.1 Design of Experiment

Dynamic tests were performed to determine the model structure[1] and parameter estimates[2] resulting from body axis rotation rates. In preparation for testing, the model was attached to the wind tunnel support using a bearing box housing that was configured to allow for single degree of freedom rotation in roll, pitch or yaw. Due to limitations in time, the roll axis was not tested. A Microstrain 3DM-GX1[3] inertial measurement unit (IMU) was placed inside the nose of the model (Fig. 6.1) to measure the Euler angles (ψ,θ,ϕ) and body rates (p,q,r). The 100Hz sampling rate, well above the natural dynamics of the model, precluded concerns of aliasing. Since no major aeroelastic effects were observed during testing, the model was treated as a rigid body and angular measurements were used directly. Because the model was fully constrained in translational, measured accelerations were due to (i) IMU position offset from the c.g. during rotation and (ii) aerodynamic buffeting (noise). Consequently, it was not possible to calculate the dynamic force parameters with rate dependencies. Finally, the model mass, inertia, and c.g. properties were

[1]Model structure determination is to obtain a mathematical form of the given data that is parsimonious and has good predictive capability.

[2]Parameter estimation is the process of calculating the coefficients of a given model structure by minimizing the square of the error between model and measurement values.

[3]The sensor specifications are given in Table C-2 of Appendix C.

estimated using the Solid Works model assembly and part definitions. Validation was performed by comparing the estimated and measured model mass, which agreed within 5%. The error was attributed to paint, glue and sanding not accounted for in the computer model.

Figure 6.1: Microstrain 3DM-GX1 Inertial Measurement Unit

6.2 Origins of Aerodynamic Damping

The influence of the yaw rate r on the aircraft dynamics is shown in Fig. 6.2. Positive rotation of the aircraft about the yaw axis produces a linear velocity distribution along the span of the wing. Asymmetric lift between the port and starboard wing induces a positive roll coupling in the form of C_{l_r}. Note that the test setup only allowed for rotation along one axis at a time; therefore, this cross term could not be determined via system identification. Finally, a restoring yaw moment is produced by the change in sideslip angle α at ruddervators due to the yaw rate. Similarly, the differential drag on each wing also produces a restoring moment.

Rotation rates about the longitudinal axis of the aircraft create a linear velocity distribution across the wing, shown in Fig. 6.3. The distribution causes a roll

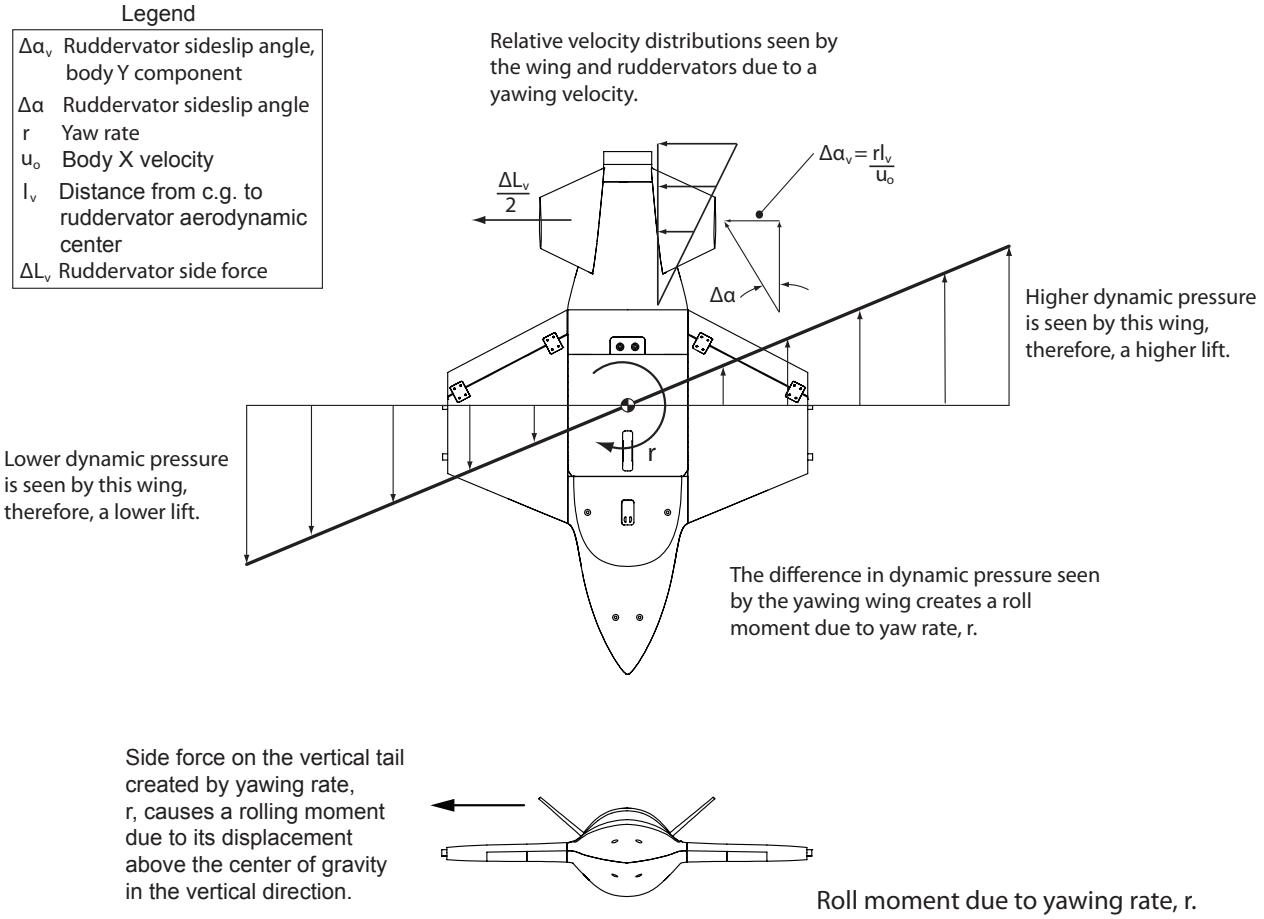

Figure 6.2: Influence of the yawing rate on the wing and vertical tail.

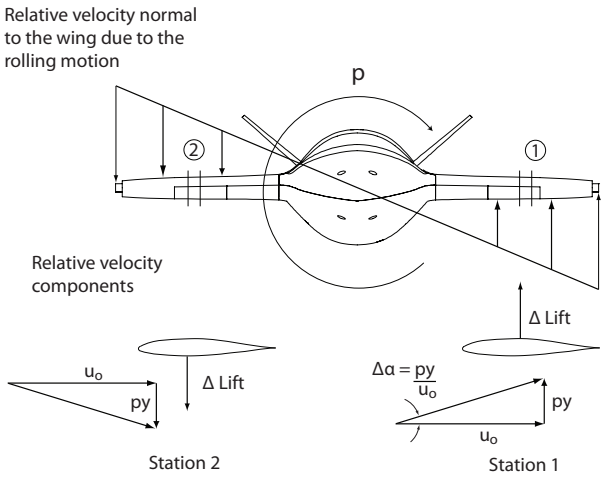

Figure 6.3: Wing planform undergoing a rolling motion.

moment, C_{l_p}, due to the increase and decrease in angle of attack at the port and starboard wing, respectively. Typically, the roll damping is due to contributions of the wing; however, the low aspect ratio design means the fuselage and ruddervators can potentially contribute as much damping as the wing [28]. Unfortunately, testing in the roll axis was not performed due to time constraints; consequently lateral modeling accuracy may suffer depending on the sensitivity to C_{l_p}.

Rotation about the lateral axis produces the stability derivatives C_{z_q} and C_{m_q}, which arise from the velocity profile (and hence change in angle of attack) at the ruddervators due to pitch rate q shown in Fig. 6.4.

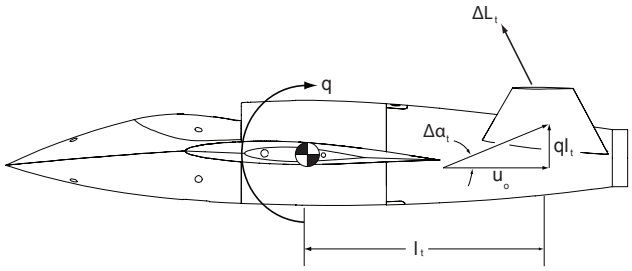

Figure 6.4: Mechanism for aerodynamic force due to pitch rate.

Finally, it is worth noting that stability derivatives $C_{z_{\dot{\alpha}}}$ and $C_{m_{\dot{\alpha}}}$ are a consequence of lag in the downwash of the wing onto the ruddervators [28], but could not be measured directly due to collinearity: the test setup allowed for the measurement of $C_{m_{\dot{\alpha}}} + C_{m_q}$, and is detailed in Section 7.2.

A detailed derivation of the aforementioned dynamic coefficients can be found in Refs. [25, 28]. Table 6.1 summarizes the dynamic force and moment parameters estimated during testing:

Table 6.1: Aerodynamic Damping Parameters

C_{z_q}	C_{m_q}	$C_{z_{\dot{\alpha}}}$	$C_{m_{\dot{\alpha}}}$	C_{y_p}	C_{n_p}	C_{l_p}	C_{y_r}	C_{n_r}	C_{l_r}
✗	✓	✗	✓	✗	✗	✗	✗	✓	✗

6.3 System Identification

6.3.1 Background Theory

A brief overview of the important equations and concepts of linear estimation theory are given in this section, and based on Ref [26]. Throughout this paper, all postulated model structures are linear. As a result, they can be expressed as:

$$\boldsymbol{y} = \boldsymbol{X}\boldsymbol{\theta} \tag{6.1}$$

where $\boldsymbol{X}$ is a matrix of vectors of ones and regressors (measured values) and $\boldsymbol{\theta}$ is a vector of parameters to be estimated. The regression equation is defined as:

$$\boldsymbol{z} = \boldsymbol{X}\boldsymbol{\theta} + \boldsymbol{\nu} \tag{6.2}$$

where $\boldsymbol{z}$ is the measured output and $\boldsymbol{\nu}$ is a vector of measurement noise. The noise is assumed to be zero mean, uncorrelated, and constant variance:

$$E(\boldsymbol{\nu}) = \boldsymbol{0} \qquad E(\boldsymbol{\nu}\boldsymbol{\nu}^{\boldsymbol{T}}) = \sigma^2\boldsymbol{I} \tag{6.3}$$

Under these assumptions, the linear estimation problem can be solved analytically by minimizing the sum of the squared errors in the cost function:

$$J(\boldsymbol{\theta}) = \frac{1}{2}(\boldsymbol{z} - \boldsymbol{X}\boldsymbol{\theta})^T(\boldsymbol{z} - \boldsymbol{X}\boldsymbol{\theta}) \tag{6.4}$$

The solution to this optimization problem is:

$$\hat{\boldsymbol{\theta}} = (\boldsymbol{X}^T\boldsymbol{X})^{-1}\boldsymbol{X}^T\boldsymbol{z} \tag{6.5}$$

where $\hat{\boldsymbol{\theta}}$ is the best (unbiased) parameter estimate that minimizes Eq. (6.18). Next, the covariance matrix of the parameters is:

$$Cov(\hat{\boldsymbol{\theta}}) \equiv E[(\hat{\boldsymbol{\theta}} - \boldsymbol{\theta})(\hat{\boldsymbol{\theta}} - \boldsymbol{\theta})^T] = (\boldsymbol{X}^T\boldsymbol{X})^{-1}\boldsymbol{X}^T E(\boldsymbol{\nu}\boldsymbol{\nu}^T)\boldsymbol{X}(\boldsymbol{X}^T\boldsymbol{X})^{-1} \tag{6.6}$$

where the diagonal terms are the variance of the parameter estimates (equal to 1-σ standard deviation), and the off diagonal terms are the covariances between parameters, which take on large nonzero values when the parameters when collinear.

Finally, the coefficient of determination is defined as:

$$R^2 = \frac{\hat{\boldsymbol{\theta}}^T\boldsymbol{X}^T\boldsymbol{z} - N\bar{z}^2}{\boldsymbol{z}^T\boldsymbol{z} - N\bar{z}^2} \tag{6.7}$$

where N is the number of data points in the time series, and $\bar{z}$ is the average value for the measured output. The R^2 value is a measure of how well the model fits the data and varies between 0 and 1, where 1 is a perfect fit.

6.3.2 SIDPAC

This subsection describes mathematical underpinnings behind the collection of programs known as System IDentification Programs for AirCraft (SIDPAC) developed by Dr. Eugene Morelli of NASA Langley and used in this paper.

6.3.2.1 deriv.m

During dynamic wind tunnel testing, the onboard IMU measured the angular body rates (p,q,r); however, no such sensor exists for angular accelerations. Consequently, these values need to be obtained via numerical differentiation of the rate terms. While finite differencing methods can be used, they inherently magnify the sensor noise inversely to the time step. Instead, local smoothing is performed in the time domain by fitting a local second-order polynomial of the form:

$$y = a_0 + a_1 t + \frac{1}{2} a_2 t^2 \tag{6.8}$$

where the derivative is given by:

$$\dot{y} = a_1 + a_2 t \tag{6.9}$$

Because Eq. (6.9) evaluated at the current point, $t = 0$,the local derivative is equal to a_1. The solution for a_1 can be found via the normal equations as:

$$a_1 = \frac{\sum_{k=i-2}^{i+2} kz(k)}{10\Delta t} \tag{6.10}$$

where i is the index of the ith measured data point at time $i\Delta t$, Δt is the time step, and $z(k)$ is the measured datapoint.

6.3.2.2 smoo.m

Implicit in the formulation of linear regression is that the regressors $\boldsymbol{X}$ are measured without noise. This assumption is violated for the noisy data collected during experimental runs, leading to the parameter estimates being biased and inefficient[26]. Therefore, an optimal global Fourier smoother was applied to reduce measurement noise for all signals. This methodology has been found to increase estimation accuracy [27].

The routine works by first zeroing the endpoints of the signals. Next, the data is reflected about the origin to remove slope discontinuities at the endpoints. The periodic data is then expanded using a Fourier sine series, as the reflection process makes the resulting signal an odd function. Since the endpoint discontinuities were removed through the zero/reflection process, it can be shown that the deterministic components of the Fourier magnitude plot decreases as k^{-3}, where k is the frequency index, to a constant value. Therefore, all frequencies where the Fourier magnitudes are constant are due to measurement noise. This information is then used to construct an optimal Wiener filter:

$$\Phi(k) = \frac{\tilde{y}^2(k)}{\tilde{y}^2(k) + \tilde{\nu}^2(k)} \tag{6.11}$$

where $\tilde{y}^2(k)$ is the Fourier magnitudes that decay as k^{-3} and $\tilde{\nu}^2(k)$ are the Fourier

coefficients after leveling-off has occurred. The data is then transformed back into the time domain, and the endpoints are readjusted to their original values. The advantage of this methodology is that the smoother avoids introducing phase shifts in the data, which is critical because the system identification techniques are based on mappings between the regressors and output in the time domain.

6.3.2.3 mof.m

The function mof.m determines the best mathematical model for a measured output. First, the user inputs a collection of measured signals and specifies the maximum order each individual signal and maximum order for any product of signals. Next, a pool of candidate regressors are generated subject to the user constraints. These regressors are then orthogonalized using a Gram-Schmidt process:

$$\boldsymbol{P} = \boldsymbol{X}\boldsymbol{G}^{-1} \tag{6.12}$$

where $\boldsymbol{G}$ is an upper triangular transformation matrix of ones along the diagonal and parameter projections on the super-diagonal. Because the orthogonalization processes depends on the order in which the regressors are assembled in the P matrix, the most important variables are placed in the beginning columns of the matrix to ensure a small model structure. The advantage of using orthogonalized regressors is that each one contributes uniquely to the model fit. A solution space is then generated for every possible set of orthogonal regressors, without regard for

order, and ranked according to its predicted square error:

$$\text{PSE} \equiv \frac{1}{N}(\boldsymbol{z} - \hat{\boldsymbol{X}}\hat{\boldsymbol{\theta}})^T(\boldsymbol{z} - \hat{\boldsymbol{X}}\hat{\boldsymbol{\theta}}) + \sigma_{max}^2\frac{p}{N} \tag{6.13}$$

where σ_{max} is an estimate of the maximum variance, and p is the number of model terms. The lowest PSE solution is selected as the best model, and the model parameters are obtained by performing the inverse transformation of Eq. (6.12) on the orthogonal regressors. Equation (6.13) can be rewritten in terms of the mean squared fit error (MSFE):

$$PSE = MSFE + \sigma_{max}^2\frac{p}{N} \tag{6.14}$$

where:

$$MSFE = \frac{1}{N}(z - \hat{y})^T(z - \hat{y}) = \frac{1}{N}(\nu^T\nu) \tag{6.15}$$

Expressing the PSE using Eqs. (6.14)-(6.14), it can be seen that the MSFE is the least squares cost function divided by the number of data points in the time series. Since the regressors were orthogonalized using Eq. (6.12), the MSFE decreases monotonically with each new term added to the model. On the other hand, the over fit penalty term $\sigma_{max}^2\frac{p}{N}$ increases monotonically with the number of model terms. Therefore, the PSE will always have a single global minimum value when determining the best model structure.

Finally, the model independent estimate of the maximum variance can be

estimated as:

$$\sigma^2_{max} = \frac{1}{N}\sum_{i=1}^{N}[z(i) - \bar{z}]^2 \tag{6.16}$$

where $\bar{z}$ is the mean of the measured response.

6.3.2.4 *r_colores.m*

Recall that the methodology introduced previously was for ordinary least-squares, where it was assumed the measurement errors were zero mean, uncorrelated and equal variance. In practice, the assumption of uncorrelated noise is invalid. Consequently, the noise can be represented as:

$$E(\nu) = 0 \qquad Cov(\nu) = E(\nu\nu^T) = V \tag{6.17}$$

where V is a nonsingular and positive definite noise covariance matrix. This change propagates to the cost function:

$$J(\boldsymbol{\theta}) = \frac{1}{2}(\boldsymbol{z} - \boldsymbol{X\theta})^T V^{-1}(\boldsymbol{z} - \boldsymbol{X\theta}) \tag{6.18}$$

and parameter estimates:

$$\hat{\boldsymbol{\theta}} = (\boldsymbol{X}^T\boldsymbol{X})^{-1}\boldsymbol{X}^T V^{-1}\boldsymbol{z} \tag{6.19}$$

which is now *asymptotically* unbiased. This solution is a weighted least squares problem, with the weighting matrix defined as $W = V^{-1}$. However, because all the

measured time histories are coming from a single IMU under the same conditions at the same time, there is no justification for introducing unequal weightings to model heterogeneous variances; therefore, the ordinary least squares solution of Eq. (6.19) is used.

On the other hand, the residuals can be significantly correlated because the data is collected sequentially in time from a moving aircraft. This affects the estimated covariance matrix, and corrections are made by way of introducing as estimate of autocorrelation from the measured time histories in Eq. (6.6):

$$Cov(\hat{\boldsymbol{\theta}}) = (\boldsymbol{X}^T\boldsymbol{X})^{-1}\left[\sum_{i=1}^{N}\boldsymbol{x}(i)\sum_{j=1}^{N}\hat{\mathcal{R}}_{\nu\nu}(i-j)\boldsymbol{x}^T(j)\right](\boldsymbol{X}^T\boldsymbol{X})^{-1} \tag{6.20}$$

where $\hat{\mathcal{R}}_{\nu\nu}(i-j)$ is the autocorrelation matrix for the residuals (assumed to be a zero mean, weakly stationary process). This error bounds correction is necessary because without it, the errors will be underestimated.

6.3.3 Data Filtering

Prior to analysis, the measured time histories of the signals were processed and filtered. First, the non-constant Euler angle and body rotation rates were resampled to a constant time step of $dt = 0.0005$ using the built in MATLAB spline function. This time step value was chosen to avoid introducing time shifts in the signal; however, it inevitably added high frequency oscillations that result from curve fitting the data through tightly spaced time steps. Next, the resulting signal was down-sampled to every 5th data point, or dt =0.0025, to avoid excessively large vector

sizes. This signal was then smoothed using smoo.m in Subsection 6.3.2.2. The rate terms were then differentiated using deriv.m in Subsection 6.3.2.1 to obtain estimates of the body angular accelerations. The smoothed sensor data for the Euler angles and body rates were cross checked for consistency as follows. First, the deriv.m was applied to the smoothed Euler angle sensor output, and plotted against smoothed body rates. Conversely, simple Euler integration was applied to the smoothed body rates and plotted against the smoothed Euler angles. In both cases the agreement was excellent. With this consistency check completed, the data was then windowed for system identification over an interval that started at the point of release and ended when the model returned to equilibrium (see Fig. 7.4 in Subsection 7.1.2).

Chapter 7

Experimental Results: Dynamic Testing

7.1 Yaw Perturbation Tests

7.1.1 Test Procedure

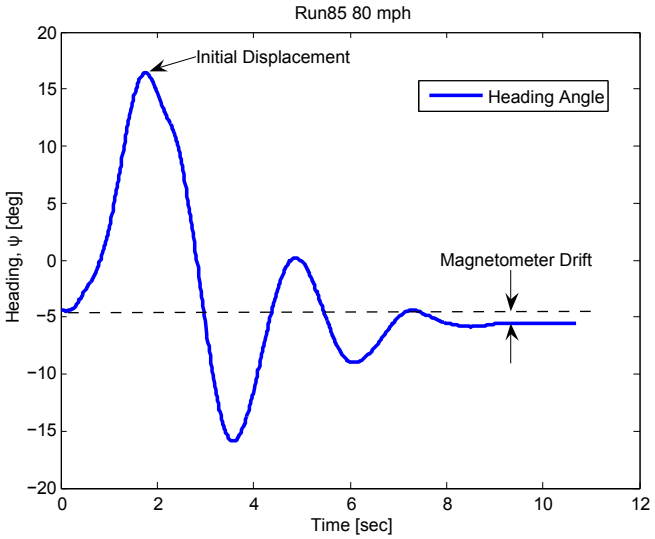

Figure 7.1: Controls neutral heading offset, $\psi = -5.6^o$

Yaw tests were conducted by configuring the bearing box to allow for rotation parallel to the body z-axis of the model. Rectangular string was fed though a hole on the port side of the wind tunnel and tied around the empennage. At the start of each run, the string was drawn into the control room of the wind tunnel. This pivoted the nose of the aircraft starboard, inducing an initial condition of a positive heading displacement. The model was briefly held at this position and then

released. Upon release the model oscillated about the bearing axis and returned to a stable equilibrium position, as shown in Fig. 7.1. The controls-neutral runs typically returned to an equilibrium heading angle of $\psi \cong -6^o$, despite being a controls neutral configuration. According to Barlow[21], this behavior is attributed to asymmetric flow in the tunnel, model asymmetry, or hysteresis due to small separation areas. The tunnel operators hypothesized that the heading offset was due to the asymmetric increase in drag on the port side of the aircraft caused by to the rectangular string. At times, the string would transition from random whipping motions to distinct modal shapes, supporting the hypothesis. In addition, slight drift was noticed in the yaw angle between the start and end of each run. This is because the IMU relies on a magnetometer for absolute yaw angle and that the wind tunnel had lots of iron close by. This was not a problem for the high frequency data collected because the mean about the oscillations remained fairly constant. Tests were performed for tunnel speeds ranging from 80-120 mph, in progressive increments of 10 mph (see Appendix B for the complete test matrix). In addition, the model configurations tested were controls-neutral, and $\delta_r = 15^o$ rudder deflection (where positive rudder is defined as left trailing edge movement as viewed from behind).

7.1.2 Model Structure Determination

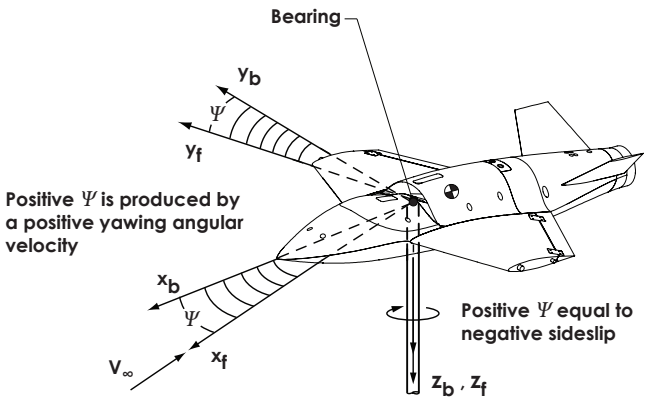

Figure 7.2: Wind-tunnel model constrained to pure yawing motion.

The test setup, with wind tunnel and aircraft body frames subscripted f & b, respectively, is shown in Fig. 7.3. The equation of motion can be written as:

$$\sum \text{Yawing moments} = I_{zz}\ddot{\psi} \tag{7.1}$$

where the inertial value I_{zz} is calculated about the *pivot point* of the bearings and $\ddot{\psi}$ is obtained by smoothed numerical differentiation of the measured body rate r. The constraint of horizontally planar rotation resulted in the following angular relationships:

$$\psi = -\beta \qquad \dot{\psi} = -\dot{\beta} = r \tag{7.2}$$

where β is the sideslip angle, r is the body yaw rate, and ψ is the heading angle. From Eq. (7.2) it is apparent that $\dot{\beta}$ and r are collinear, precluding the possibility of attributing yaw moments from either state independently. Fortunately, the contribution from $\dot{\beta}$ is usually small; therefore, it was assumed that all yaw rate

parameters were directly attributable to r.

The SIDPAC function $mof.m$, detailed in Subsection 6.3.2.3, was used to determine the model structure of the yaw moments on left hand side of Eq. (7.1). $z = I_{zz}\ddot{\psi}$ was used as the measured output and $\theta = [\beta\ r]$ was used as the pool of candidate regressors. Each regressor had its constant value removed to prevent correlation with the bias term and allow for a true multivariate Taylor series expansion [26]. The following linear model structure was obtained:

$$C_n = C_{n_0} + C_{n_\beta}\Delta\beta + C_{n_{\hat{r}}}\Delta\hat{r} \tag{7.3}$$

where:

$$C_{n_\beta} = \left.\frac{\partial C_n}{\partial \beta}\right|_0 \quad C_{n_{\hat{r}}} = \left.\frac{\partial C_n}{\partial \hat{r}}\right|_0 \quad \hat{r} = \frac{rb}{2V_0} \tag{7.4}$$

A randomly chosen controls neutral run is presented in Fig. 7.3. The residual, shown in the lower subplot, is zero mean with little deterministic content. The coefficient of determination, $R^2 = 98.78$, is indicative of an excellent model.

Testing was then repeated for a $\delta_r = 15^0$ control deflection, shown in Fig. 7.4. The effect of the rudder input was a significant increase in mean and peak sideslip amplitude, causing the model to oscillate around the transition point of nonlinear flow. In order to maintain a simple model structure, a linear spline[1] $S(\beta)$ was included in the pool of candidate regressors: $\boldsymbol{X} = [\beta\ S(\beta)\ r]$.

[1] A spline knot at $\beta = 15^o$ was found to be the statistically best estimate of the transition angle for the dynamic flow field. This value is close to the $\beta_0 = 18^o$ trim value and indicates the direction of the perturbation from trim resulted in the model experiencing linear or nonlinear flow, as indicated by the red shaded region of Fig. 7.4.

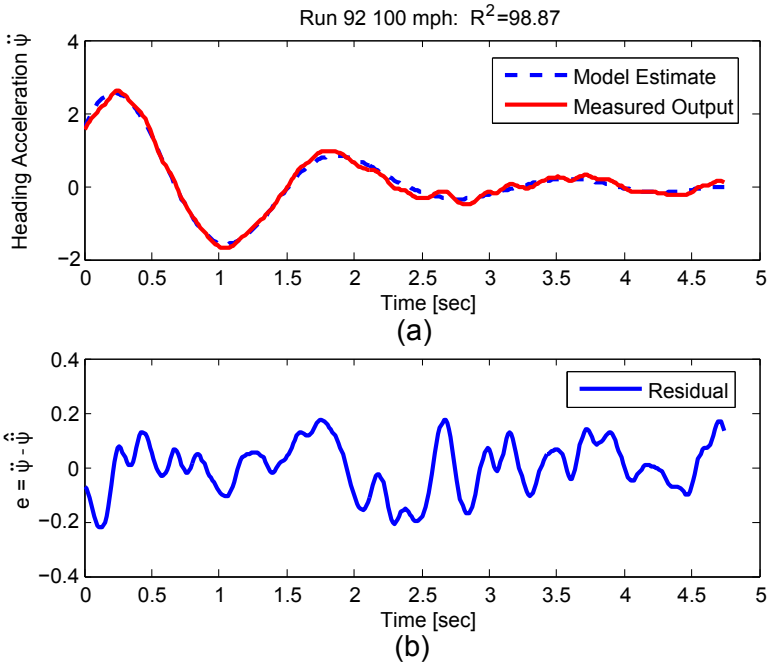

Figure 7.3: Controls neutral yaw perturbation.

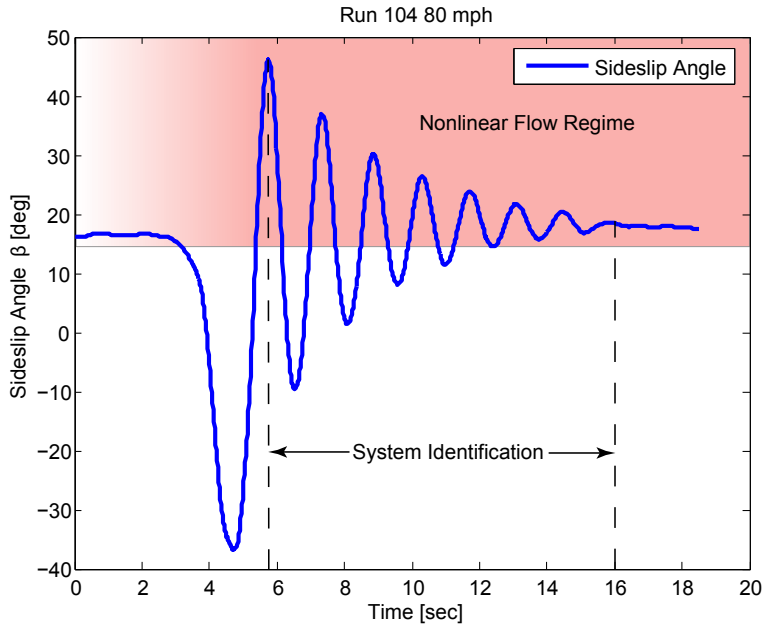

Figure 7.4: $\delta_r = 15^o$ yaw perturbation.

The model structure was determined to be:

$$C_n = C_{n_0} + C_{n_\beta}\Delta\beta + C_{n_{S(\beta)}}S(\beta) + C_{n_{\hat{r}}}\Delta\hat{r} \tag{7.5}$$

where the linear coefficients $[C_{n_\beta}\ C_{n_{\hat{r}}}]$ were calculated using Eq. (7.4) and $C_{n_{S(\beta)}} = \frac{\partial C_n}{\partial \beta}|_0$ for $\beta > 15^o$. Note at trim the net moment on the model is zero ($C_{n_o} = 0$); therefore, the bias term must be equal and opposite to the bearing dynamic frictional force.

7.1.3 Parameter Estimation

The model parameter estimates of Eqs. (7.3),(7.5) were determined using the SIDPAC function *r_colores.m*, detailed in Subsection 6.3.2.4, to correct for colored residuals in the Cramer-Rao bounds. Figure 7.5 shows damping parameter estimates plotted against tunnel speed. In order to improve estimation accuracy, each data point in the figure represents the average of four repeated runs. The mean and scatter for the repeated runs were found to be nearly identical in all cases. The lack of any trends in Fig. 7.5 clearly shows that the damping terms are invariant to the range of tunnel speeds tested. Mean values of the damping parameters are closer to zero for increasing rudder deflection, which follows the observed increase in oscillations of Fig. 7.4 as compared to Fig. 7.1. Furthermore, it must be emphasized that the damping parameters are slightly over-predicted due to unquantified bearing friction, as the setup of the experiment precluded quantification of this error.

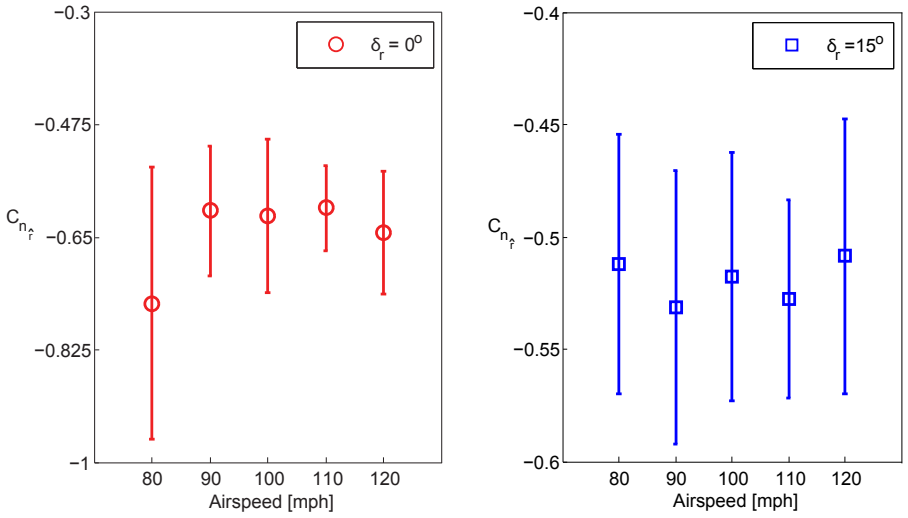

(a) $\delta_r = 0^o$ (b) $\delta_r = 15^o$

Figure 7.5: Damping parameter estimates vs. tunnel speed w/95% CI.

7.1.4 Comparison of Static and Dynamic Data

Parameter estimates of the yaw stiffness term-C_{n_β} were calculated using static and dynamic data, with comparisons serving to (i) act as validation, and (ii) quantify changes in the flow field due to the dynamic behavior arising from body rotation rates. This parameter was chosen as a metric because it uses a wide range of sideslip angles for its determination and has profound implications on stability. Pitch neutral static data (with variations in sideslip angle) was used in the comparative analysis to match the attitude constraint in the dynamic runs. In addition, corrections[2] were made to account for origin offsets.

The yaw moment graphs of the static data are shown in Fig. 7.6. In both rudder deflection cases ($\delta_r = 0^o$,$\delta_r = 15^o$), the model structure of the static data

[2]The static runs were calculated about an origin at the design cg, while dynamic runs were calculated about an origin at the bearings. The 'design cg' is the location of the production aircraft center of gravity, which differed from the *physical* cg of the model.

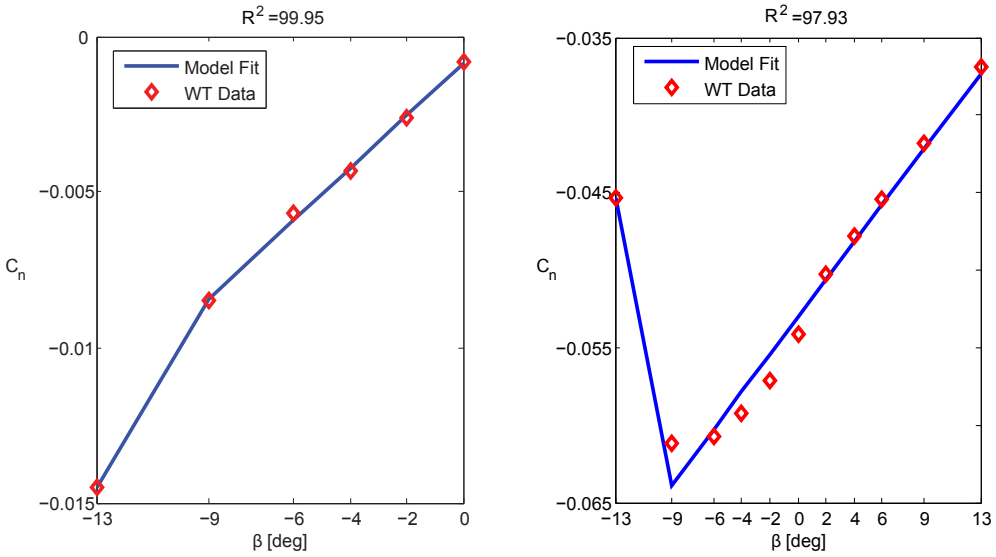

(a) $\delta_r = 0^o$ (b) $\delta_r = 15^o$

Figure 7.6: Static yaw moment curves at for $\theta = 0^o$, $V = 110$ mph.

was determined to be linear between $-9^o \leq \beta \geq 13^o$ with a linear spine at $\beta \leq -9^o$:

$$C_n = C_{n_o} + C_{n_\beta}\Delta\beta + C_{n_{S(\beta)}}S(\beta) \tag{7.6}$$

Note that the model structure of Eq. (7.6) agrees fairly well with the dynamic model structure in Eqs. (7.3,7.5), which is linear for $\beta \pm 20^o$ when $\delta_r = 0^o$. The difference in the spline locations were attributed to inherent differences exists between static and dynamic flowfields. For the $\delta_r = 15^o$ dynamic runs, it is believed that the $\beta = -9^o$ spline was not found to be statistically significant because the oscillations were centered about $\beta = 18^o$; consequently, not enough time was spent in the negative sideslip region to capture the $\beta = -9^o$ spline effects, as seen in Fig. 7.4.

A comparison of the static and dynamic parameters were made by calculating

the percent error:

$$\text{percent error} = \frac{\text{measured value - accepted value}}{\text{accepted value}} \times 100 \tag{7.7}$$

In aircraft system identification, the dynamic parameter estimates are considered to be the 'accepted value'; therefore, the static parameter estimates were used as the 'measured value.' Differences in the static and dynamic tunnel speeds resulted in using a nearest neighboor approach for the measured value. For example, the percent error of the dynamic parameters at 90 mph was calculated using the 'measured values' from the 80 mph static run. Since the $\delta_r = 15^o$ static runs were only tested at one speed, the measured value was the same for all percent error calculations. This approach is not believed to affect the results significantly because the static estimate of C_{n_β} shows only a 5% change in for a 30 mph change in tunnel speed when $\delta_r = 0^o$. The percent errors are given in Table 7.1 below.

Table 7.1: Percent error of static and dynamic parameter estimates.

Tunnel Speed	C_{n_β} ($\delta_r = 0^o$)	C_{n_β} ($\delta_r = 15^o$)
80 mph	33.24%	42.65%
90 mph	35.84%	46.89%
100 mph	37.58%	43.24%
110 mph	34.99%	45.00%
120 mph	33.49%	42.87%

The percent error between the static and dynamic estimates of the stiffness terms C_{n_β} are given in Table 7.1 and show an error of 33-46%. Some of the error can be attributed to inaccuracies in the estimate of the model inertia I_{zz}, which

was used during system identification. However, the most probable explanation is that the large amplitude sideslip displacements of $\beta \pm 50^o$ (Fig. 7.4) traversed during dynamic runs resulted in the tail fins interacting with shed wingtip vortices (Fig 7.7), introducing a sidewash factor, $\partial\sigma\backslash\partial\beta$ not have encountered during static testing, where the sideslip was limited to $\beta \pm 13^o$.

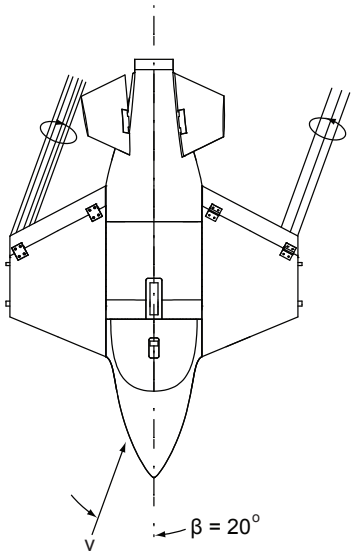

Figure 7.7: Wing-tail vortex interaction.

7.2 Pitch Perturbation Tests

7.2.1 Test Procedure

Pitch tests were conducted by configuring the bearing box to allow for rotation parallel to the body Y axis of the model. Static tests showed that the model is unstable in the pitch axis; therefore, stability augmentation was provided through the use of a linear extension spring, shown in Fig. 7.8. A servo operated track slider allowed the connection point between the spring and support strut to be raised or

lowered, thereby changing the length of the spring and hence trim attitude of the model. Two spring geometries were used, corresponding to a no wind trim condition of $\theta = -6.25^o$ and $\theta = 0.5^o$. As the tunnel was brought on-line, the model pitch attitude slowly increased until the point where the aerodynamic pitch moment was equal and opposite to the restoring torque from the spring extension, as seen by the wind on trim values in Fig. 7.9. Next, the model was given an initial pitch angle, θ_i, and allowed to freely oscillated back to trim. Nose up and nose down perturbations were induced by pressing down on the nose or tail of the aircraft with a pole that extended through a porthole in the ceiling of the wind tunnel test section. Inevitably, the introduction of the pole caused disturbances in the flow field above the model and was a source of error in the experiment: the effects were assumed negligible.

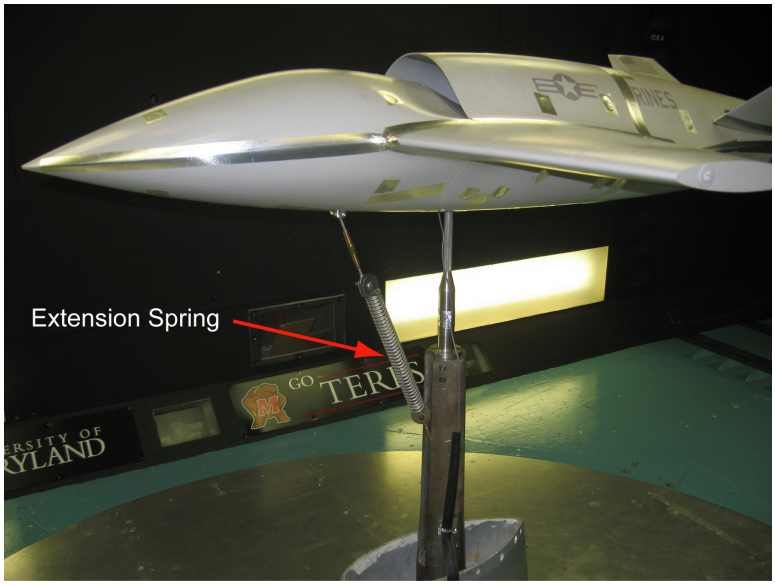

Figure 7.8: Extension spring added for stability augmentation.

Each setting in the test matrix was repeated four times, with two nose up initial conditions ($+\theta_i$), and two nose down initial conditions ($-\theta_i$), shown in Fig. 7.9b.

This method was used to obtain a broad sweep of positive and negative pitch angles, aiding in model structure and parameter estimation. Tests ranged from 70-90 mph, in progressive increments of 10 mph. Finally, no wind runs (0 mph) were performed to quantify the spring constant and frictional damping terms.

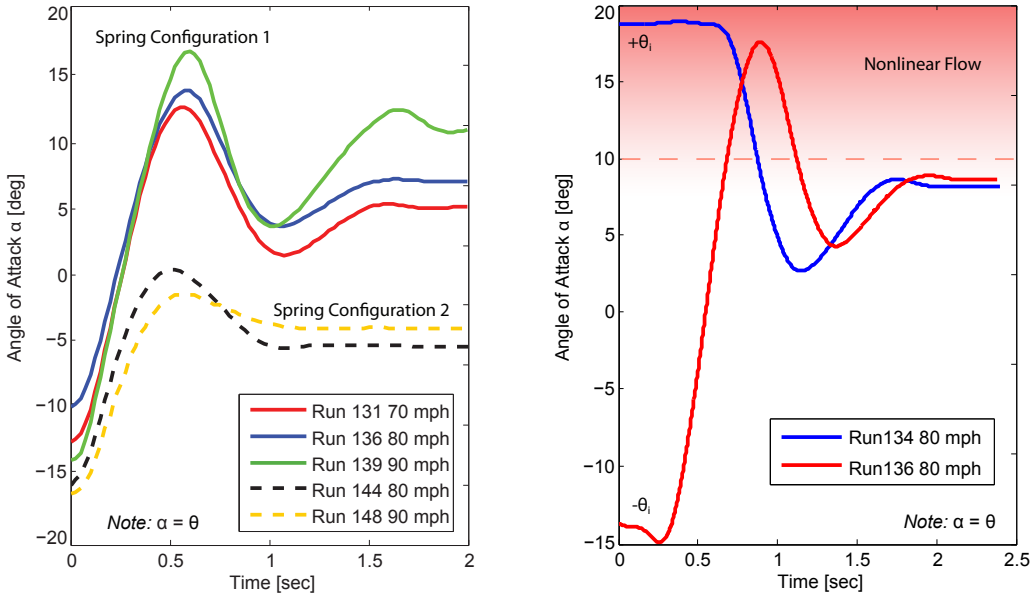

(a) Variation in wind-on trim values for various spring configuraitons.

(b) Variation of sweep in pitch angles for positive and negative initial displacement conditions.

Figure 7.9: Wind-tunnel model constrained to pure pitching motion.

7.2.2 Model Structure Determination

The test setup, with wind tunnel and aircraft body frames subscripted f & b, respectively, is shown in Fig. 7.10.

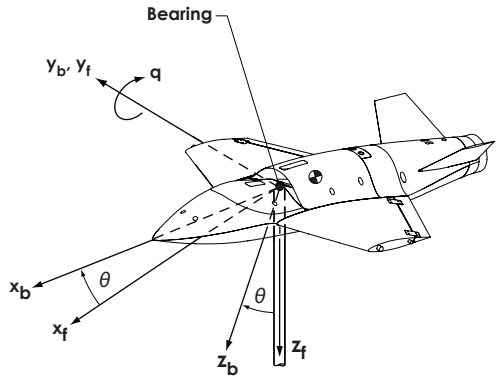

Figure 7.10: Wind-tunnel model constrained to pure pitching motion.

The angular constraints on the model resulted in the following relationships:

$$\theta = \alpha \qquad \dot{\theta} = \dot{\alpha} = q \qquad \beta = 0^o \tag{7.8}$$

where α is the angle of attack, and q is the body rate. From Eq. (7.8), it is apparent $\dot{\alpha}$ and q are collinear. This made it impossible to distinguish pitch moments from either state independently; therefore, it was assumed that all pitch rate parameters were directly attributable to q. The rotational equation of motion can be written as:

$$\sum \text{Aerodynamics Pitch Moments} + M_{cg} + \tau = I_{yy}\ddot{\theta} \tag{7.9}$$

where I_{yy} is the model inertial, τ is the restoring torque due to the spring, M_{cg} is the gravitational torque due to the cg offsets from the axis of rotation, and $\ddot{\theta}$ is obtained by smoothed numerical differentiation of the measured body rate q. Using the estimated cg offsets from the bearing axis, the model structure for M_{cg} was

derived analytically:

$$M_{cg} = WL\cos(\phi - \theta) \cong WL(1 + [\phi - \alpha_0]\Delta\alpha) \tag{7.10}$$

where W is the model weight, L is the radial distance from the pivot to cg, and ϕ is the declination angle between the pivot and cg. The rightmost expression is a linearization of the cosine term using the relationships in Eq. (7.8), the angle difference identity, and small disturbance theory.

7.2.3 Stability Analysis

As mentioned earlier, static testing showed that the model was unstable in the pitch axis. Left unresolved, perturbations way from trim will result in unstable pitch divergence, which could tear the model off the support strut and damage the wind tunnel. Static stability is achieved when the pitch stiffness-C_{m_α}, defined as the rate of change in pitch moment with respect to angle of attack, takes on negative values. This is because positive perturbations in angle of attack (nose up) generate a negative stabilizing (nose down) restoring torque [25, 28]. In order to quantify a baseline estimate on the level of instability, system identification (see Section 6.3) was performed on the static pitch moment data of Fig. 7.11, yeilding the linear model:

$$C_m = C_{m_0} + C_{m_\alpha}\Delta\alpha + C_{m_{S(\alpha^2)}}S(\alpha^2) \tag{7.11}$$

where $S(\alpha^2)$ is defined for $\alpha \geq 10^o$ and the nondimensional parameters are defined as:

$$C_{m_\alpha} = \left.\frac{\partial C_m}{\partial \alpha}\right|_0 \qquad C_{m_{S(\alpha^2)}} = \left.\frac{\partial C_m}{\partial \alpha^2}\right|_0 \tag{7.12}$$

Next, the restoring torque of the spring was modeled[3] as:

$$\tau = \tau_0 + \kappa_{eq}\Delta\alpha \tag{7.13}$$

where τ is the net torque due to the spring, τ_0 is the torque at trim, and κ_{eq} is the equivalent torsional spring constant from the linear extension spring.

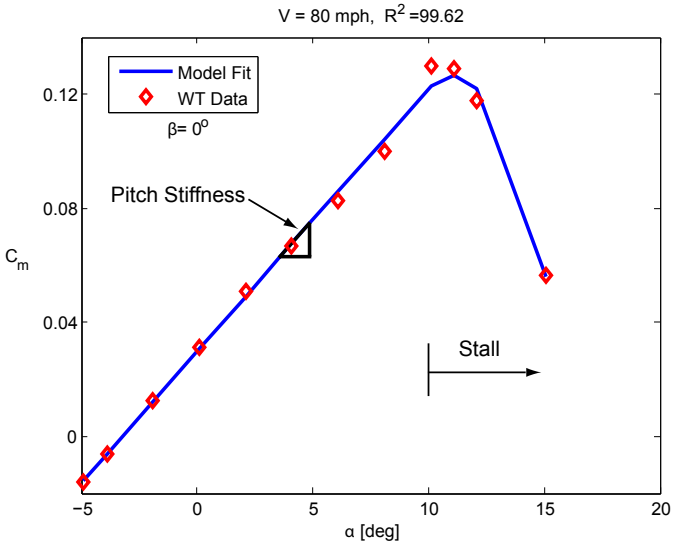

Figure 7.11: Static pitch moment about the pivot point.

[3]From the kinematic constraints of the model, it can be shown that the linear extension spring very closely approximates a linear torsional spring.

Substituting Eqs. (7.10,7.11[4],7.13) into Eq. (7.9) yields:

$$\begin{aligned} I_{yy}\ddot{\theta} &= \overbrace{M_0 + WL - \tau_0}^{trim} + \overbrace{(WL[\phi - \alpha_0] + M_\alpha - \kappa_{eq})}^{static\ stability}\Delta\alpha + \overbrace{(M_\mu + M_q)}^{damping}\Delta q \\ &+ \overbrace{M_{S(\alpha^2)}}^{stall} S(\Delta\alpha^2) \end{aligned} \tag{7.14}$$

where M_q and M_μ were added to *representatively*[5] account for aerodynamic and frictional damping, respectively. The first group of bracketed terms in Eq. (7.14) shows that the spring provides the necessary restoring torque to oppose the aerodynamic and gravitational moments at trim. This can be seen by setting $\Delta\alpha = \Delta q = S(\Delta\alpha^2) = \ddot{\theta} = 0$ and solving for τ_0:

$$\tau_0 = M_0 + WL \tag{7.15}$$

The second group of bracketed terms shows that the spring stiffness, κ_{eq}, acts as a gain on the system, achieving static stability when:

$$\kappa_{eq} > WL[\phi - \alpha_0] + M_\alpha \tag{7.16}$$

Note that because the c.g. is aft of the bearings axis, the gravitational force introduces an additional term of the form: $WL[\phi - \alpha_0]$, which tends further to destabilize the system. Finally, the third and fourth groups of bracketed terms represent damping and stall, respectively.

[4]Equation (7.11) is expressed in dimensional form.

[5]The actual dynamic model structure is determined in Eq. (7.19).

7.2.4 Spring-Mass Damper System

In order to overcome the problem of collinearity between the aerodynamic (M_0,M_α,M_q) and mechanical parameters (τ_0,κ_{eq},M_μ), the model was subjected to no wind (0 mph) oscillation tests. This bypasses the problem of collinearity and allows the mechanical parameters to be independently quantified. Dropping all aerodynamic terms in Eq. (7.14) and moving the gravitational moment, expressed in nonlinear form, to the right hand side yields:

$$-\tau_0 - \kappa_{eq}\Delta\alpha + M_\mu \Delta q = I_{yy}\ddot{\theta} - WL\cos(\phi - \Delta\alpha) \tag{7.17}$$

The parameters on the left hand side of Eq. (7.17) were the unknown parameters, whereas the terms on the right hand side were treated as the 'measured output'. The parameter estimates and coefficients of determination are given in Table 7.2 for the two spring configurations.

Table 7.2: Mechanical parameter estimates (2-σ standard deviation).

Trim Condition	τ_0 [ft-lb]	κ_{eq} [ft-lb/rad]	M_μ [ft-lb/rad-s]	R^2
$\alpha_0 = -6.25^o$	17.00 (0.0308)	60.57 (1.61)	-1.13 (0.215)	99.27
$\alpha_0 = \quad 0.50^o$	16.78 (0.0771)	60.42 (1.49)	-1.12 (0.210)	98.74

The small variance and high R^2 values indicate an excellent model and parameter estimates. Validation was made by substituting values for WL and τ_0 in Eq. (7.15), and dropping the aerodynamic term M_0. The resulting agrement, $17.0 \cong 17.04$, was excellent. Finally, stability was checked by way of Eq. (7.16), where the static parameter estimate of M_{m_α} was calculated from Fig. 7.11 to a worst case of 90 mph.

The result, $60.57 > 54.63$, shows that stability is guaranteed at all test speeds with, at minimum, a 10% margin for error.

7.2.5 Dynamic Model Structure Determination

After resolving the issues of collinearity with the mass-spring damper parameters, the equation of motion given by Eq. (7.9) was modified by adding the effects of the spring given by Eq. (7.13), replacing M_{cg} with the nonlinear form given by Eq. (7.10), and moving all known parameters to the right hand side:

$$\sum \text{Pitch Aerodynamics} = I_{yy}\ddot{\theta} - WL\cos(\phi - \Delta\alpha) - \tau_0 - \kappa_{eq}\Delta\alpha \tag{7.18}$$

Note that the aerodynamic model structure in Eq. (7.18) is yet to be determined from the *dynamic* pitch data: the model structure used previously in Eq. (7.14) is based on the *static* test data and served only as an aid in determining a proper spring constant for safe dynamic testing. The model structure of the dynamic pitch moments was obtained using $\boldsymbol{z} = I_{yy}\ddot{\theta} - WL\cos(\phi - \Delta\alpha) - \tau_0 - \kappa_{eq}\Delta\alpha$ as the 'measured output' and $\boldsymbol{X} = [\alpha\ q\ S(\alpha)]$ as the pool of candidate regressors. Each regressor had its mean value removed to prevent correlation with the bias term and allow for a true multivariate Taylor series expansion [26]. The location of the spline term, $S(\alpha)$, varied based on the spring configuration (trim condition), and direction and magnitude of the initial condition, $\pm\theta_i$. Figure 7.9a shows that the first spring configuration has a large trim angle that passes through the static stall angle of $\alpha = 10^o$ as tunnel speed increased. Consequently, peak amplitudes of the

first spring configuration encounter periods of nonlinear stall and had the following model structure:

$$C_m = C_{m_0} + C_{m_\alpha}\Delta\alpha + C_{m_{S(\alpha)}}S(\alpha) + C_{m_{\hat{q}}}\Delta\hat{q} \tag{7.19}$$

where:

$$C_{m_\alpha} = \left.\frac{\partial C_m}{\partial \alpha}\right|_0 \qquad C_{m_{S(\alpha)}} = \left.\frac{\partial C_m}{\partial \alpha}\right|_0 \text{for } \alpha > 12^o \qquad C_{m_{\hat{q}}} = \left.\frac{\partial C_m}{\partial \hat{q}}\right|_0 \qquad \hat{q} = \frac{q\bar{c}}{2V_0} \tag{7.20}$$

A randomly selected graph of a typical model fit is shown in Fig. 7.12, with coefficient of determination $R^2 = 96.38$. The residual, shown in the lower subplot, is zero mean with little deterministic content.

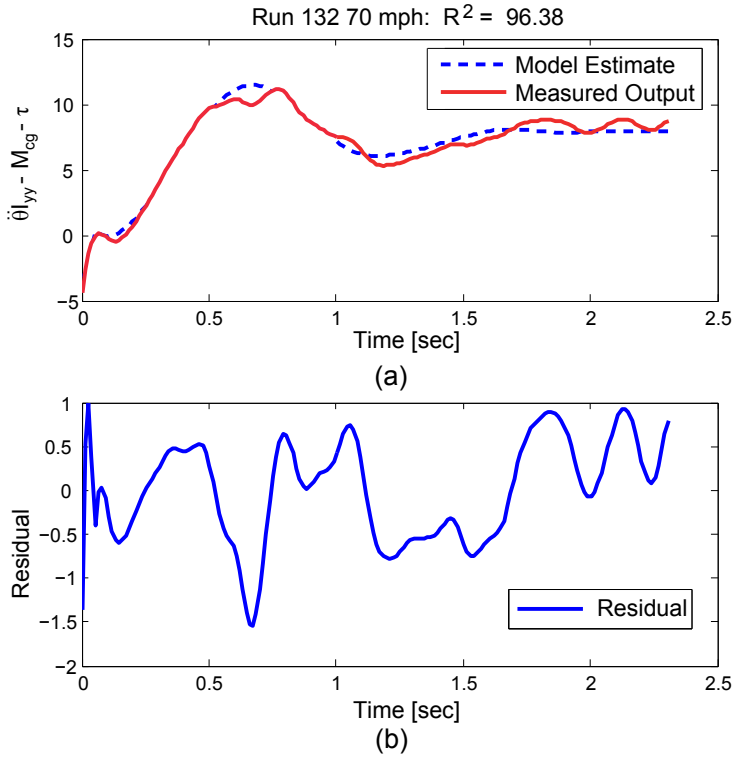

Figure 7.12: Controls neutral pitch perturbation (High α spring geometry).

7.2.6 Parameter Estimation

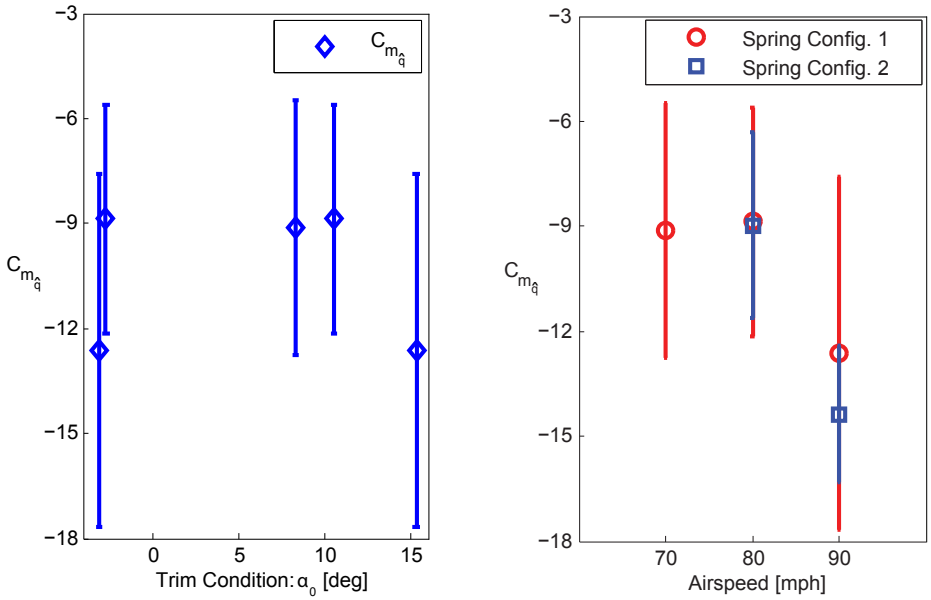

(a) Variation with trim condition.

(b) Variation with airspeed.

Figure 7.13: Damping parameter estimates vs. tunnel speed & trim condition with 95% CI.

The damping parameter estimates are plotted in Fig. 7.13, with each point in the test matrix was repeated four times and averaged to improve estimation accuracy. In Fig. 7.13a tunnel speed is the abscissa, with the first and second spring configurations plotted in red and blue, respectively. Despite two different spring configurations, the 80 & 90 mph runs are repeatable, with similar error bounds at 80 mph. In addition, there appears to be increasing damping (more negative $C_{m_{\hat{q}}}$) with tunnel speed. In Fig. 7.13b, the damping parameters are plotted with trim condition as the abscissa. Note that variation in trim condition was a result of the combination of spring configuration and tunnel speed (Fig. 7.9). The data shows no significant variation; therefore, changes in $C_{m_{\hat{q}}}$ were attributed solely to freestream

velocity. Finally, note that the spread in the damping parameters relative to the mean value is significantly larger for the pitch data.

7.2.7 Comparison of Static and Dynamic Data

Table 7.3: Percent error between static and dynamic parameter estimates.

Spring Config.	Tunnel Speed	C_{m_α}
1	70 mph	6.60%
1	80 mph	12.93%
1	90 mph	14.37%
2	80 mph	9.07%
2	90 mph	23.37%

The aerodynamic model structure and parameter estimates calculated from the static and dynamic runs were compared to quantify changes in the flowfield due to rotation rates. The difference in the static and dynamic data was calculated using the percent error methodology of the stiffness terms using Eq. 7.7 and are given in Table 7.3. Remarkably, C_{m_α} compared favorably despite the significant collinearity between the spring, gravitational, and aerodynamic torques. The average error was found to be 14% and compares better than the yaw stiffness term, C_{n_β}, which had errors upwards of 46% despite R^2 value was as high as 98%. This indicates that the flowfield has a significantly lower sensitivity to pitch rates, as compared to yaw. Again, some of the error in the parameter estimates are due to inaccuracies in the terms (I_{yy}, L, ϕ), which were estimated in Solid Works and are only as accurate as the material property definitions. Finally, part of the error is due to the unsteady $\dot{\alpha}$ term, because it is not truly a derivative but dependent on the entire past history of the flow [25]. This error was assumed to be low because the reduced frequency of

oscillations, which provides insight into the effects of the time history on the angle of attack, was small.

7.3 Origin Offsets

The parameter estimation process in the two previous sections occurred about the bearing axis of rotation, which differed from the design c.g. of the aircraft. Correction of the parameter estimates due to c.g. offsets is:

$$\begin{bmatrix} C_l \\ C_m \\ C_n \end{bmatrix}_{cg} = \begin{bmatrix} C_l \\ C_m \\ C_n \end{bmatrix}_{pivot} + \begin{bmatrix} 1/b & 0 & 0 \\ 0 & 1/\bar{c} & 0 \\ 0 & 0 & 1/b \end{bmatrix} \left\{ \begin{bmatrix} (x_{pivot} - x_{cg}) \\ (y_{pivot} - y_{cg}) \\ (z_{pivot} - z_{cg}) \end{bmatrix} \times \begin{bmatrix} C_X \\ C_Y \\ C_Z \end{bmatrix} \right\} \tag{7.21}$$

where b is the model wingspan, $\bar{c}$ is the average geometric chord, and ($[x_{cg}\ y_{cg}\ z_{cg}]$, $[x_{pivot}\ y_{pivot}\ z_{pivot}]$) are the coordinates of the aircraft cg and pivot point, respectively. Recall that the limitations in the experiment did not allow for the determination of the rate dependent aerodynamic forces; therefore, the last term in Eq. (7.21) is zero. Consequently, damping parameters estimated can be added directly to the static database.

7.4 Assumptions

Inherent to the test methodology is that static and dynamic tests can be performed independently and added linearly to form a complete aerodynamic database:

$$C_i = C_{i,static} + C_{i,dynamic} \text{ for } i = l, m, n \tag{7.22}$$

The comparative analysis of the yaw axis data in Section 7.1.4 shows that this approximation is far from ideal because of the large changes in C_{n_β} (33-46%) highlight the inherent differences between static and dynamic data. In contrast, the pitch axis parameter C_{m_α} differed, on average, by 14% meeting the assumptions of Eq. (7.22) fairly well. The comparative analysis between the static and dynamic data highlights the reason why time varying flight test data is always preferred for high fidelity modeling and is regarded as 'truth'. Finally, recall that the tip mounted propulsion systems were not included in the scale model, which can significantly alter the damping coefficients due to interaction effects.

Chapter 8

Simulink Math Models

8.1 Nonlinear Simulation

This section describes the topology of the math models created in the Simulink environment of MATLAB using the Aerospace Toolbox. The purpose of the simulation is to facilitate the development of future controls algorithms and evaluate the accuracy of linearized models. The simulation fuses the aerodynamic coefficients obtained from static and dynamic testing with CFD predictions of high speed flight (200 mph), wing tip mounted propulsion systems, and thurst vectoring exhaust vanes. Three function blocks are described in this preamble, as they will be referenced frequently throughout the writeup.

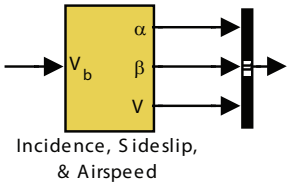

Figure 8.1: Wind frame function block.

The first built in function, shown in Fig. 8.1, transforms the body frame velocities (u, v, w) into the wind frame (V, α, β) using the standard relations:

$$V = \sqrt{u^2 + v^2 + w^2} \tag{8.1}$$

$$\alpha = \arctan \frac{w}{u} \tag{8.2}$$

$$\beta = \arcsin \frac{v}{V} \tag{8.3}$$

The duct rotation matrices and their associated Simulink subfunction blocks are described next. The duct rotation sequence is pitch angle, followed by heading angle (yaw). The body to duct rotation sequence (subscripted 'BD') is given by:

$$R_{BD} = R_{yaw}(\delta_y) R_{pitch}(\delta_p) \tag{8.4}$$

where:

$$R_{pitch}(\delta_p) = \begin{bmatrix} \cos\delta_p & 0 & -\sin\delta_p \\ 0 & 1 & 0 \\ \sin\delta_p & 0 & \cos\delta_p \end{bmatrix} \tag{8.5}$$

$$R_{yaw}(\delta_y) = \begin{bmatrix} \cos\delta_y & \sin\delta_y & 0 \\ -\sin\delta_y & \cos\delta_y & 0 \\ 0 & 0 & 1 \end{bmatrix} \tag{8.6}$$

and δ_p, δ_y denote the duct pitch and yaw angles, respectively. The equivalent Simulink subfunctions of the rotation matrices are given in Figs. 8.2a-8.2b. Note that the reverse operation: going from the duct frame to the body frame (subscripted 'DB'), is accomplished by the reverse rotation sequence:

$$R_{DB} = R_{pitch}(-\delta_p) R_{yaw}(-\delta_y) \tag{8.7}$$

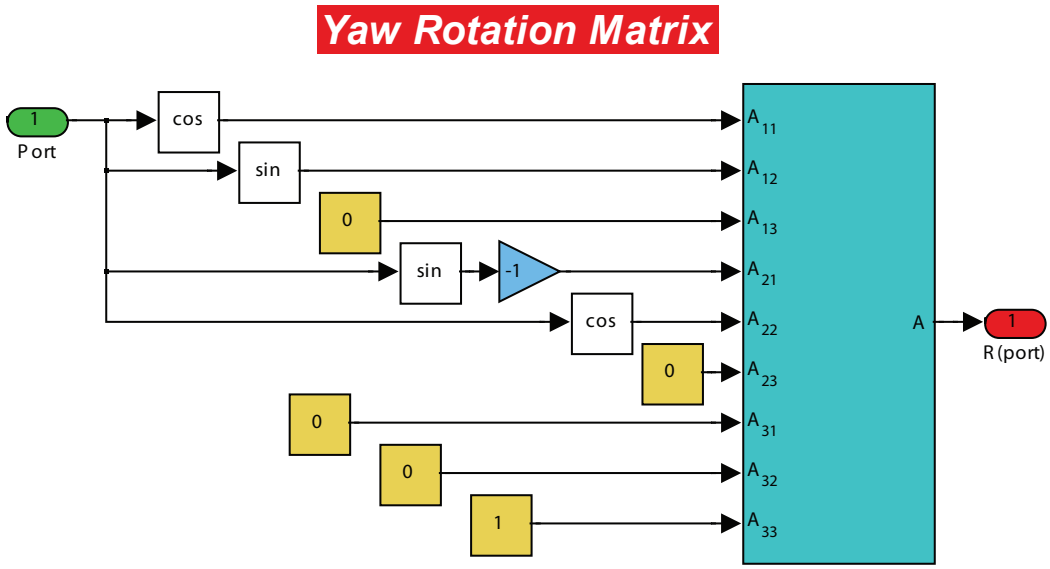

(a) R_{yaw}

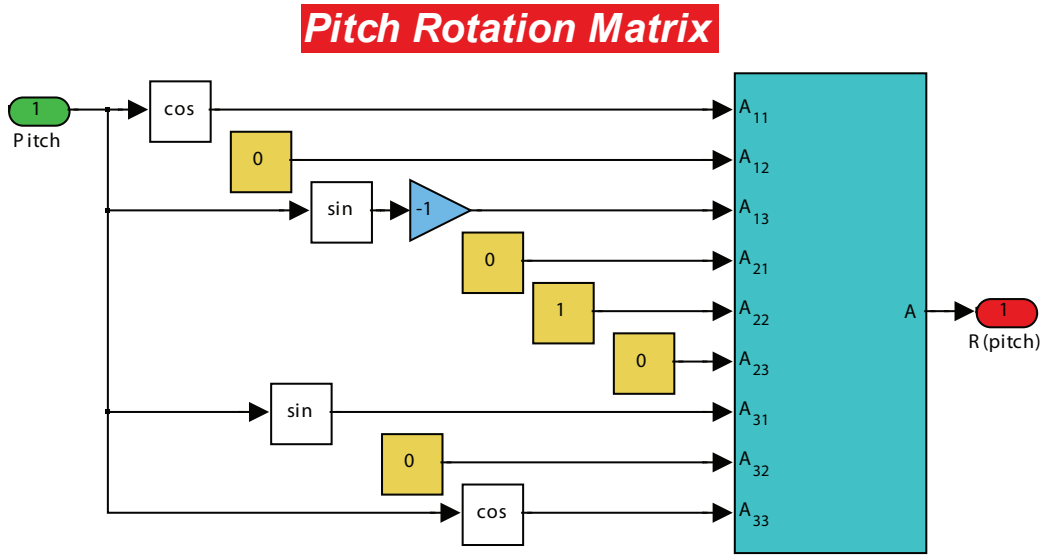

(b) R_{pitch}

Figure 8.2: Simulink duct rotation matrices.

8.2 Equations of Motion

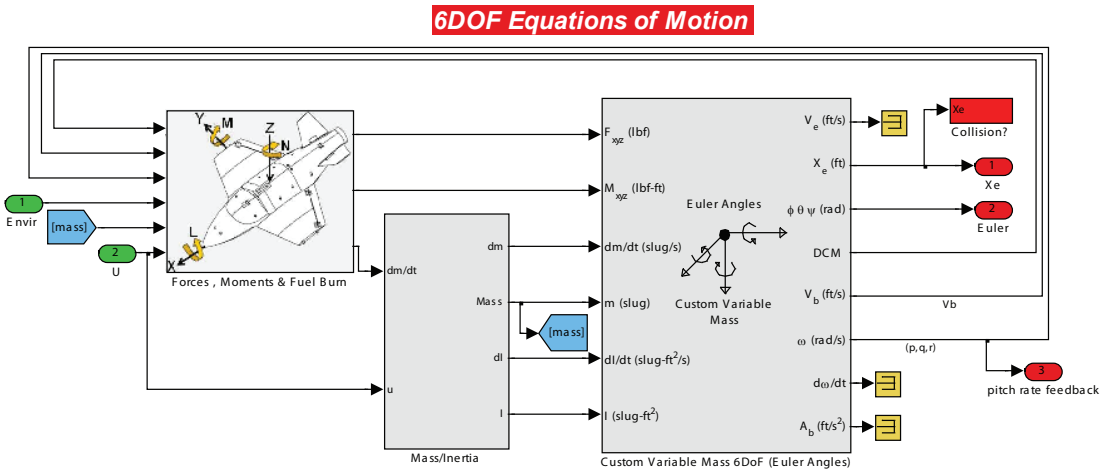

Figure 8.3: Equations of motion function block.

Integration of the equations of motion occurs in the subsystem shown in Fig. 8.3. At each time step in the simulation, the aerodynamic force-moment, and mass-inertial properties are calculated in the 'Forces, Moments & Fuel Burn' and 'Mass/Inertia' subsystems, respectively. These nonlinear parameters serve as inputs to the 'Custom Variable Mass 6DoF (Euler Angles)' block. The 6DoF block solves the translational and rotational equations of motion in the body fixed frame[1], given as:

$$[F^B] = \begin{bmatrix} X \\ Y \\ Z \end{bmatrix} = m([\dot{V^B}] + [\omega^B] \times [V^B]) + \dot{m}[V^B] \tag{8.8}$$

and

$$[M^B] = \begin{bmatrix} L \\ M \\ N \end{bmatrix} = [I^B][\dot{\omega^B}] + [\omega^B] \times ([I^B][\omega^B]) + [\dot{I^B}][\omega^B] \tag{8.9}$$

[1] http://www.mathworks.com/access/helpdesk_r13/help/toolbox/aeroblks/6dofeulerangles.html

where

$$[V^B] = \begin{bmatrix} u \\ v \\ w \end{bmatrix} \quad [\omega^B] = \begin{bmatrix} p \\ q \\ r \end{bmatrix} \quad [I^B] = \begin{bmatrix} I_{xx} & -I_{xy} & -I_{xz} \\ I_{yx} & I_{yy} & -I_{yz} \\ I_{zx} & -I_{zy} & I_{zz} \end{bmatrix} \quad [\dot{I^B}] = \begin{bmatrix} \dot{I}_{xx} & -\dot{I}_{xy} & -\dot{I}_{xz} \\ \dot{I}_{yx} & \dot{I}_{yy} & -\dot{I}_{yz} \\ \dot{I}_{zx} & -\dot{I}_{zy} & \dot{I}_{zz} \end{bmatrix} \tag{8.10}$$

where the superscipt 'B' notation indicates a body axis reference frame with an origin at the aircraft mass center, (u,v,w) are the body velocities, (p,q,r) are the body rotation rates, (X,Y,Z) are the body forces, (L,M,N) are the body moments, and $([I^B], [\dot{I^B}])$ are the body inertia and inertia rate tensors, respectively.

Integration of Eqs. (8.8)-(8.9) results in an updated state vector, which contains the aircraft Euler angles, direction cosine matrix, body frame angular rates, velocity, and position vectors in both the body and earth frames. The integration method uses the Ode45 Dormand-Prince solver with default relative tolerance (1e-3). The method and tolerance can be changed in the 'Configuration Parameters' menu depending on the desired accuracy or simulation speed. Note that the simulation runs fast enough in default settings for real time hardware-in-the-loop testing.

8.3 Environmental Properties

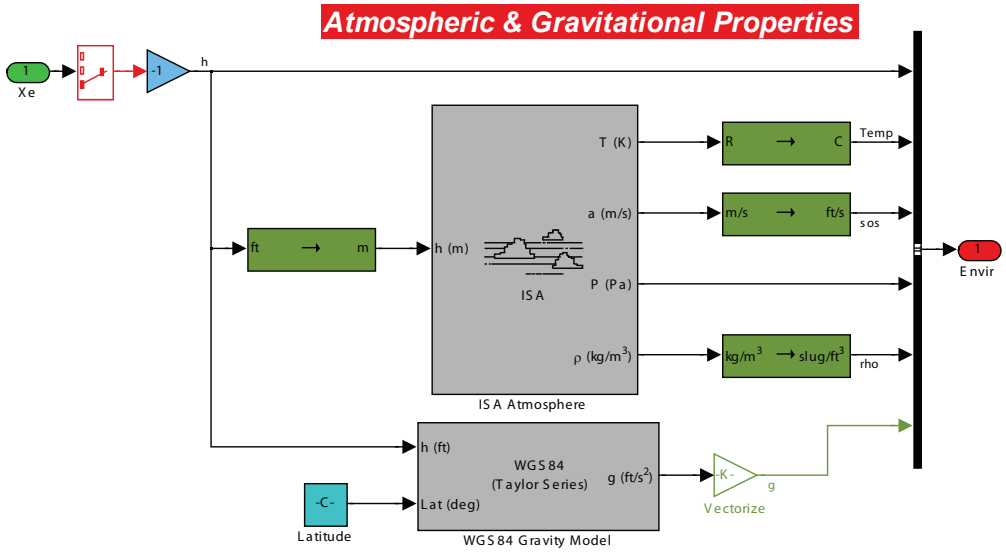

Figure 8.4: Atmospheric and gravitational parameters.

The 'Weather & Environment' subsystem provides atmospheric and gravitational data, shown in Fig. 8.4. The atmospheric properties are computed using the 1976 International Standard Atmosphere (ISA) model, which calculates the temperature, air density, and speed of sound (SoS). The magnitude of the gravitational force is calculated using the 1984 World Geodetic System (WGS84) representation of Earth's gravity, using a fixed latitude coordinate (Jessup, Maryland) and current altitude, labeled 'h'. Note that the altitude is the negative of the z-component in the north-east down (NED) earth fixed frame, which is accounted via the gain '-1' at the beginning of the diagram. In the future, additional built-in aerospace function blocks of the Dryden wind turbulence and wind shear models can be easily added within this subsystem to test control algorithms for robustness to environmental disturbances.

8.4 Control variables

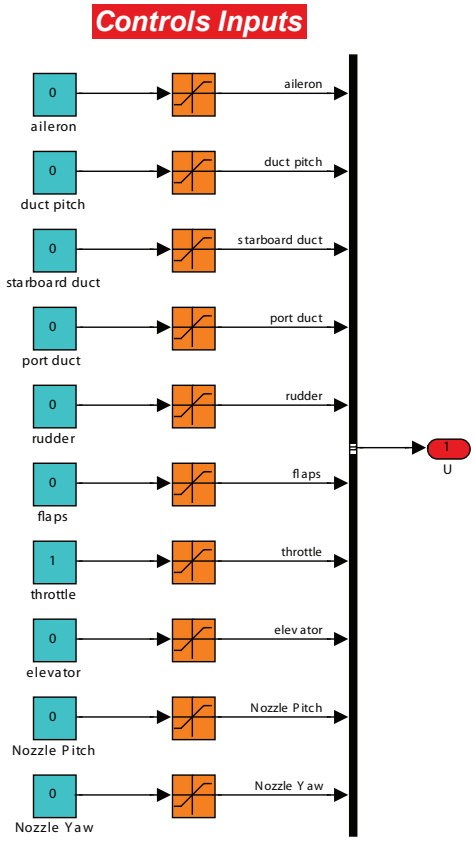

Figure 8.5: Simulation control inputs and saturation limits.

The control variables are set inside the controls input subfunction shown in Fig. 8.5, with the associated saturation limits specified in Table 8.1. The saturation blocks provide limitations on the allowable controls deflections, and are based on the analysis of Chapter 5. Nozzle inputs control deflecting vanes downstream the turboshaft engine. The 'duct pitch' input collectively positions both wingtip mounted ducts in pitch, while the port/starboard yaw inputs independently rotate each duct in yaw. All other control inputs follow standard aircraft convention defined in Subsection 4.5. For future refinement, actuator time delay blocks can be added downstream the saturation blocks, along with controls mixing routines for

the ruddervator and flaperon surfaces.

Table 8.1: Control surface saturation limits.

Control Surface	Saturation Limits
Aileron	$\pm 45^0$
Rudder	$\pm 30^0$
Elevator	$\pm 30^0$
Throttle	$0 - 100\%$
Flaps	$0 - 45^0$
Duct pitch	$0 - 90^0$
Starboard\port duct	$\pm 7.5^0$
Nozzle pitch	$\pm 45^0$
Nozzle yaw	$\pm 45^0$

8.5 Mass & Inertia Properties

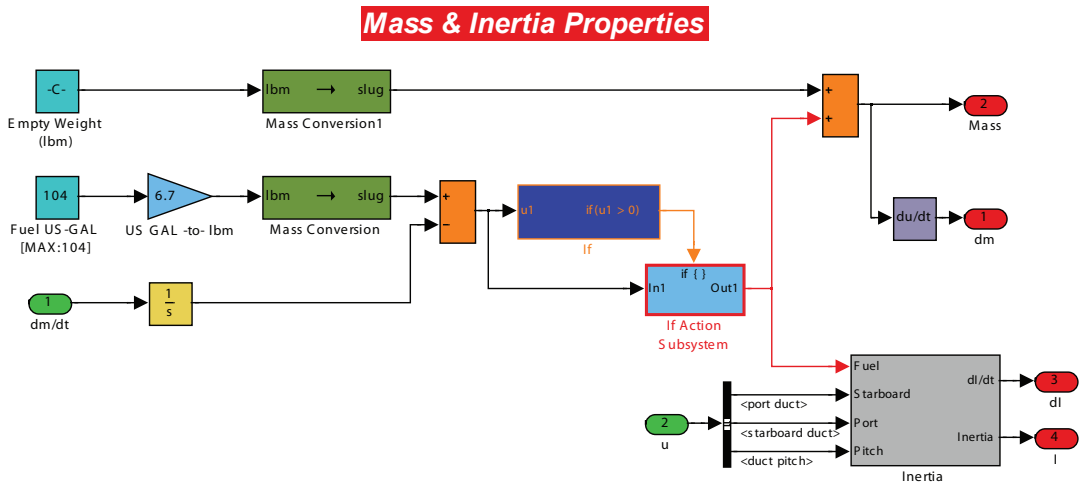

Figure 8.6: Calculation of mass and inertia properties.

The mass and inertial subsystem is shown in Fig. 8.6. The mass of the vehicle is a culmination of the basic empty weight and available fuel. The total fuel capacity is 104 U.S. gallons, which is reduced at each time step in proportion the specific fuel consumption (SFC) of the engine. The running total of fuel consumed is calculated via the integration block '$1/s$', which is then subtracted from the starting quantity. The conditional if-statement blocks set the fuel-mass to zero when the tanks are exhausted. Note that the c.g. of the aircraft is invariant to changes resulting from fuel burn because the fuel management system keeps the c.g. at a fixed location throughout flight by switching between fuel cells.

The calculation of the aircraft inertia, shown in Fig. 8.8, is a summation of the airframe, fuel, and duct components:

$$[I^B_{total}] = [I^B_{fuel-airframe}] + [I^B_{ducts}] \tag{8.11}$$

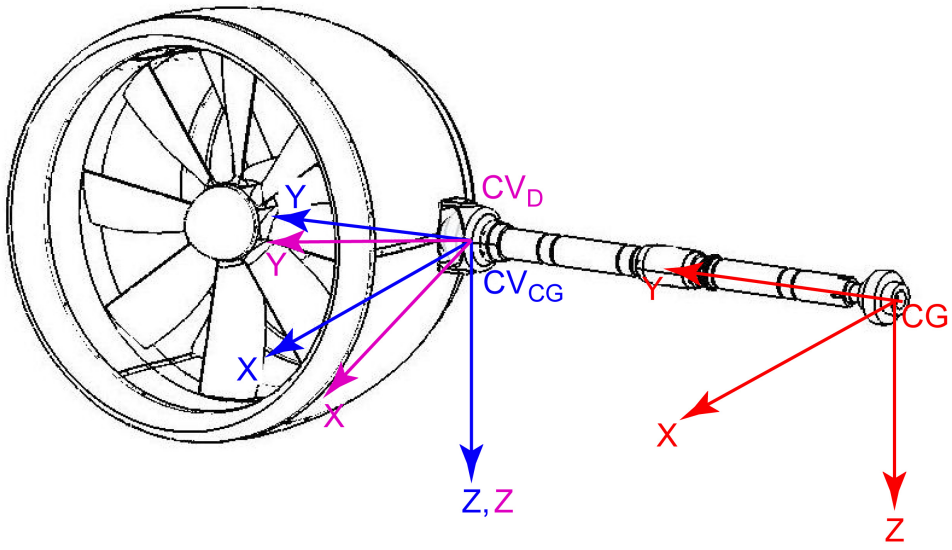

Figure 8.7: Duct frame and pivot point.

The fuel-airframe inertia matrix (enclosed by a red dash-dot boarder in Fig. 8.8) is calculated as a linear interpolation between the fully fueled and basic empty weight:

$$[I^B_{fuel-airframe}] = [I^B_{basic}] + \left(\frac{[I^B_{ramp}] - [I^B_{basic}]}{696.8} \right) fuel \tag{8.12}$$

where the fractional term is the rate of change in the fuel-airframe inertia matrix per lbf fuel, $fuel$ is the current fuel level in the simulation, and ($[I^B_{basic}]$, $[I^B_{ramp}]$) are the basic (no fuel) and ramp (fully fueled) airframe inertial matrices in the aircraft body frame (*excluding* contributions from the ducts), resectively.

The inertia matrices of the ducts are calculated about the constant-velocity (CV) joint at the duct-wing interface, shown in Fig. 8.7. This is subtle but important distinction, because the ducts do not pivot about their geometric center. The calculation of the duct inertia is as follows: first, the inertia of the duct $[I^D_{duct}]$ is calculated in the local duct body axis (superscript 'D') with an origin at the CV

joint, denoted D_{CV}. Next, the inertia matrix is rotated parallel to the airframe body axis C_{xyz} via the relation: $[R_{DB}][I^D_{duct}][R_{DB}]^T$ (this can be seen by the enclosed dark green dash-dot boarder in Fig. 8.8). Finally, the parallel axis theorem (expressed as $m_{duct}[D^2]$ and enclosed by a blue dash-dot boarder in Fig. 8.8) is employed to account for distance offsets from D_{CV} to C_{xyz}, Ref. [32]. The total transformation can be written as:

$$[I^B_{duct}] = [R_{DB}][I^D_{duct}][R_{DB}]^T + m_{duct}[D^2] \tag{8.13}$$

where

$$D = \begin{bmatrix} d_y^2 + d_z^2 & -d_x d_y & -d_x d_z \\ -d_x d_y & d_x^2 + d_z^2 & -d_y d_z \\ -d_x d_z & -d_y d_z & d_x^2 + d_y^2 \end{bmatrix} \tag{8.14}$$

with the equivalent Simulink subfunction block given in Fig. 8.9. This procedure is repeated for both the port and starboard duct, where:

$$[I^B_{ducts}] = [I^B_{duct}]_{port} + [I^B_{duct}]_{starboard} \tag{8.15}$$

Finally, the derivative of the total aircraft inertia is accounted for by the 'derivative' block in Fig. 8.6, which is output for later use in the equations of motion.

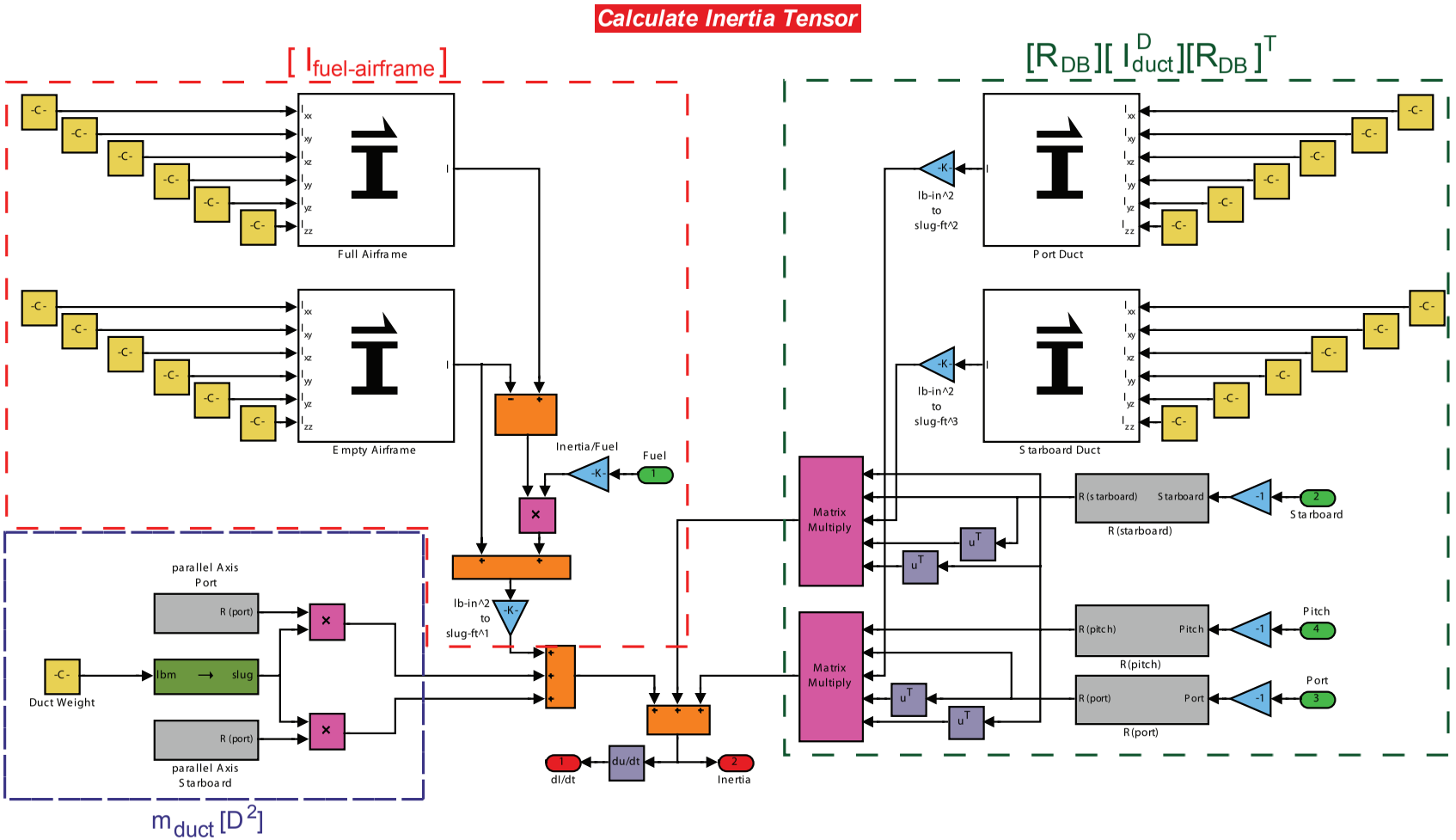

Figure 8.8: Inertia Subfunction

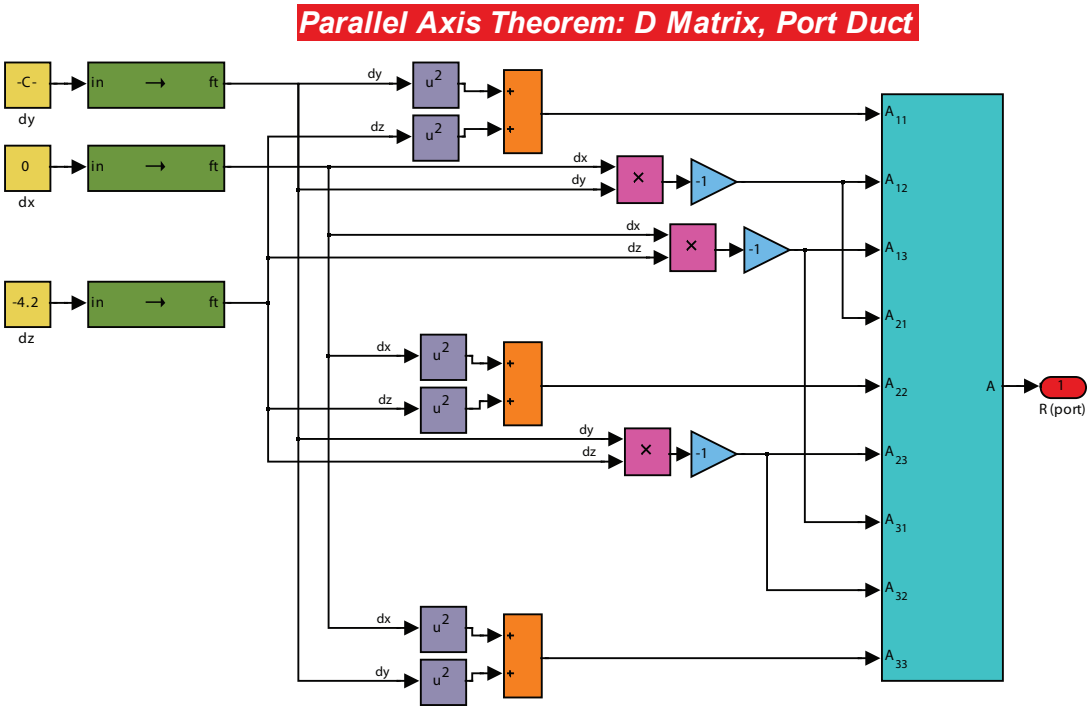

Figure 8.9: Parallel axis theorem (D matrix).

8.6 Static Lookup Tables

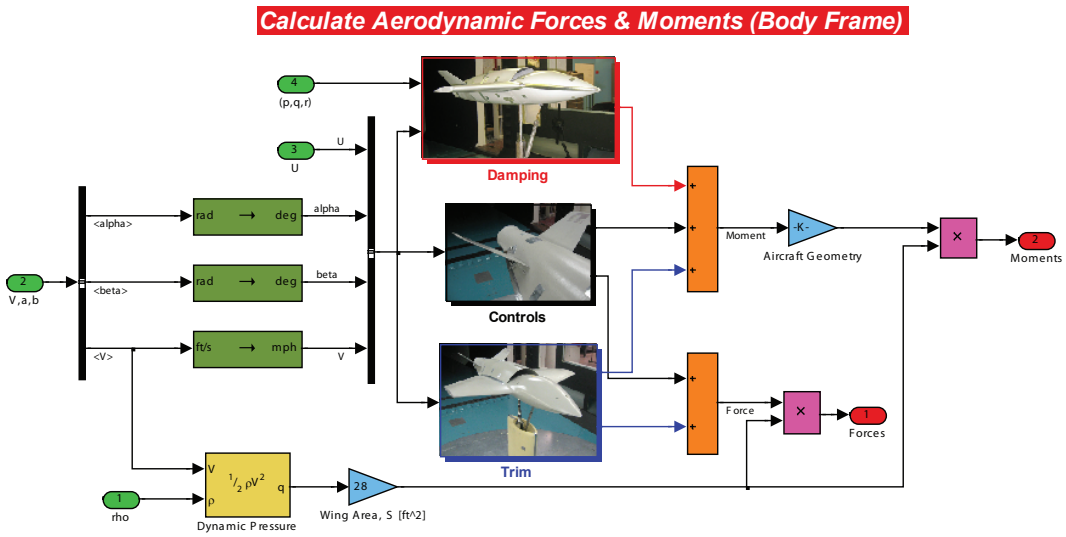

Figure 8.10: Aerodynamic lookup tables.

This section describes the construction of the static aerodynamic data sets used in the simulation environment. First, the wind frame data in Chapter 5 was converted into the body axis according to the transformation matrices in Section 4.5. Second, the data was formatted for use with the built-in Simulink interpolation block, which requires the data to have the same lookup indices for each explanatory variable. However, during wind tunnel testing, it is never possible to exactly reproduce the same combination of angle of attack and sideslip each time because the wind tunnel support has slop and there is some backlash in the gears. Furthermore, exact reproduction of tunnel speed is not possible due to inherent unsteadiness in the flow. Consequently, the data was converted to a common set of indices using a custom interpolation routine.

Next, the reflection method described in Section 5.5.3 was applied to expand

the raw data to include both positive and negative sideslip angles and controls deflections, as follows. The controls neutral, elevator, and rudder static runs were reflected to include positive sideslip angles, as only negative angles were tested. Finally, the rudder data was reflected in deflection angle, as only positive rudder deflections were tested. In addition, note that the flap control tests were performed at $\beta = 0$; therefore, the variation to sideslip is not included. Ailerons were tested at a fixed angle of attack ($\alpha = 6^o$) with varying sideslip angle, and then at symmetric flight condition ($\psi = 0^o$) with varying angle of attack. Consequently, perturbations of the ailerons are independently calculated due to sideslip and angle of attack, and added.

The data was then categorized according to stability and control. The stability data is depicted by the the 'trim' subfunction in Fig. 8.10. The controls data is compiled in the form of perturbation values, computed by subtracting the corresponding trim value from the control deflection value for a given combination of angle of attack, sideslip, and freestream velocity. This is done so that the control force and moment coefficients take on the peturbation form ΔC_δ.

The total static force and moment values are obtained via summation of the trim and control coefficients, and then scaled using the prototype wing area and reference geometry (average chord and wing span). Finally, physical values are realized by multiplying by the dynamic pressure.

8.7 Force & Moment Summation

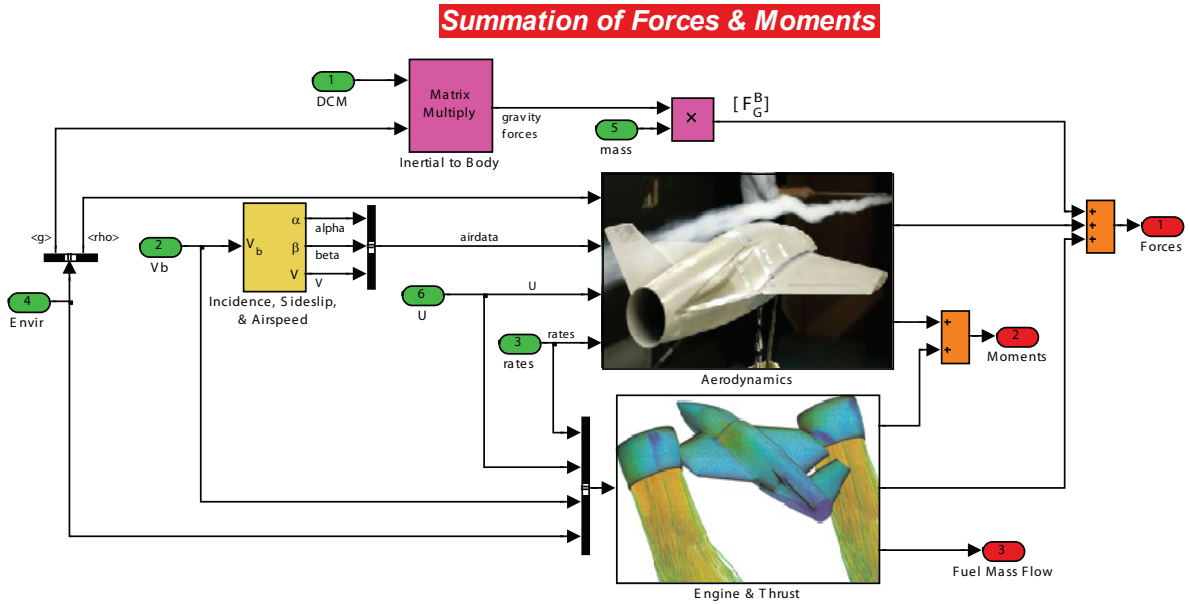

Figure 8.11: Aerodynamic, Graviational, and propulsive forces and moments.

The contents of the 'Forces, Moments & Fuel Burn' block are shown in Fig. 8.11. This block culminates the force and moment contributions from the propulsion systems, airframe aerodynamics, and external environment. The gravitational force in the Environemnt block of Section 8.3 is calculated in the earth fixed axis; therefore, conversion to the body axis occurs via matrix multiplication with the euler angle direction cosine matrix giving:

$$[F_G^B] = \begin{bmatrix} -mg\sin\theta \\ mg\sin\phi\cos\theta \\ mg\cos\phi\cos\theta \end{bmatrix} \tag{8.16}$$

Since the gravitational force acts through the aircraft center of mass, no torques are generated. Finally, engine SFC is output from the 'Engine & Thrust' block and serves as an input to mass inertia block.

8.8 Aerodynamic Damping

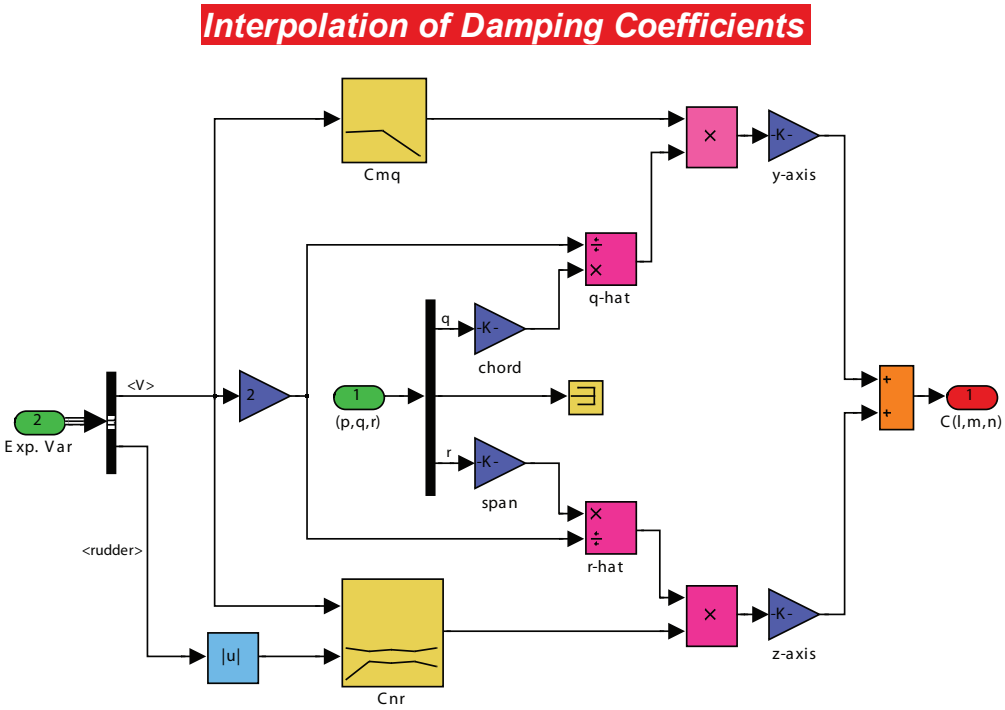

Figure 8.12: Aerodynamic damping function block diagram.

This subsystem (Fig. 8.12) adds the aerodynamic damping parameters ($C_{n_{\hat{r}}}$, $C_{m_{\hat{q}}}$) via the lookup tables 'Cmq' and 'Cnr'. The lookup table for $C_{m_{\hat{q}}}$ is a function of the freestream velocity and interpolates between 70-90 mph, as determined by the analysis in Section 7.2. Similarly, the lookup table for $C_{n_{\hat{r}}}$ is based on the freestream velocity and rudder deflection angle with interpolation limits between 80-120 mph and $\delta_r = 0 - 15^o$. The use of the absolute value function in front of the rudder input is based on the assumption that the damping is invariant to the sign of the deflection. The interpolation blocks have the 'use-end values' lookup method enabled, which prohibits extrapolation outside the ranges specified. This prevents the parameters taking on nonphysical values as the vehicle approaches hover conditions.

These parameters ($C_{n_{\hat{r}}}$, $C_{m_{\hat{q}}}$) are then multiplied by ($\hat{r}$, $\hat{q}$), given by Eqs. (7.4), (7.20), respectively, and repeated below:

$$\hat{q} = \frac{q\bar{c}}{2V_0} \qquad \hat{r} = \frac{rb}{2V_0} \tag{8.17}$$

where the multiplication is seen by tracing the signals from the division blocks labeled 'q-hat' & 'r-hat' and the values ($\bar{c}$='chord', b='span') are the *model scale* vehicle parameters. Finally, the scalar parameters ($C_{n_{\hat{r}}}\hat{r}$, $C_{m_{\hat{q}}}\hat{q}$) are expressed in body axis vector form via the gains labeled 'y-axis' and 'z-axis', respectively. The two vectors are then summed and outputted from the subsystem to be added to the static moment parameters (See Section 7.4). Damping effects from the ducts are accounted for using a quasi-steady based approach, which assumes a differential velocity distribution at each duct due to rotation rates, as specified in Section 8.9.

8.9 Engine Dynamics

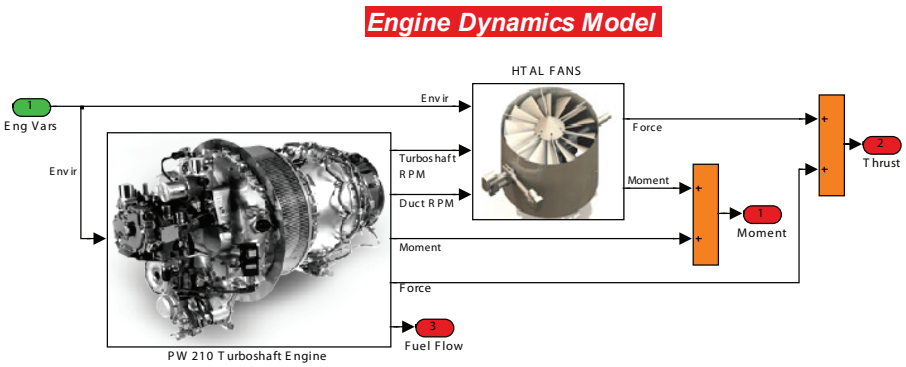

Figure 8.13: Engine dynamics subsystem.

The engine function block, shown in Fig. 8.13, calculates the forces and moments arising from the wingtip mounted ducts in the 'High Torque Arial Lift' (labeled HTAL) and center mounted turboshaft engine (labeled 'PW210 Turboshaft Engine'). At the time of this writting, a 1000SHP Pratt & Whittnay PW210 turboshaft engine is projected for use[2].

8.9.1 HTAL Fans

The contents of the 'HTAL Fans' subfunction block is shown in Fig. 8.14. In the 'Quasi-Steady Velocity' subfunction, the wind frame velocities are calculated for each duct. The velocities and fan RPM are then used in the 'Duct Forces & Moments' subfunction, which uses nonlinear lookup tables to calcualte the forces and moments in the duct frame. Next, the 'Thrust Vectoring' subfunction transforms the forces and moments into the aircraft body frame. Fianlly, the 'Gyroscopic Torques' subfunction calculates the moments generated on the aircraft due to the angular

[2]In addition to the Pratt & Whitney Canada PW210, the General Electric T700 and Honeywell T53 engines can be used in the aircraft.

momentum of rotating components.

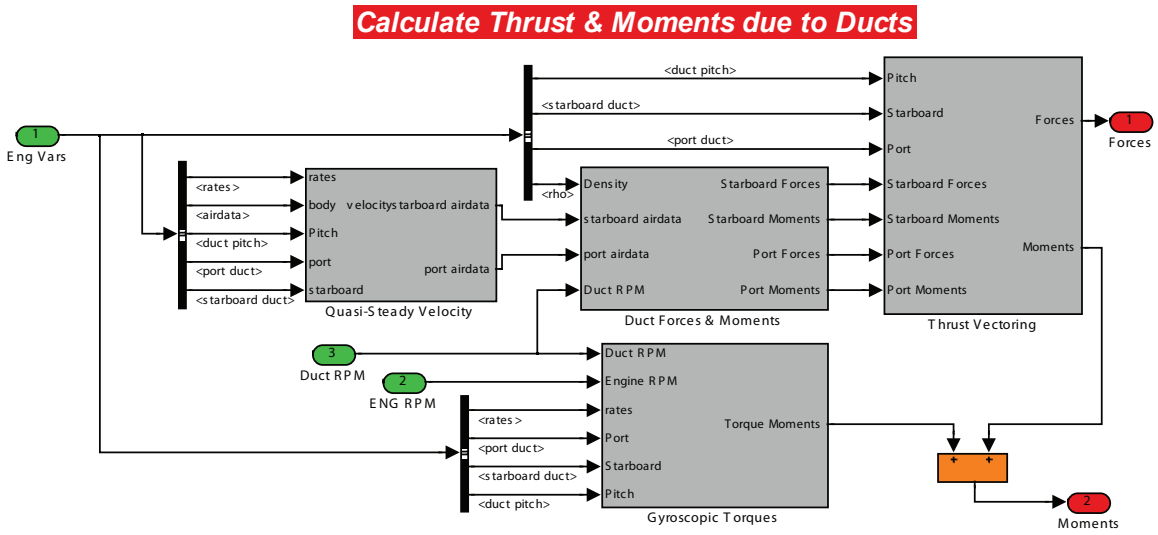

Figure 8.14: High level calculation of duct forces and moments.

The quasi-steady velocity subfunction, shown in Fig. 8.14, calculates the velocity seen at each duct, which is a combination of the velocity of the aircraft mass center (subscript cg) and velocity gradients stemming from rotation rates (subscript rot). The analysis calculates the change in velocity at each duct as follows:

$$[V^B_{duct}] = \begin{bmatrix} u \\ v \\ w \end{bmatrix}_{cg} + \left(\begin{bmatrix} p \\ q \\ r \end{bmatrix}_{cg} \times \begin{bmatrix} dx \\ dy \\ dz \end{bmatrix} \right)_{rot} \tag{8.18}$$

where $[p, q, r]^T$ are the body rotation rates, and $[dx, dy, dz]^T$ are the distances from the center of the duct to the aircraft cg. This is a first order approximation because the velocity change is assumed to occur at the center of the duct. In reality, each duct has a velocity gradient along its entire length and would require a substantial increase in the number of CFD test cases to fully encorporate.

After the port and starboard duct velocities are calculated, they are converted

to the duct body frame using the transformation:

$$[V^D_{duct}] = [R_{DB}][V^B_{duct}] \tag{8.19}$$

Finally, the duct body velocity components are converted into the duct wind frame using Eqs. (8.1)-(8.3). The equivalent Simulink operations are given in Fig. 8.15.

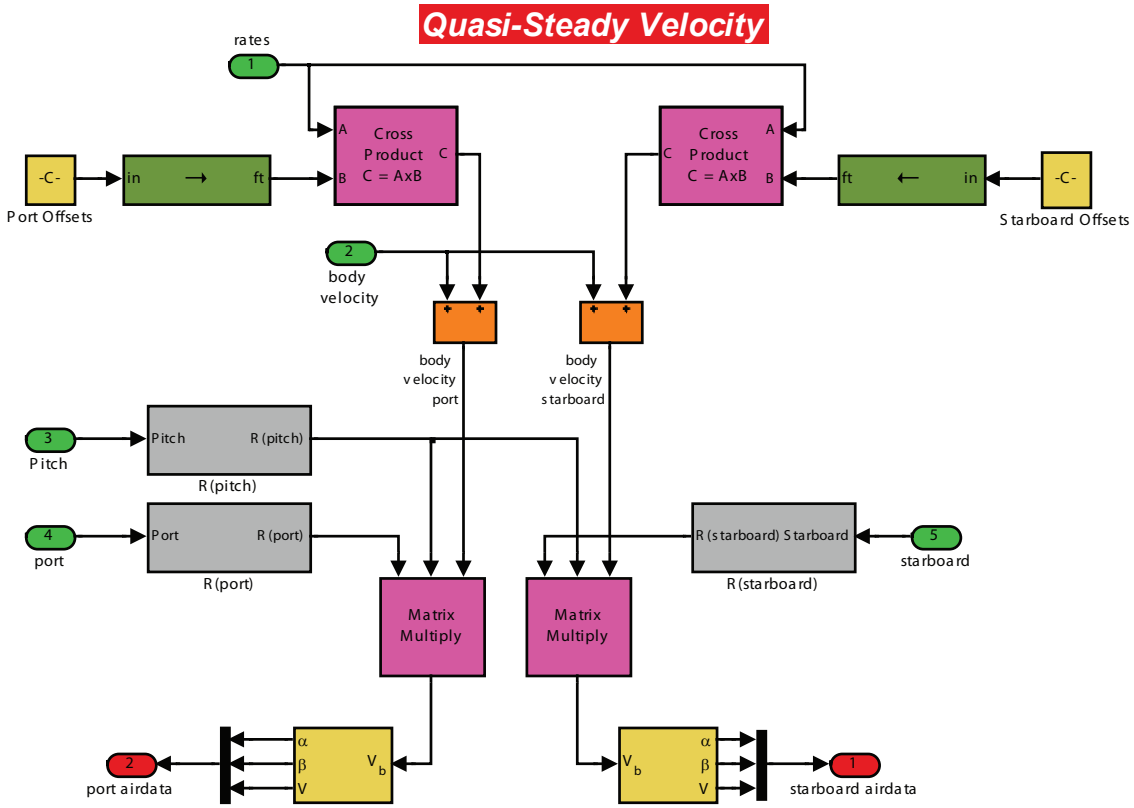

Figure 8.15: Quasi-steady duct velocities.

Once the quasi-steady velocities are calculated at each duct, the duct forces and moments are resolved in the duct body frame about an origin at center of the fan face. The forces and moments are generated in the 'Duct Forces & Moments' block in Fig. 8.14 using CFD generated nonlinear lookup tables. A complete description and

test matrix of the data is given in Appendix D. Note that because the CFD analysis was performed at prototype scale and standard atmosphere, all lookup values used are dimensional. Furthermore, counter rotation of the port and starboard ducts results in clockwise and anti-clockwise swirll within the rotor wake, respectively. As a result, the duct frame side force and yaw moment lookup values are equal and opposite for each duct for a similar set of lookup values. However, generally speaking, the net side force and yaw moment is not zero because the lookup values (angle of attack and airspeed) will differ on each duct due to body rotation rates and differential yaw control inputs. Finally, the effects of density altitude are accounted for by simple multiplication of the force and moment values by the ratio ρ_{alt}/ρ_{std}, where the subscript alt and std represent 'at altitude' and standard conditions, respectively.

Table 8.2: CFD propulsion test matrix

RPM	2500-6500
$[V_D^D]$	0 - 200 mph
γ	$0^o - 90^o$

Due to the symmetric nature of the ducts, the CFD tables were generated for a specified fan RPM, duct freestream velocity (in the duct body frame $[V_D^D]$), and freestream angle γ, as shown in Table 8.2. This was done to eliminate an explict dependency on sideslip angle, dramatically reducing the size of the test matrix. Instead, sideslip is accounted for by transforming the duct forces and moments through a roll angle ϕ. Through the use of this methodology, any value of (α,β) can be obtained.This transformation is mathematically equivalent to a conversion

in polar coordinates, shown in Fig. 8.16.

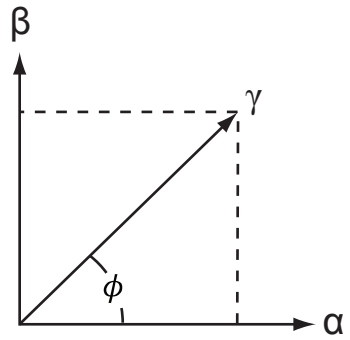

Figure 8.16: Polar coordinate Transformation.

In order to account for sideslip, a freestream angle γ was calculated using:

$$\gamma = \sqrt{\alpha^2 + \beta^2} \tag{8.20}$$

and

$$\phi = \arctan \frac{\alpha}{\beta} \tag{8.21}$$

with (γ, RPM, $[V_D^D]$) as inputs, the pre-rotation duct frame forces $[F_\gamma^D]$ and moments $[M_\gamma^D]$ are interpolated from the test matrix data. Next, these values are rotated in roll by an angle γ to produce the duct frame forces and moments:

$$[F_D^D] = [R_\phi][F_\gamma^D] \qquad\qquad [M_D^D] = [R_\phi][M_\gamma^D] \tag{8.22}$$

where

$$R_\phi = \begin{bmatrix} 1 & 0 & 0 \\ 0 & \cos\phi & \sin\phi \\ 0 & -\sin\phi & \cos\phi \end{bmatrix} \tag{8.23}$$

These operations are performed in the Simulink diagram of Fig. 8.17.

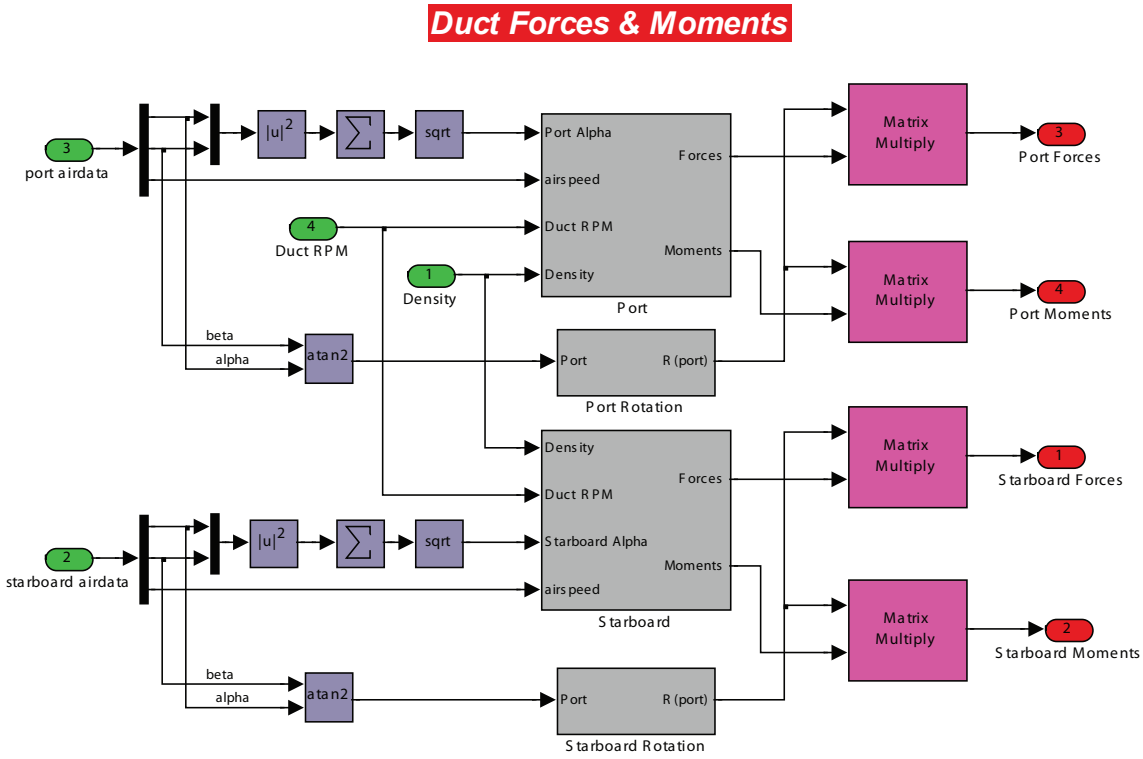

Figure 8.17: Duct parameter transformation and Force/Moment lookup.

Next, the duct frame moments are resolved about an origin at the wing-duct CV joint (with axis aligned with the duct) using the relation:

$$[M^D_{CV}] = [M^D_D] + ([r^D_{CV/D}] \times [F^D_D]) \tag{8.24}$$

where $[r^D_{CV/D}]$ is the offset between the center of the fan face and CV joint, expressed in the duct frame. Note that forces are invariant to origin offsets. At this point, the forces and moments are resolved about the CV joint, but still aligned with the body axis of the duct. The next step is to transform the axis so that they are parallel to the aircraft body axis (but still with an origin at the CV joint). The transformation

is:

$$[F^B_{CV}] = [R_{BD}][F^D_{CV}] \qquad [M^B_{CV}] = [R_{BD}][M^D_{CV}] \tag{8.25}$$

Finally, the origin is corrected to coincide with the aircraft center of mass using the relation:

$$[M^B_{cg}] = [M^B_D] + ([r^B_{cg/CV}] \times [F^B_{CV}]) \tag{8.26}$$

where $[r^B_{cg/CV}]$ is the offset between the CV joint and aircraft center of mass, expressed in the aircraft body frame. The equivalent simulink operations are given in Fig. 8.18.

Finally, it is important to note that the difference in velocities as seen by the port and starboard ducts due to rotation rates produces quasi-steady damping effects. This damping is due only to the ducts, whereas damping contributions from the bare airframe are accounted for in Section 8.8.

Gyroscopic contributions from the duct fans and turboshaft engine are accounted for in 'Gyroscopic Torques' block of Fig. 8.19. The gyroscopic torques result from the angular momentum of the rotating components, expressed as:

$$h_p = \begin{bmatrix} I_p\Omega_p & 0 & 0 \end{bmatrix}^T \tag{8.27}$$

where I_p is the polar moment of inertia of the rotating components, Ω_p is the angular velocity of said component, and the subscript 'p' stands for the propulsion system. Note here that h_p is expressed in the frame of the rotating component of interest. In addition, because the port and starboard ducts counter rotate, their angular velocities must satisfy: $\Omega_{fan,port} = -\Omega_{fan,starboard}$. For each fan, the angular

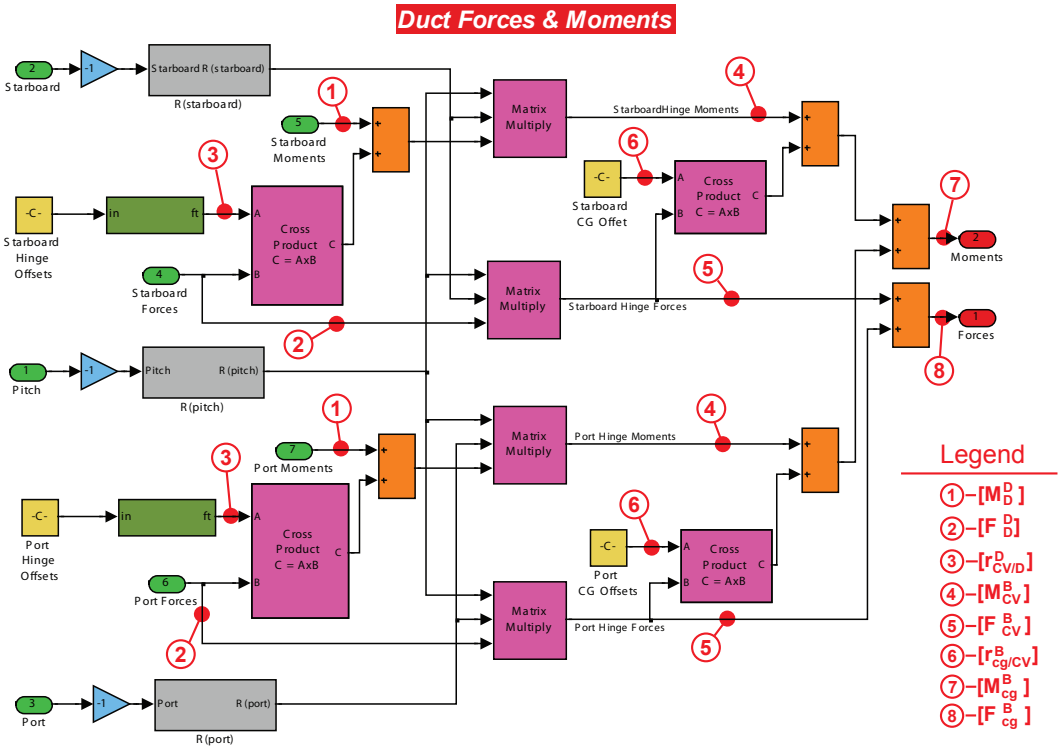

Figure 8.18: Conversion of duct forces and moments to aircraft body frame.

momentum can be expressed in the body frame as:

$$[h^B_{fan}] = [R_{BD}][h^D_{fan}] \tag{8.28}$$

The angular velocity of the center mounted turboshaft engine, aligned with the body x-axis, is:

$$\Omega_T = \eta\Omega_{fan} \tag{8.29}$$

where η is the gear ratio between the ducts and turbine, Ω_{fan} is the fan angular velocity, and Ω_T is the angular velocity of the rotating components in the turboshaft

engine. Consequnetly, the angular momentum of the turboshaft engine is:

$$[h_T^B] = \begin{bmatrix} I_T\Omega_T & 0 & 0 \end{bmatrix}^T \tag{8.30}$$

where $[h_T^B]$ is the angular moment of the turboshaft engine in the aircraft body frame, I_T is the polar moment of inertia of the rotating components, and Ω_T is the angular velocity of the rotating components. The total angular momentum in the body frame is then:

$$[h_{total}^B] = [h_{fan,port}^B] + [h_{fan,starboard}^B] + [h_T^B] \tag{8.31}$$

The gyroscopic couples generated are then expressed using the transport equation:

$$[M_T^B] = \frac{d}{dt}([h_{total}^B]) = [\dot{h}_{total}^B] + ([\omega^B] \times [h_{total}^B]) \tag{8.32}$$

where $[\omega^B]$ is defined in Eq. (8.10), $[h_{total}^B]$ is defined above, and $[M_T^B]$ is the body axis moments due to gyroscopic couplings. The first term in Eq. (8.32) represents local transients in the angular velocities of the rotating components: i.e. spool-up or spool-down. The second term represents moments generated as a result of rotations of the aircraft body axis relative to an earth fixed frame. For this analysis, the first term is assumed negligible as compared to the second term and therefore dropped. The Simulink function of the gyroscopic couples is given in Fig. 8.19.

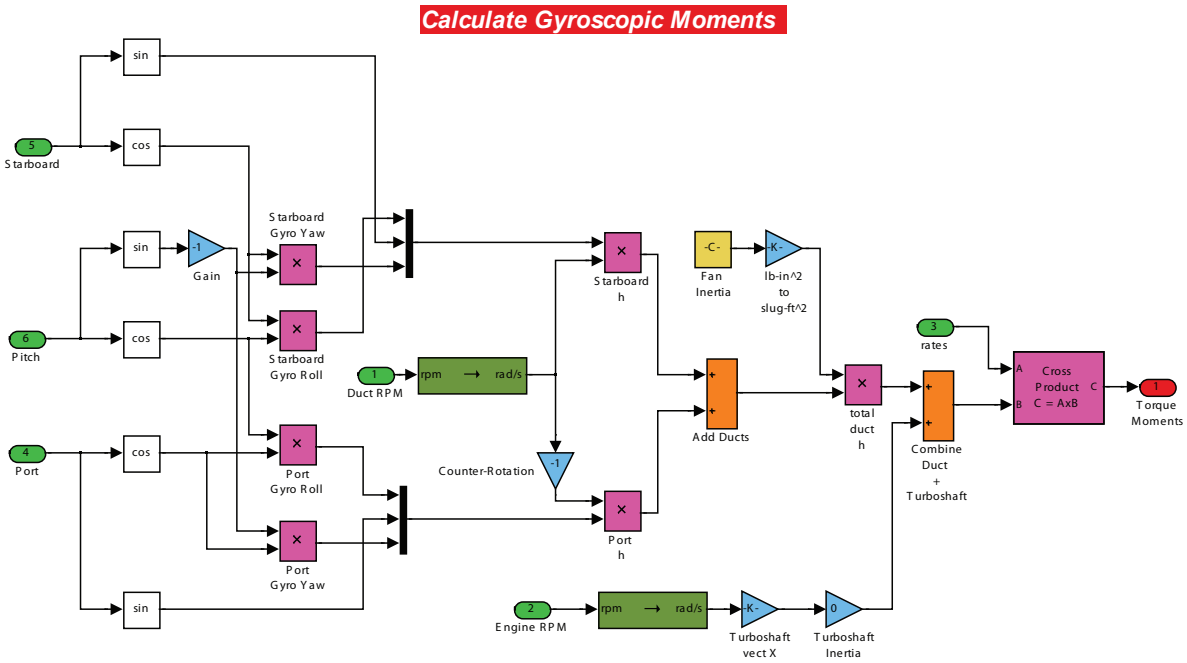

Figure 8.19: Gyroscopic couplings.

8.10 Open Loop Simulation

The results of a simple open-loop controls neutral simulation plot are presented in this section to observe the evolution of the aircraft dynamics. The aircraft was initialized at 5000ft altitude, with the attitude and body rates set to zero (steady wings level flight). In addition, the airspeed was initialized at 160kts, angle of attack $\alpha = 5^o$, and sideslip $\beta = 0^o$. The aircraft position plots, shown in Fig. 8.20a, indicate that the aircraft is slowly losing altitude (as seen by state Ze). Similarly, the forward position, Xe, increases linearly. The average forward velocity from this plot is roughly 165kts, and follows from the conversion of potential to kinetic energy during the descent. Similarly, this trend can also be seen in the airdata plot in Fig. 8.20b. In this plot, it also indicates that the angle of attack and sideslip quickly diverge, a tell-tale sign of an unstable system. The oscillatory behavior is indicative of a short period limit cycle, and is also seen in the attitude and body rate plots of Fig. 8.20c and Fig. 8.20d, respectively. Interestingly, the body pitch rate, p, in Fig. 8.20d appears to take on a limit cycle; meanwhile, the yaw rate term diverges almost linearly.

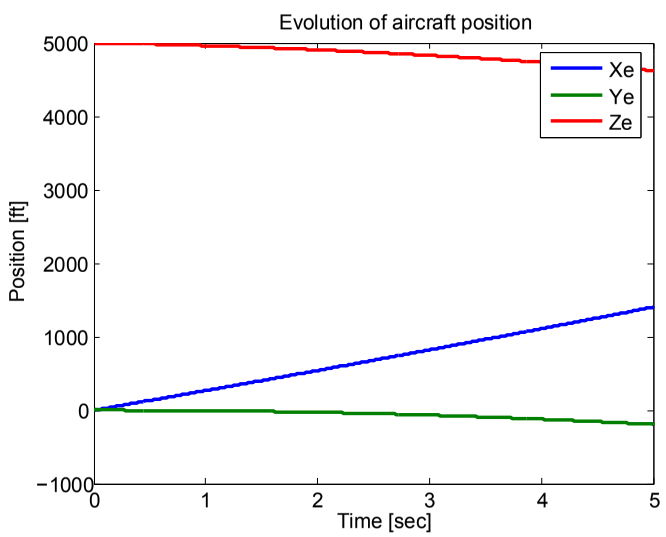

(a) Position

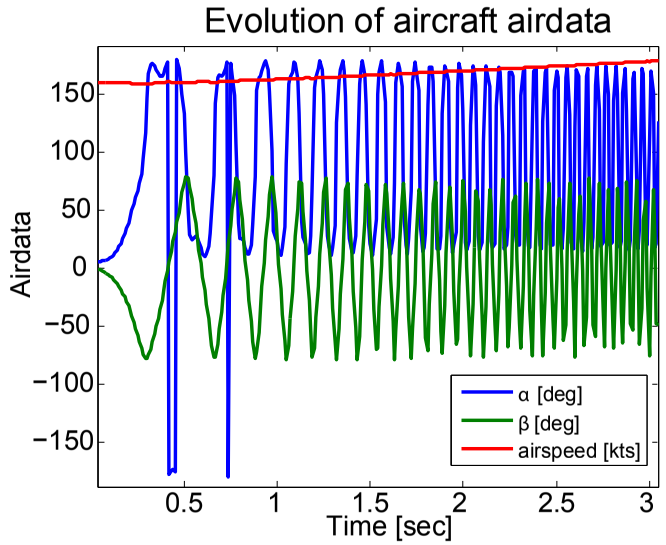

(b) Airdata

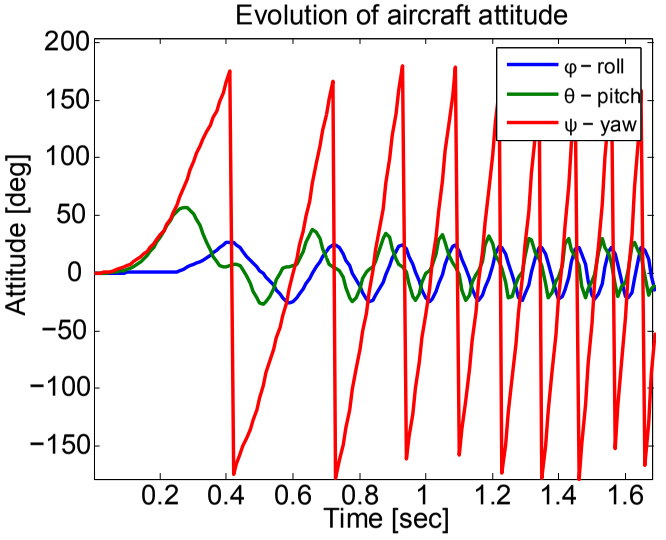

(c) Attitude

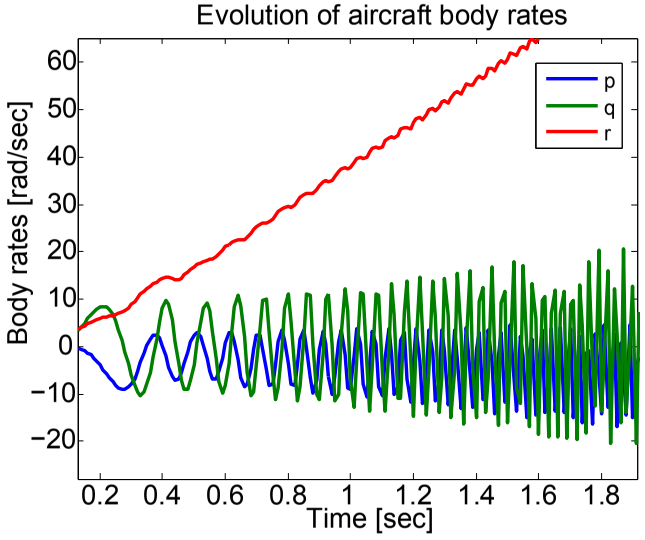

(d) Body Rates

Figure 8.20: Open loop simulation results.

Chapter 9

Conclusions and Recommendations for Future Works

9.1 Summary

In order to support the development of the AD-150 twin-tail tilt-duct VTOL UAV, two weeks of static and dynamic testing were conducted on a $3/10^{th}$ scale wind tunnel model. The model was designed and fabricated using wind tunnel modeling foam and a 3-axis CNC machine in house at American Dynamics Flight Systems. Next, two weeks of static and dynamic testing were conducted at the Glenn L. Martin Wind Tunnel. Comparative analysis was conducted between static wind tunnel and CFD data. Furthermore, system identification was performed on the dynamic runs to obtain the quasi-steady pitch and yaw stability derivatives. Finally, a basic simulation was constructed in the Simulink environment using the airframe wind tunnel data in conjunction with CFD generated performance of the ducts.

9.2 Limitations

Due to limitations in equipment and facilities, the following compromises and conclusions pertaining to the accuracy of the obtained model were made:

1. Wing-duct Interaction effects are absent in the data: prior research [16] sug-

gests that this interaction will increase inflow at the outboard portions of the wing, causing a reduced stall margin (or possibly eliminating it) that affects flaperon control effectiveness. Consequently, comprehensive models of this phenomenon would provide a higher fidelity flight dynamics model.

2. Complex ground effect based phenomenon was not modeled. Similarly, comprehensive models of this phenomenon would provide a higher fidelity flight dynamics model.

3. Reynolds distortions were introduced from the inability to use a sufficiently large wind tunnel model. The effect of these Reynolds distortions on the aerodynamic coefficients is unquantifiable due to a lack of full scale comparative data; however, discrepancies in the Reynolds number under an order of magnitude and away from the transition reigion are generally accepted to be sufficiently accurate.

9.3 Conclusions

The following specific conclusions have been drawn from the work reported in this thesis:

1. In the controls neutral static runs, the following observations were made about the longitudinal aerodynamics:

    - Lift shows a strong linear trend well into stall, correlating well with CFD analysis.

- Drag showed an expected quadratic trend; however, correlation with CFD started to break down near the point of stall ($\alpha > 10^o$).
- Pitch moment plots indicated the aircraft exhibits a precipitous moment stall, well before drop off in lift. Additionally, the slope of the trend indicates static instability. Correlation with CFD was found to be generally adequate below stall.

2. In the controls neutral static runs, the following observations were made about the lateral aerodynamics:
   - Side force trends are linear; however, correlation with CFD was generally poor.
   - Roll moment trends are nonlinear and indicate static stability. Correlation to CFD was found to be modest.
   - Yaw moment trends are nonlinear with static stability, but stability decreases near transition to stall. Correlation with CFD was found to be low.

3. In the static longitudinal control deflections runs the following observations were made with regard to the control power plots:
   - Flap deflections caused a linear increase in the lift slope with an associated increase in drag, but reduction in pitch moment. During symmetric tests ($\beta = 0^o$) coupling was found to be negligible.

- Elevator deflections induced a strong nonlinear change in pitch moment, lift, and drag. Coupling with the lateral axis increased nonlinearly with increasing magnitude of sideslip. Elevator stall occurred for deflections greater than $\delta_e = 15^o$.

4. In the static lateral control deflections runs the following observations were made with regard to the control power plots:

   - Aileron control plots indicate a linear relationship in roll response with no indications of drop off for deflections as high as $\delta_a = 45^o$. This is a beneficial characteristic considering roll control authority has historically been a problem [16] in the VZ-4.
   - Rudder control plots show a moderately linear trend between $\delta_r \pm 45^o$, with stall drop off occurring for larger deflection values. Strong yaw-roll coupling exists, but coupling with the longitudinal axis is minimal.

5. The ordinary least squares methodology was successfully used to determine the pitch and yaw rate damping parameters from wind tunnel experiments. The scatter in the parameter estimates were repeatable and consistent, with typical model fits as high as $R^2 = 96\%$. Validation of the results were done by way of comparison between static and dynamic estimates of the pitch and yaw stiffness terms. While a large discrepancy of 33-46% exists in the yaw, it was assumed that the error was attributed to the large amplitude oscillations that can invalidate a quasi-steady approximation. Note that this is an assumption as to the root cause in the difference of the coefficients - only precise testing

to determine what is happening in the boundary layer can prove or disprove the assumption. The pitch data, while plagued with collinearity, showed an average error of only 14%.

6. A simulation environment was sucessfully created in Simulink. Simple open loop output plots show rapid divergence, indicative of an unstable system with poles in the right half plane. This is consistent with the unstable pitch up moments generated by the airframe and ducts.

9.4 Future work

Based on the limitations outlined above, higher order modeling of wing-duct interactions and ground effect are recommended for future work. In addition, it is recommended that dynamic testing be performed to determine the quasi-steady roll moment damping stability derivative. These tests can be done by way of wind tunnel tests or CFD analysis. In the case of CFD analysis, validation with wind tunnel data should be made, when possible. The advantage of this method is that dynamic CFD analysis allows for the calculation of both aerodynamic force and moment stability derivatives with rate dependencies; whereas wind tunnel data only provides moment derivatives.

Full state linearization should be performed about a series of equilibrium trim points (steady wings level flight, turning flight, and hover). Effectiveness of the linearized models can then be determined by way of comparison to output results from the nonlinear simulation. Discrepancies between the two models will necessi-

tate the evaluation a new operating trim point, thereby introducing gain scheduling in the controls design. This accounts for the plant dynamic nonlinearities using a set of linear models. In addition, the linear time invariant (LTI) models provide a means of performing formal stability analysis − allowing for the eventual design and testing of an autopilot.

Appendix A

VZ-4 Stability Derivatives

The following stability and control derivatives, obtained from Ref [19], is for the Doak VZ-4. Finding this data was a nontrivial process that involved a bit of luck. As a result, the full data set is repeated here, along with the following note from the source:

> The data presented in this appendix have been collected from very diverse sources over a long period of time. In a few cases the original source of the data is now unclear. In many cases the data have been altered because of internal inconsistencies or physical improbabilities revealed by attempt to use them. For these reasons we wish to make it clear that the data are only nominally representative of the several aircraft configurations. In particular, the manufacturers of the aircraft cannot be held accountable for this information, nor would they be bound to concur in any conclusions with respect to their aircraft that might be derived from its use.

The following foot notes were included with the full stability data that follows.

[a] Normalized. (Note $M_{\delta_e}/Z_{\delta_e}$ changes with forward speed due to shift from jet to tail control. Values quoted are approximate.

[b] denotes approximated factors.

[c] Primed derivatives shown in parenthesis.

[d] (W = 3100 lb; I_x = 1990 slug-ft^2; I_z = 3450 slug-ft^2; α_w = 12 degrees)

[e] Condition of validity not satisfied.

Table A.1: VZ-4 Longitudinal Derivatives

U_o, ft/sec	0	58.5	73.0	126.6
X_u	-0.137	-0.130	-0.140	-0.210
X_w	0	-0.084	0.120	0.015
X_q	0	0	0	0
X_{δ_T}	0	0.342	0.442	0.914
X_{δ_e}	0	0	0	0
Z_u	0	-0.248	-0.285	-0.345
Z_w	-0.137	-0.526	-0.39	-0.718
Z_q	0	0	0	0
Z_{δ_T}	1.0	-0.940	-0.906	-0.406
Z_{δ_e}	1.08	1.00[a]	1.00[a]	1.00[a]
M_u	0.0136	0.0128	0.01205	0.0107
M_w	0	-0.032	-0.046	-0.082
$M_{\dot{w}}$	0	0	0	0
M_q	-0.0452	-0.858	-1.065	-1.839
M_{δ_T}	0	0	0	0
M_{δ_e}	1.0[o]	0.775	0.775[a]	0.775
W, lb	3100	3100	3100	3100
I, $slug - ft^2$	1790	1790	1790	1790

Table A.2: VZ-4 Longitudinal exact and approximate factors

		Speed, U_o (ft/sec)			
		0	58.5	73.0	126.6
Denominator	ω_{sp}	$1/T_{sp_1} = 0.137$	1.40 (1.49)	1.90 (1.94)	3.404 (3.24)
	ζ_{sp}	$1/T_{sp_2} = 0.824$	0.459 (0.464)	0.375 (0.374)	0.374 (0.406)
	ω_p	0.731	0.492 (0.457)	0.399 (0.395)	0.316 (0.315)
	ζ_p	-0.439	2.34 (0.378)	0.216 (0.275)	0.346 (0.375)
Stick	$1/T_{\theta_1}$	0.137	0.0757	$\omega = 0.287$	0.224
	$1/T_{\theta_2}$	0.137	0.539	$\zeta = 0.820$	0.598
	$1/T_{u_1}$	0.137 (0.137)	0.539	-150.8 (-151.5)	
	$1/T_{u_2}$	-	343.1 (325.0)	0.456 (0.454)	-1564.0 (-1570.0)
					0.6510 (0.650)
	$1/T_w$	$1/T_{sp_2}$	46.4 (45.8)	57.6 (56.5)	
	ω_w	$-\omega_p$	0.377 (0.360)	0.361 (0.370)	0.299 (0.300)
	ζ_w	$-\zeta_p$	0.168 (0.181)	0.191 (0.189)	0.349 (0.350)
Throttle	$1/T_{h_1}$		-4.095 (-4.71)	-3.66 (-4.32)	-6.81 (-7.71)
	$1/T_{h_2}$	[at $U_0 = 0$, $w = -\dot{h}$]	-0.218 (-0.215)	-0.1548 (-0.156)	0.0700 (0.060)
	$1/T_{h_3}$		5.302 (4.71)	5.017 (4.32)	8.79 (7.71)
	$1/T_{h_w}$		1.36 (1.35)	1.58 (1.62)	3.24 (3.37)
			0.550 (0.549)	0.495 (0.505)	0.326 (0.319)
	ω_{sp}	[at $U_0 = 0$, $w = -\dot{h}$]	-0.258 (-0.239)	-0.241 (-0.276)	-0.634 (-0.648)
	ζ_{sp}		0.288 (0.267)	0.264 (0.291)	0.0924 (0.930)
	$1/T_{\theta_1}$	-			
	$1/T_{\theta_2}$	-			
			-0.688 (-0.712)	-0.645 (-0.878)	-0.0982 (-0.0914)
	$1/T_u$	-	2.029 (1.98)	2.17 (1.84)	3.46 (3.60)
	ω_u	-	0.5676 (0.594)	0.427 (0.567)	0.383 (0.360)
	ζ_u	-			
	$1/T_h$	$= 1/T_{sp2}$	0.580	0.425	1.25
	ω_h	$= \omega p$	1.335	1.81	3.20
	ζ_h	$= \zeta p$	0.104	0.254	0.247

Table A.3: VZ-4 Lateral Derivatives

U_o, ft/sec	1.0	58.5	73.0	126.6
Y_v	-0.14	-0.2895	-0.2945	-0.333
Y_p	0	0	0	0
Y_r	0	0	0	0
Y_{δ_a}	0	-24.9	-26.8	-30.04
Y_{δ_r}	1.017	1.85	2.29	5.31
L_v	-0.0122 (-0.0123)	-0.0224 (-0.0236)	-0.0216 (-0.0241)	-0.0136 (-0.0158)
L_p	-0.271 (-0.273)	-0.455 (-0.467)	-0.497 (-0.508)	-0.67 (-0.677)
L_r	0 (0.0825)	1.75 (1.848)	0.911 (1.01)	0.659 (0.807)
L_{δ_a}	0.69 (0.696)	0.5013 (0.5055)	0.5208 (0.525)	0.972 (0.979)
L_{δ_r}	-0.185 (-0.119)	-0.141 (-0.0442)	-0.13 (-0.0102)	-0.15 (0.126)
N_v	0 (0.000885)	0.0081 (0.0098)	0.01 (0.0121)	0.0174 (0.0184)
N_p	0 (0.0197)	0.0605 (0.0940)	0.0535 (0.0900)	0.0109 (0.0596)
N_r	-0.656 (-0.662)	-0.655 (-0.788)	0.723 (-0.796)	-1.13 (-1.19)
N_{δ_a}	0 (-0.0500)	0.003 (-0.0333)	0.0041 (-0.0336)	0.0133 (-0.0571)
N_{δ_r}	-0.539(-0.531)	-0.78 (-0.777)	-0.962 (-0.961)	-2.204 (-2.213)
I_{xz}/I_x	-0.1246	-0.1246	-0.1246	-0.1246
I_{xz}/I_z	-0.07188	-0.07188	-0.07188	-0.07188

Table A.4: VZ-4 Lateral exact and approximate factors

		Speed, U_o (ft/sec)			
		0	58.5	73.0	126.6
Denominator	ω_d	0.699 (0.704)	0.866 (0.758)	0.914 (0.92)	1.59 (1.54)
	ζ_d	-0.347 (-0.355)	0.1655 (0.035)	0.205 (0.21)	0.421 (0.436)
	$1/T_r$	0.888 (0.914)	1.242 (1.477)	0.957 (1.023)	0.796 (0.804)
	$1/T_s$	0.653 (0.662)	0.0159 (0.0141)	0.265 (0.190)	0.0620 (0.0583)
Aileron/Differential Thrust	$1/T_{\phi_1}$	0.14 (0.14)	0.407 (0.464)	$\omega_\phi = 1.13$ ($1/T_{\phi_1} = 1.269$)	$\omega_\phi = 1.65$ (1.70)
	$1/T_{\phi_2}$	0.6564 (0.14)	1.712 (1.764)	$\zeta_\phi = 0.968$ ($1/T_{\phi_1} = 1.161$)	$\zeta_\phi = 0.595$(0.595)
	$1/T_{r_1}$	0 (0)	-0.646 (-0.671)	-0.606 (-0.614)	-0.7188 (-0.70)
	$1/T_{r_2}$	0.140 (0.14)	0.982 (0.979)	1.02 (0.886)	1.51 (1.42)
	$1/T_{r_3}$	0 (0)	6.329 (7.32)	8.24 (9.25)	9.01 (9.85)
	$1/T_{p_1}$	0.657	-0.611	-0.577	0.754
	$1/T_{p_2}$	447.0	0.595	0.846	1.35
	$1/T_{p_3}$		1.192	0.944	0.5911
Rudder tail jet	$1/T_{\phi_1}$	0.267 (0.368)[a]	1.03 (1.054)	1.90 (1.98)	2.39 (2.71)
	$1/T_{\phi_2}$	1.008 (0.775)[a]	33.5 (33.0)	99.5 (94.0)	-15.73 (-14.2)
	$1/T_{r_1}$	0.886 (0.919)	1.17 (1.185)	1.188 (1.191)	1.15 (1.187)
	ω_r	0.674 (0.699)	0.802 (0.804)	0.793 (0.792)	0.642 (0.661)
	ζ_r	-0.348 (-0.352)	-0.274 (-0.303)	-0.259 (-0.252)	-0.147 (-0.1322)
	$1/T_{v_1}$	-1.75	-0.793 (0.79)	-0.452 (-0.447)	-0.205 (-0.289)
	$1/T_{v_2}$	0.994	1.27 (1.25)	0.968 (0.954)	0.896 (-0.979)
	$1/T_{v_2}$	2.22	25.47 (25.96)	31.43 (31.9)	53.93 (53.97)

Appendix B

Test Matrix

This appendix contains the compelte test matrix used to obtain the static stability and controls plots in Chapter 5.

Table A-1: Wind Tunnel Test Matrix

Run	Variation	V mph	θ (Pitch)	ψ (Heading)	Configuration	Control Surface	Type	Status	Notes
902	902	-	0^o	ψ_1	UPRIGHT	Neutral	Variation	OK	
903	903	-	θ_3	0^o	UPRIGHT	Neutral	Variation	Bad Run	
904	904	-	θ_3	0^o	UPRIGHT	Neutral	Variation	OK	
1	902	80	0^o	ψ_1	UPRIGHT	Neutral	Aero Zero	OK	
905	905	-	θ_6	0^o	INV+IMAGE IN	Neutral	Variation	Bad Run	
906	906	-	θ_6	-14^o	INV+IMAGE IN	Neutral	Variation	Bad Run	
907	907	-	θ_6	14^o	INV+IMAGE IN	Neutral	Variation	Bad Run	
908	908	-	θ_6	-14^o	INV+IMAGE IN	Neutral	Variation	OK	
909	909	-	θ_6	0^o	INV+IMAGE IN	Neutral	Variation	OK	
910	910	-	θ_6	14^o	INV+IMAGE IN	Neutral	Variation	OK	
2	908	80	θ_5	-14^o	INV+IMAGE IN	Neutral	Variation	OK	
3	909	80	θ_5	0^o	INV+IMAGE IN	Neutral	Variation	OK	
4	910	80	θ_5	14^o	INV+IMAGE IN	Neutral	Variation	OK	
5	908	80	θ_5	-14^o	INV	Neutral	Variation	Bad Run	no power to rotating post
6	908	80	θ_5	-14^o	INV	Neutral	Variation	OK	
7	909	80	θ_5	0^o	INV	Neutral	Variation	OK	
8	910	80	θ_5	14^o	INV	Neutral	Variation	OK	
911	911	-	θ_7	0^o	UPRIGHT	Neutral	Variation	Bad Run	shevitz was not on
912	912	-	θ_7	0^o	UPRIGHT	Neutral	Variation	OK	
913	913	-	θ_7	2^o	UPRIGHT	Neutral	Variation	OK	
914	914	-	θ_7	4^o	UPRIGHT	Neutral	Variation	OK	
915	915	-	θ_7	6^o	UPRIGHT	Neutral	Variation	OK	
916	916	-	θ_7	7^o	UPRIGHT	Neutral	Variation	OK	
917	917	-	θ_7	13^o	UPRIGHT	Neutral	Variation	OK	
9	912	50	θ_7	0^o	UPRIGHT	Neutral	Static	Bad Run	didn't change pitch file
10	912	50	θ_2	0^o	UPRIGHT	Neutral	Static	OK	
11	913	50	θ_2	2^o	UPRIGHT	Neutral	Static	OK	
12	914	50	θ_2	4^o	UPRIGHT	Neutral	Static	OK	
13	915	50	θ_2	6^o	UPRIGHT	Neutral	Static	OK	
14	916	50	θ_2	9^o	UPRIGHT	Neutral	Static	OK	

Table A-1: Wind Tunnel Test Matrix - Cont'd

Run	Variation	V mph	θ (Pitch)	ψ (Heading)	Configuration	Control Surface	Type	Status	Notes
15	917	50	θ_2	13^o	UPRIGHT	Neutral	Static	OK	
16	912	80	θ_2	0^o	UPRIGHT	Neutral	Static	OK	
17	913	80	θ_2	2^o	UPRIGHT	Neutral	Static	OK	
18	914	80	θ_2	4^o	UPRIGHT	Neutral	Static	OK	
19	915	80	θ_2	6^o	UPRIGHT	Neutral	Static	OK	
20	916	80	θ_2	9^o	UPRIGHT	Neutral	Static	OK	
21	917	80	θ_2	13^o	UPRIGHT	Neutral	Static	OK	
22	912	110	θ_2	0^o	UPRIGHT	Neutral	Static	OK	
23	913	110	θ_2	2^o	UPRIGHT	Neutral	Static	OK	
24	914	110	θ_2	4^o	UPRIGHT	Neutral	Static	OK	
25	915	110	θ_2	6^o	UPRIGHT	Neutral	Static	OK	
26	916	110	θ_2	9^o	UPRIGHT	Neutral	Static	OK	
27	917	110	θ_2	13^o	UPRIGHT	Neutral	Static	OK	
28	912	160	θ_2	0^o	UPRIGHT	Neutral	Static	OK	
29	913	160	θ_2	2^o	UPRIGHT	Neutral	Static	OK	
30	914	160	θ_2	4^o	UPRIGHT	Neutral	Static	OK	
31	915	160	θ_2	6^o	UPRIGHT	Neutral	Static	OK	
32	916	160	θ_2	9^o	UPRIGHT	Neutral	Static	OK	
33	917	160	θ_2	13^o	UPRIGHT	Neutral	Static	OK	
34	912	110	θ_2	0^o	UPRIGHT	Elevator 45^o	Static	Bad Run	drag error
35	912	110	θ_2	0^o	UPRIGHT	Elevator 45^o	Static	OK	
36	915	110	θ_2	6^o	UPRIGHT	Elevator 45^o	Static	OK	
37	917	110	θ_2	13^o	UPRIGHT	Elevator 45^o	Static	OK	
918	918	-	0^o	ψ_3	UPRIGHT	Rudder 45^o	Variation	OK	
919	919	-	6^o	ψ_3	UPRIGHT	Rudder 45^o	Variation	OK	
920	920	-	11^o	ψ_3	UPRIGHT	Rudder 45^o	Variation	OK	
38	918	110	0^o	ψ_3	UPRIGHT	Rudder 45^o	Static	OK	
39	919	110	6^o	ψ_3	UPRIGHT	Rudder 45^o	Static	OK	
40	920	110	11^o	ψ_3	UPRIGHT	Rudder 45^o	Static	OK	
41	918	110	θ_2	0^o	UPRIGHT	Elevator -45^o	Static	Bad Run	variation not changed

Table A-1: Wind Tunnel Test Matrix - Cont'd

Run	Variation	V mph	θ (Pitch)	ψ (Heading)	Configuration	Control Surface	Type	Status	Notes
42	912	110	θ_2	0^o	UPRIGHT	Elevator -45^o	Static	OK	
43	915	110	θ_2	6^o	UPRIGHT	Elevator -45^o	Static	OK	
44	917	110	θ_2	13^o	UPRIGHT	Elevator -45^o	Static	OK	
45	918	110	0^o	ψ_3	UPRIGHT	Rudder -45^o	Static	OK	
46	919	110	6^o	ψ_3	UPRIGHT	Rudder -45^o	Static	OK	
47	920	110	11^o	ψ_3	UPRIGHT	Rudder -45^o	Static	OK	
48	912	110	θ_2	0^o	UPRIGHT	Elevator 30^o	Static	OK	
49	915	110	θ_2	6^o	UPRIGHT	Elevator 30^o	Static	OK	
50	917	110	θ_2	13^o	UPRIGHT	Elevator 30^o	Static	OK	
51	918	110	0^o	ψ_3	UPRIGHT	Rudder 30	Static	OK	
52	919	110	6^o	ψ_3	UPRIGHT	Rudder 30	Static	OK	
53	920	110	11^o	ψ_3	UPRIGHT	Rudder 30	Static	OK	
54	912	110	θ_2	0^o	UPRIGHT	Elevator -30^o	Static	OK	
55	915	110	θ_2	6^o	UPRIGHT	Elevator -30^o	Static	OK	
56	917	110	θ_2	13^o	UPRIGHT	Elevator -30^o	Static	OK	
57	918	110	0^o	ψ_3	UPRIGHT	Rudder -30^o	Static	OK	
58	919	110	0^o	ψ_3	UPRIGHT	Rudder -30^o	Static	Bad Run	pitch angle not changed
59	919	110	6^o	ψ_3	UPRIGHT	Rudder -30^o	Static	OK	
60	920	110	11^o	ψ_3	UPRIGHT	Rudder -30^o	Static	OK	
61	912	110	θ_2	0^o	UPRIGHT	Elevator 15^o	Static	OK	
62	915	110	θ_2	6^o	UPRIGHT	Elevator 15^o	Static	OK	
63	917	110	θ_2	13^o	UPRIGHT	Elevator 15^o	Static	OK	
64	918	110	0^o	ψ_3	UPRIGHT	Rudder 15^o	Static	OK	
65	919	110	6^o	ψ_3	UPRIGHT	Rudder 15^o	Static	OK	
66	920	110	11^o	ψ_3	UPRIGHT	Rudder 15^o	Static	OK	
67	912	110	θ_2	0^o	UPRIGHT	Elevator -15^o	Static	OK	
68	915	110	θ_2	6^o	UPRIGHT	Elevator -15^o	Static	OK	
69	917	110	θ_2	13^o	UPRIGHT	Elevator -15^o	Static	OK	
70	918	110	0^o	ψ_3	UPRIGHT	Rudder -15^o	Static	OK	
71	919	110	6^o	ψ_3	UPRIGHT	Rudder -15^o	Static	OK	

Table A-1: Wind Tunnel Test Matrix - Cont'd

Run	Variation	V mph	θ (Pitch)	ψ (Heading)	Configuration	Control Surface	Type	Status	Notes
72	920	110	11^o	ψ_3	UPRIGHT	Rudder -15^o	Static	OK	
73	912	110	θ_2	0^o	UPRIGHT	Aileron 45^o	Static	OK	
74	919	110	6^o	ψ_3	UPRIGHT	Aileron 45^o	Static	OK	
75	912	110	θ_2	0^o	UPRIGHT	Aileron 30^o	Static	OK	
76	919	110	6^o	ψ_3	UPRIGHT	Aileron 30^o	Static	OK	
77	912	110	θ_2	0^o	UPRIGHT	Aileron 15^o	Static	OK	
78	919	110	6^o	ψ_3	UPRIGHT	Aileron 15^o	Static	Bad Run	Data taken with no wind
79	919	110	6^o	ψ_3	UPRIGHT	Aileron 15^o	Static	OK	repeat of run 78
80	912	110	θ_2	0^o	UPRIGHT	Flap 15^o	Static	OK	
81	912	110	θ_2	0^o	UPRIGHT	Flap 30^o	Static	OK	
82	912	110	θ_2	0^o	UPRIGHT	Flap 45^o	Static	OK	
83	-	80	-	-	UPRIGHT	Neutral	Dynamic (Yaw)	OK	
84	-	80	-	-	UPRIGHT	Neutral	Dynamic (Yaw)	OK	
85	-	80	-	-	UPRIGHT	Neutral	Dynamic (Yaw)	OK	
86	-	80	-	-	UPRIGHT	Neutral	Dynamic (Yaw)	OK	
87	-	90	-	-	UPRIGHT	Neutral	Dynamic (Yaw)	OK	
88	-	90	-	-	UPRIGHT	Neutral	Dynamic (Yaw)	OK	
89	-	90	-	-	UPRIGHT	Neutral	Dynamic (Yaw)	OK	
90	-	90	-	-	UPRIGHT	Neutral	Dynamic (Yaw)	OK	
91	-	100	-	-	UPRIGHT	Neutral	Dynamic (Yaw)	OK	
92	-	100	-	-	UPRIGHT	Neutral	Dynamic (Yaw)	OK	
93	-	100	-	-	UPRIGHT	Neutral	Dynamic (Yaw)	OK	
94	-	100	-	-	UPRIGHT	Neutral	Dynamic (Yaw)	OK	
95	-	110	-	-	UPRIGHT	Neutral	Dynamic (Yaw)	OK	
96	-	110	-	-	UPRIGHT	Neutral	Dynamic (Yaw)	OK	
97	-	110	-	-	UPRIGHT	Neutral	Dynamic (Yaw)	OK	
98	-	110	-	-	UPRIGHT	Neutral	Dynamic (Yaw)	OK	
99	-	120	-	-	UPRIGHT	Neutral	Dynamic (Yaw)	OK	
100	-	120	-	-	UPRIGHT	Neutral	Dynamic (Yaw)	OK	
101	-	120	-	-	UPRIGHT	Neutral	Dynamic (Yaw)	OK	

Table A-1: Wind Tunnel Test Matrix - Cont'd

Run	Variation	V mph	θ (Pitch)	ψ (Heading)	Configuration	Control Surface	Type	Status	Notes
102	-	120	-	-	UPRIGHT	Neutral	Dynamic (Yaw)	OK	
103	-	80	-	-	UPRIGHT	Rudder 15^o	Dynamic (Yaw)	OK	
104	-	80	-	-	UPRIGHT	Rudder 15^o	Dynamic (Yaw)	OK	
105	-	80	-	-	UPRIGHT	Rudder 15^o	Dynamic (Yaw)	OK	
106	-	80	-	-	UPRIGHT	Rudder 15^o	Dynamic (Yaw)	OK	
107	-	80	-	-	UPRIGHT	Rudder 15^o	Dynamic (Yaw)	OK	
108	-	90	-	-	UPRIGHT	Rudder 15^o	Dynamic (Yaw)	OK	
109	-	90	-	-	UPRIGHT	Rudder 15^o	Dynamic (Yaw)	OK	
110	-	90	-	-	UPRIGHT	Rudder 15^o	Dynamic (Yaw)	OK	
111	-	90	-	-	UPRIGHT	Rudder 15^o	Dynamic (Yaw)	OK	
112	-	100	-	-	UPRIGHT	Rudder 15^o	Dynamic (Yaw)	OK	
113	-	100	-	-	UPRIGHT	Rudder 15^o	Dynamic (Yaw)	OK	
114	-	100	-	-	UPRIGHT	Rudder 15^o	Dynamic (Yaw)	OK	
115	-	100	-	-	UPRIGHT	Rudder 15^o	Dynamic (Yaw)	OK	
116	-	110	-	-	UPRIGHT	Rudder 15^o	Dynamic (Yaw)	OK	
117	-	110	-	-	UPRIGHT	Rudder 15^o	Dynamic (Yaw)	OK	
118	-	110	-	-	UPRIGHT	Rudder 15^o	Dynamic (Yaw)	OK	
119	-	110	-	-	UPRIGHT	Rudder 15^o	Dynamic (Yaw)	OK	
120	-	120	-	-	UPRIGHT	Rudder 15^o	Dynamic (Yaw)	OK	
121	-	120	-	-	UPRIGHT	Rudder 15^o	Dynamic (Yaw)	OK	
122	-	120	-	-	UPRIGHT	Rudder 15^o	Dynamic (Yaw)	OK	
123	-	120	-	-	UPRIGHT	Rudder 15^o	Dynamic (Yaw)	OK	
124	-	50	-	-	UPRIGHT	Neutral	Dynamic (Pitch)	OK	Equilibrium Runs
125	-	60	-	-	UPRIGHT	Neutral	Dynamic (Pitch)	OK	Equilibrium Runs
126	-	70	-	-	UPRIGHT	Neutral	Dynamic (Pitch)	OK	Equilibrium Runs
127	-	80	-	-	UPRIGHT	Neutral	Dynamic (Pitch)	OK	Equilibrium Runs
128	-	90	-	-	UPRIGHT	Neutral	Dynamic (Pitch)	OK	Equilibrium Runs
129	-	70	-	-	UPRIGHT	Neutral	Dynamic (Pitch)	OK	Perturbations Runs
130	-	70	-	-	UPRIGHT	Neutral	Dynamic (Pitch)	OK	Perturbations Runs
131	-	70	-	-	UPRIGHT	Neutral	Dynamic (Pitch)	OK	Perturbations Runs
132	-	70	-	-	UPRIGHT	Neutral	Dynamic (Pitch)	OK	Perturbations Runs

Table A-1: Wind Tunnel Test Matrix - Cont'd

Run	Variation	V mph	θ (Pitch)	ψ (Heading)	Configuration	Control Surface	Type	Status	Notes
133	-	80	-	-	UPRIGHT	Neutral	Dynamic (Pitch)	OK	Perturbations Runs
134	-	80	-	-	UPRIGHT	Neutral	Dynamic (Pitch)	OK	Perturbations Runs
135	-	80	-	-	UPRIGHT	Neutral	Dynamic (Pitch)	OK	Perturbations Runs
136	-	80	-	-	UPRIGHT	Neutral	Dynamic (Pitch)	OK	Perturbations Runs
137	-	90	-	-	UPRIGHT	Neutral	Dynamic (Pitch)	OK	Perturbations Runs
138	-	90	-	-	UPRIGHT	Neutral	Dynamic (Pitch)	OK	Perturbations Runs
139	-	90	-	-	UPRIGHT	Neutral	Dynamic (Pitch)	OK	Perturbations Runs
140	-	90	-	-	UPRIGHT	Neutral	Dynamic (Pitch)	OK	Perturbations Runs
141	-	0	-	-	UPRIGHT	Neutral	Dynamic (Pitch)	OK	No Wind
142	-	80	-	-	UPRIGHT	Neutral	Dynamic (Pitch)	OK	$\theta_0 = -4.9^o$
143	-	80	-	-	UPRIGHT	Neutral	Dynamic (Pitch)	OK	$\theta_0 = -4.9^o$
144	-	80	-	-	UPRIGHT	Neutral	Dynamic (Pitch)	OK	$\theta_0 = -4.9^o$
145	-	80	-	-	UPRIGHT	Neutral	Dynamic (Pitch)	OK	$\theta_0 = -4.9^o$
146	-	90	-	-	UPRIGHT	Neutral	Dynamic (Pitch)	OK	$\theta_0 = -4.9^o$
147	-	90	-	-	UPRIGHT	Neutral	Dynamic (Pitch)	OK	$\theta_0 = -4.9^o$
148	-	90	-	-	UPRIGHT	Neutral	Dynamic (Pitch)	OK	$\theta_0 = -4.9^o$
149	-	90	-	-	UPRIGHT	Neutral	Dynamic (Pitch)	OK	$\theta_0 = -4.9^o$
150	-	0	-	-	UPRIGHT	Neutral	Dynamic (Pitch)	OK	No Wind $\theta_0 = -4.9^o$
151	-	0	-	-	UPRIGHT	Neutral	Dynamic (Pitch)	OK	No Wind $\theta_0 = -4.9^o$
152	-	0	-	-	UPRIGHT	Neutral	Dynamic (Pitch)	OK	No Wind $\theta_0 = -4.9^o$
153	-	0	-	-	UPRIGHT	Neutral	Dynamic (Pitch)	OK	No Wind $\theta_0 = -4.9^o$
154	-	0	-	-	UPRIGHT	Neutral	Dynamic (Pitch)	OK	No Wind $\theta_0 = 0^o$
155	-	0	-	-	UPRIGHT	Neutral	Dynamic (Pitch)	OK	No Wind $\theta_0 = 0^o$
156	-	0	-	-	UPRIGHT	Neutral	Dynamic (Pitch)	OK	No Wind $\theta_0 = 0^o$
157	-	0	-	-	UPRIGHT	Neutral	Dynamic (Pitch)	OK	No Wind $\theta_0 = 0^o$

Table A-2: Variable Definitions

θ (Pitch)	ψ (Heading)
$\theta_1 = -5^o, -4^o, -2^o, 0^o, 2^o, 4^o, 6^o, 8^o, 10^o, 11^o, 12^o, 15^o, 16^o$	$\psi_1 = -2, -1.5, -1, -.5, 0, .5, 1, 1.5, 2$
$\theta_2 = -5^o, -4^o, -2^o, 0^o, 4^o, 6^o, 10^o, 12^o, 16^o$	$\psi_2 = -16^o, 0^o, 16^o$
$\theta_3 = -2^o, -1.5^o, -1^o, -0.5^o, 0^o, 0.5^o, 1^o, 1.5^o, 2^o$	$\psi_3 = -13^o, -9^o, -6^o, -4^o, -2^o, 0^o, 2^o, 4^o, 6^o, 9^o, 13^o$
$\theta_4 = -16^o, 4^o, 16^o$	
$\theta_5 = -16^o, -15^o, -12^o, -11^o, -10^o, -8^o - 6^o, -4^o, -2^o, 0^o, 2^o, 4^o, 5^o$	
θ_6 = VARIATION	
θ_7 = VARIATION	

Appendix C

Sensor Specifications

Table C-1: Jewell Instruments LSO inclonometer

Input Range	$\pm$ 30
Resolution and Threshold	1μ rad
Nonlinearity (% FRO) maximum	0.02
Natural Frequency (Hz) nominal	20.0
Bandwidth [-3db] (Hz)	20.0

Table C-2: Microstrain 3DM-GX1 Specifications

Orientation Range	360^o full scale (FS)
Orientation Accuracy	2^o (dynamic test conditions)
Gyros	300^o/sec FS
Gyro Nonlinearity	0.2%
Gyro Bias Stability	0.7^o/sec
Magnetometers	1.2 Gauss FS
Magnetometer Nonlinearity	0.4%
Magnetometer Bias Stability	0.010 Gauss
Orientation Resolution	$< 0.1^o$ minimum
Digital Output Rates	100 Hz
Operating Temperature	-40 to +70 C

Appendix D

CFD Test Matrix

A complete test matrix of the CFD propulsion ducts is given in Table D-1. The data clearly shows that variation in freestream angle γ and RPM are not consistent across all airspeeds, posing a problem because the Simulink lookup function block requires a consistent set of indices. Therefore, the test matrix was modified such that all combinations of airspeed and RPM had a corresponding freestream vector of $\gamma = \{0^o, 5^o, 10^o, 15^o, 30^o, 45^o, 60^o, 75^o, 90^o\}$ and RPM vector of RPM $= \{2500, 3000, 3500, 4000, 4500, 5000, 5500, 6000, 6500\}$. All reported data is in the local duct body frame[1]. In cases of missing data, end point saturation was used: this is simply an assumption. The missing data can later be replaced with new CFD runs, or extrapolated depending on the linearity of the data. The correction process is as follows:

0 mph

The 0 mph runs are set to constant force and moment values for all freestream angles. That is a byproduct of the wind having zero magnitude, and represents the hover on station flight condition.

[1]The forces are: normal, axial and side. Meanwhile, the moments are pitch, roll and yaw

10 mph

For the 10mph runs, notice that lowest fan speed is 4500 RPM; therefore, forces and moments for fan speed between 2500-4000RPM were assumed constant and equal to the 4500 RPM results. In addition, the freestream angle variation was $\gamma = 0 - 15^o$; therefore, the force and moments for $\gamma = 30 - 90^o$ were assumed to be constant and equal to the $\gamma = 15^o$ case.

25-80 mph

For the 20-80 mph runs, the 2500-4000 RPM fan speeds were only calculated at $\gamma = 0^o$; therefore, forces and moments for $\gamma = 5 - 90^0$ were assumed constant and equal to the $\gamma = 0^o$ cases. For the 4500-6500 RPM fan speeds, the freestream angles $\gamma = 5 - 10^o$ were added by linearly interpolating between $\gamma = 0, 15^o$.

110-200 mph

For the 110-200 mph runs, the 2500-4000 RPM fan speeds were only calculated at $\gamma = 0^o$; therefore, forces and moments for $\gamma = 5 - 90^0$ were assumed constant and equal to the $\gamma = 0^o$ cases. For the 4500-6500 RPM fan speeds, the freestream angles $\gamma = 5 - 10^o$ were added by linearly interpolating between $\gamma = 0, 15^o$. The 4500 RPM runs had to be added by interpolating between the 4000 RPM and 5000 RPM data for $\gamma = 0^o$ and assuming the forces and moments are constant for across all freestream angles. Finally, for the 5000-6500 RPM fan speeds, the freestream angles $\gamma = 5 - 10^o$ were added by linearly interpolating between $\gamma = 0, 15^o$.

Table D-1: CFD Test Matrix, Ducts

Sim. Run No.	RPM	$[V_D^D]$, mph	γ, deg
335	2500	0	0
328	3000	0	0
314	3500	0	0
321	4000	0	0
107	4500	0	0
108	5000	0	0
109	5500	0	0
100	6000	0	0
110	6500	0	0
294	4500	10	0
295	4500	10	5
296	4500	10	10
297	4500	10	15
298	5000	10	0
299	5000	10	5
300	5000	10	10
301	5000	10	15
302	5500	10	0
303	5500	10	5
304	5500	10	10
305	5500	10	15
306	6000	10	0
307	6000	10	5
308	6000	10	10
309	6000	10	15
310	6500	10	0
311	6500	10	5
312	6500	10	10
313	6500	10	15
336	2500	25	0
329	3000	25	0
315	3500	25	0
322	4000	25	0
273	4500	25	0
274	4500	25	15
275	4500	25	30
276	4500	25	45
277	4500	25	60
278	4500	25	75

Table D-1: CFD Test Matrix, Cont'd.

Sim. Run No.	RPM	$[V_D^D]$, mph	γ, deg
279	4500	25	90
147	5000	25	0
148	5000	25	15
149	5000	25	30
150	5000	25	45
151	5000	25	60
152	5000	25	75
153	5000	25	90
189	5500	25	0
190	5500	25	15
191	5500	25	30
192	5500	25	45
193	5500	25	60
194	5500	25	75
195	5500	25	90
101	6000	25	0
111	6000	25	15
112	6000	25	30
113	6000	25	45
114	6000	25	60
115	6000	25	75
116	6000	25	90
231	6500	25	0
232	6500	25	15
233	6500	25	30
234	6500	25	45
235	6500	25	60
236	6500	25	75
237	6500	25	90
337	2500	50	0
330	3000	50	0
316	3500	50	0
323	4000	50	0
280	4500	50	0
281	4500	50	15
282	4500	50	30
283	4500	50	45
284	4500	50	60
285	4500	50	75
286	4500	50	90
154	5000	50	0

Table D-1: CFD Test Matrix, Cont'd.

Sim. Run No.	RPM	$[V_D^D]$, mph	γ, deg
155	5000	50	15
156	5000	50	30
157	5000	50	45
158	5000	50	60
159	5000	50	75
160	5000	50	90
196	5500	50	0
197	5500	50	15
198	5500	50	30
199	5500	50	45
200	5500	50	60
201	5500	50	75
202	5500	50	90
102	6000	50	0
117	6000	50	15
118	6000	50	30
119	6000	50	45
120	6000	50	60
121	6000	50	75
122	6000	50	90
238	6500	50	0
239	6500	50	15
240	6500	50	30
241	6500	50	45
242	6500	50	60
243	6500	50	75
244	6500	50	90
338	2500	80	0
331	3000	80	0
317	3500	80	0
324	4000	80	0
287	4500	80	0
288	4500	80	15
289	4500	80	30
290	4500	80	45
291	4500	80	60
292	4500	80	75
293	4500	80	90
161	5000	80	0
162	5000	80	15
163	5000	80	30

Table D-1: CFD Test Matrix, Cont'd.

Sim. Run No.	RPM	$[V_D^D]$, mph	γ, deg
164	5000	80	45
165	5000	80	60
166	5000	80	75
167	5000	80	90
203	5500	80	0
204	5500	80	15
205	5500	80	30
206	5500	80	45
207	5500	80	60
208	5500	80	75
209	5500	80	90
103	6000	80	0
123	6000	80	15
124	6000	80	30
125	6000	80	45
126	6000	80	60
127	6000	80	75
128	6000	80	90
245	6500	80	0
246	6500	80	15
247	6500	80	30
248	6500	80	45
249	6500	80	60
250	6500	80	75
251	6500	80	90
339	2500	110	0
332	3000	110	0
318	3500	110	0
325	4000	110	0
168	5000	110	0
169	5000	110	15
170	5000	110	30
171	5000	110	45
172	5000	110	60
173	5000	110	75
174	5000	110	90
210	5500	110	0
211	5500	110	15
212	5500	110	30
213	5500	110	45

Table D-1: CFD Test Matrix, Cont'd.

Sim. Run No.	RPM	$[V_D^D]$, mph	γ, deg
214	5500	110	60
215	5500	110	75
216	5500	110	90
104	6000	110	0
129	6000	110	15
130	6000	110	30
131	6000	110	45
132	6000	110	60
133	6000	110	75
134	6000	110	90
252	6500	110	0
253	6500	110	15
254	6500	110	30
255	6500	110	45
256	6500	110	60
257	6500	110	75
258	6500	110	90
340	2500	160	0
333	3000	160	0
319	3500	160	0
326	4000	160	0
175	5000	160	0
176	5000	160	15
177	5000	160	30
178	5000	160	45
179	5000	160	60
180	5000	160	75
181	5000	160	90
217	5500	160	0
218	5500	160	15
219	5500	160	30
220	5500	160	45
221	5500	160	60
222	5500	160	75
223	5500	160	90
105	6000	160	0
135	6000	160	15
136	6000	160	30
137	6000	160	45
138	6000	160	60

Table D-1: CFD Test Matrix, Cont'd.

Sim. Run No.	RPM	$[V_D^D]$, mph	γ, deg
139	6000	160	75
140	6000	160	90
259	6500	160	0
260	6500	160	15
261	6500	160	30
262	6500	160	45
263	6500	160	60
264	6500	160	75
265	6500	160	90
341	2500	200	0
334	3000	200	0
320	3500	200	0
327	4000	200	0
182	5000	200	0
183	5000	200	15
184	5000	200	30
185	5000	200	45
186	5000	200	60
187	5000	200	75
188	5000	200	90
224	5500	200	0
225	5500	200	15
226	5500	200	30
227	5500	200	45
228	5500	200	60
229	5500	200	75
230	5500	200	90
106	6000	200	0
141	6000	200	15
142	6000	200	30
143	6000	200	45
144	6000	200	60
145	6000	200	75
146	6000	200	90
266	6500	200	0
267	6500	200	15
268	6500	200	30
269	6500	200	45
270	6500	200	60
271	6500	200	75
272	6500	200	90

Bibliography

[1] Singer, P.W., *Wired For War*, Penguin Books, New York, NY, 2009.

[2] Williams, K.W., "Human Factors Implications of Unmanned Aircraft Accidents: Flight-Control Problems," DOT/FAA/AM-06/8, Federal Aviation Administration, Oklahoma City, OK, 2006.

[3] Pineda, S.X., "MQ-8B Fire Scout Vertical Unmanned System," Northrop Grumman Facts Sheet Release.

[4] Leishman, J.G., *Principles of Helicopter Aerodynamics*, 2nd ed., Cambridge Aerospace Series. Cambridge University Press, New York, NY, 2008.

[5] Arents, D.N., "An Assessment of the Hover Performance of the XH-59A Advancing Blade Concept Demonstration Helicopter",USAAMRDL-TN-25, U.S. Army Air Mobility Research and Development Laboratory, Fort Eustis, Va. 23604, May 1977.

[6] Nelson, N.E., "The Ducted Fan in VTOL Aircraft Design," Journal of the American Helicopter Society, Vol. 4, No. 1, Jan 1959, pp. 53-56.

[7] Goodson, K.W, and Grunwald, J.J., "Aerodynamic Characteristics of a Powered Semispan Tilting-Shrouded-Propeller VTOL Model in Hovering and Transitional Flight," NASA TN D-981, Langley Research Center, Langley Field, Va., 1962.

[8] Grunwald, K.J., and Goodson, K.W., "Aerodynamic Loads on an Isolated Shrouded-Propeller Configuration for Angles of Attack From -10^o to 110^o," NASA TN D-995, Langley Research Center, Langley Field, Va., 1962.

[9] Grunwald, K.J., and Goodson, K.W., "Division of Aerodynamic Loads on a Semispan Tilting-Ducted-Propeller Model in Hovering and Transition Flight," NASA TN D-1257, Langley Research Center, Langley Field, Va., 1962.

[10] Grunwald, K.J., and Goodson, K.W., "Aerodynamic Loads on an Isolated Shrouded-Propeller Configuration for Angles of Attack From -10^o to 110^o," NASA TN D-995, Langley Research Center, Langley Field, Va., 1962.

[11] Yaggy, P.F., and Goodson, K.W., "Aerodynamics of a Tilting Ducted Fan Configuration," NASA TN D-785, Langley Research Center, Langley Field, Va., 1961.

[12] Yaggy, P.F., and Mort, W.M., "A Wind-Tunnel Investigation of a 4-Foot-Diameter Ducted Fan Mounted n the Tip of a Semispan Wing," NASA TN D-776, Ames Research Center, Moffett, Ca., 1961.

[13] Yaggy, P.F., and Mort, W.M., "Aerodynamics Characteristics of a 4-Foot-Diameter Ducted Fan Mounted on the Tip of a Semispan Wing," NASA TN D-1301, Ames Research Center, Moffett, Ca., 1962.

[14] Mort, W.M., "Performance Characteristics of a 4-Foot-Diameter Ducted Fan at Zero Angle of Attack for Several Fan Blade Angles," NASA TN D-3122, Ames Research Center, Moffett, Ca., 1965.

[15] Tapscott, R.J., and Kelley, H.L., "A Flight Study of the Conversion Maneuver of a Tilt-Duct VTOL Aircraft," NASA TN D-372, Langley Research Center, Langley Field, Va., 1960.

[16] Kelley, H.L., "Transition and Hovering Flight Characteristics of a Tilt-Duct VTOL Research Aircraft," NASA TN D-1491, Langley Research Center, Hampton, Va., 1962.

[17] Kelley, H.L., and Champine, R.A., "Flight Operating Problems and Aerodynamic and Performance Characteristics of a Fixed-Wing, Tilt-Duct, VTOL Research Aircraft," Langley Research Center, Langley Station, Hampton, Va., 1963.

[18] Stapleford, R.L., and Wolkovitch, J., and Magdaleno, R.E., and Shortwell, C.P., and Johnson, W.A., "An Analytical Study of V/STOL Handling Qualities in Hover and Transition," TR-140-1, Systems Technology, Inc., 1965.

[19] Ashkenas, I., and Graham, D., and McRuer, D. *Aircraft Dynamics and Automatic Control*, Princeton University Press, USA, 1973.

[20] Anderson, J.D., *Fundamentals of Aerodynamics*, Mc Graw-Hill, New York, NY, 2007.

[21] Barlow,J.B., and Rae,W.H., and Pope, A., *Low-Speed Wind Tunnel Testing*, Wiley-Interscience, New York, NY, 1999.

[22] Abbott, I.H., and Von Doenhoff,A.E., *Theory of Wing Sections*, Dover, New York, NY, 1959.

[23] Schmidt, L.C., et. al., *Product Engineering And Manufacturing*, College House Enterprises, LLC, Knoxville, TN, 2002.

[24] Raymer, D.P., *Aircraft Design: A Conceptual Approach*, AIAA, OH, 1999.

[25] Etkin, B., and Reid, L.D., *Dynamics of Flight: Stability and Control, 3rd ed.*, Wiley, Hoboken, NJ, 1996.

[26] Klein, V., and Morelli, E.A., *Aircraft System Identification: Theory and Practice*, AIAA, Reston, VA, 2006.

[27] Morelli, E.A., "Practical Aspects of the Equation-Error Method for Aircraft Parameter Estimation," AIAA Atmospheric Flight Mechanics Conference and Exhibit, Keystone, CO, Aug 21-24, 2006-6144.

[28] Nelson, R.C., *Flight Stability and Automatic Control*, Mc Graw-Hill, New York, NY, 1998.

[29] Willits, P., et. al. *Guided Flight Discovery: Private Pilot*, Jeppesen, Englewood, CO, 2007.

[30] Draper, H., and Smith, *Applied Regression Analysis*, Mc Graw-Hill, New York, NY, 1998.

[31] Iliff, K.W., and Maine, R.E., *Application of Parameter Estimation to Aircraft Stability and Control*, NASA Reference Publication 1168, 1986.

[32] Baruh, H., *Analytical Dynamics*, McGraw-Hill, Boston, Ma, 1999.